A VARIABLE SPACING DIFFRACTION GRATING CREATED WITH ELASTOMERIC SURFACE WAVES

by

ALISON JANE CLARK

B.Sc., The University of Waterloo, 1993

A THESIS SUBMITTED IN PARTIAL FULFILLMENT OF

THE REQUIREMENTS FOR THE DEGREE OF

MASTER OF SCIENCE

in

THE FACULTY OF GRADUATE STUDIES

(Department of Physics)

We accept this thesis as conforming
to the required standard

THE UNIVERSITY OF BRITISH COLUMBIA

June 1997

In presenting this thesis in partial fulfilment of the requirements for an advanced degree at the University of British Columbia, I agree that the Library shall make it freely available for reference and study. I further agree that permission for extensive copying of this thesis for scholarly purposes may be granted by the head of my department or by his or her representatives. It is understood that copying or publication of this thesis for financial gain shall not be allowed without my written permission.

Department of PHYSICS

The University of British Columbia
Vancouver, Canada

Date June 27/97

DE-6 (2/88)

ABSTRACT

This thesis concerns the first ever development of a variable spacing diffraction grating device created with the use of elastomeric surface waves. A variable spacing grating has the ability to deflect a laser beam to a continuous range of angles, thus allowing to steer the beam. This is achieved by diffracting an obliquely incident laser beam from a surface on which a mechanical wave is propagating.

Silicone rubber has an extremely low Young's modulus compared to non-elastomeric solids, and it can be easily cast. Using this material, surface waves can be created with low power, and such waves travel very slowly (~ 1 m/s) compared to conventional surface wave devices (~1000 m/s).

Four different types of elastomeric surface wave devices were constructed to examine their suitability as variable spacing diffraction gratings. Two of these produced surface waves that were suitable to diffract a laser beam.

The device which produced the biggest effect and most stable propagating surface wave a thin membrane of silicone rubber, supported on water. It is shown that the propagation speed of such waves is consistent with the White/Wenzel model, which predicts a dispersion relationship in terms of the membrane thickness, tension and modulus.

Overall, this structure appears to be promising for controlled diffraction, as well as other applications.

TABLE OF CONTENTS

LIST OF TABLES

LIST OF FIGURES

ACKNOWLEDGMENTS

I would like to thank everyone who has spent some time working in the Structure Surface Physics lab at UBC over the course of my M. Sc work. We have, I think, a unique environment, where, although everyone is working on distinct and different projects, there is continual enthusiasm, discussion and feedback.

This is an environment fostered successfully by our supervisor, Dr. Lorne Whitehead. His belief that the physics of new innovations is both fascinating and fun provides us with a driving force and a rewarding, challenging working environment. A special thanks goes to him for his support and insight throughout the project.

Specific thanks go to Peter Kan and Pinder Dosanjh for help with the lab equipment, Mike Montour for his help with the electronics for the piezo-electric stack, Stephane Jacob for his help with the image processing of the diffraction patterns and Michele Mossman for help with Labview and our useful discussions about the elusive properties of silicone rubber.

And of course, I owe everything to Kevin for not only his computer graphics wizardry in converting my ANSYS images into a format recognizable to Word, but also for his wonderful support in everything I do, (even during a triathlon!!!).

1. INTRODUCTION

A diffraction grating is a means of deflecting a laser beam to a well defined angle. However, conventional gratings have a fixed spacing and thus do not allow for the beam to be steered. It was our hypothesis that we could find a simple, low energy means of creating a variable spatial frequency diffraction grating that could be used to deflect a laser beam to a range of angles. Bulk acoustic waves in solid state crystal devices have been used with the disadvantage of operating at high frequency and high power in order to substantially deflect the laser beam. Silicone rubber is an elastomeric material that has a Young's modulus several orders of magnitude lower than the crystals used in conventional devices. This allows for a much lower wave speed and therefore, for a given wavelength, a much lower operation frequency. We postulated that the low frequency and modulus would allow the creation of low power traveling surface waves with sufficient amplitude to caused efficient diffraction. We investigated this possibility by launching a variety of surface wave modes into silicone rubber structures and examining the suitability of these devices as variable diffraction gratings.

1.1 Diffraction Gratings

The phenomenon of diffraction is based on the principle that light is in fact a wave. When a plane wave front encounters an aperture of similar dimensions to the wavelength of the wave, it will flare out in circular wave fronts originating from the aperture, as in Figure 1-1.

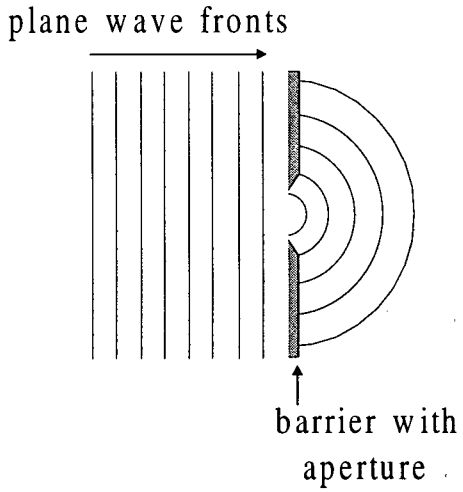

Figure 1-1: Diffraction of plane wave fronts from an aperture

When a series of apertures are placed at equal distances apart, a circular wave front originates from each of these apertures. Where two wave crests overlap, there is constructive interference. The combined action of the interference from each slit causes there to be constructive interference only in specific well defined angles. There are beams of light which are transmitted in angles different from the undeflected beam. These are called the orders of diffraction and they are number consecutively and symmetrically around the undeflected zero order beam. The apertures can be replaced with obstacles or scattering points, anything which affects the phase or the amplitude of an incident light beam. The important parameter is the spacing between the scattering centers, d. As shown in Figure 1-2, the smaller the spacing in the diffraction grating, the bigger the angular deflection, β, of the first order of diffraction.

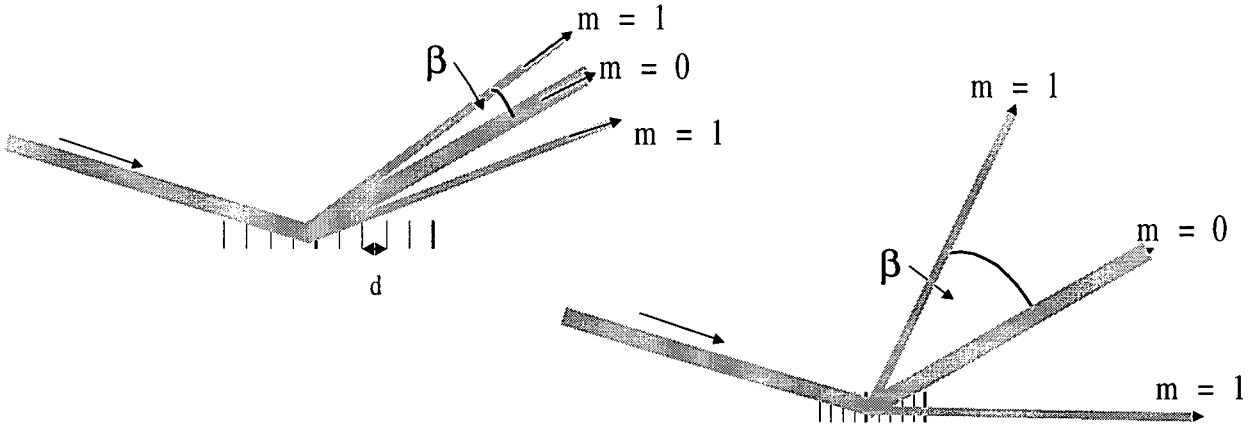

Figure 1-2: The dependence of the angular deflection of first order beam on the d-spacing

The array of repeated scattering elements which produce a diffraction grating can either be from the surface of a material or from the bulk properties of a material. For a surface grating, the incident light beam interacts with scattering elements which exist only the surface of the grating. Figure 1-3 shows a surface diffraction grating. It can either be a transmission or a reflection grating, depending on the transparency and/or the reflectivity of the material of the grating.

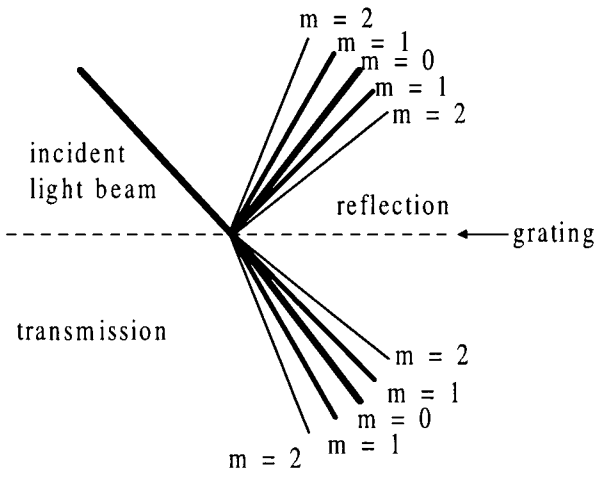

Figure 1-3: A surface diffraction grating can either be reflection or transmission

A diffraction grating that interacts with the bulk properties of a material must be able to transmit at least partially through the material. Figure 1-4 shows an example of a diffraction grating created from an array of scatter points that is uniform throughout the bulk of a material, such as a crystal lattice. Note that although, the diffracted beams are shown as originating from one scatter point in particular, the diffracted beams are as a result of constructive and destructive interference from the scattering from each point in the array.

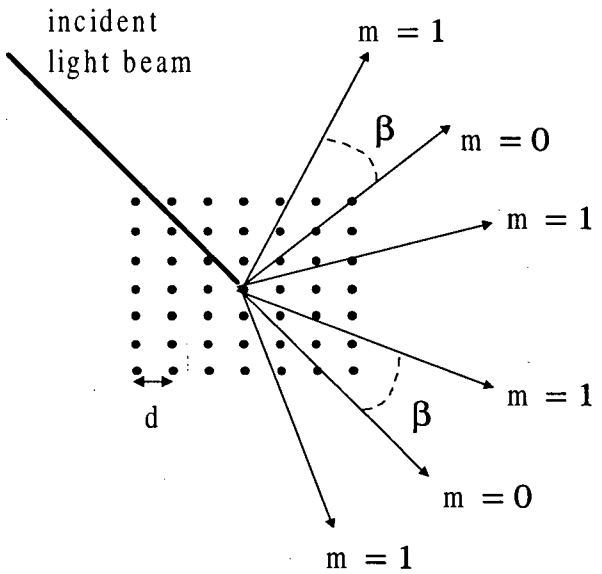

Figure 1-4: A bulk diffraction grating

We have seen how a diffraction grating can be produced from an array of fixed obstacles and/or apertures. It is also possible to create a diffraction grating from an acoustic wave which deforms the medium in which it is propagating. An acoustic wave is a mechanical wave, an example of which is the compressive wave commonly called sound. Figure 1-5 shows the five main types of

acoustic waves. There are two types of bulk waves, longitudinal and transverse. The third type, a Rayleigh wave, is a surface wave which the deformation of the material is restricted to a region near the surface. The last two, plate waves, are waves that travel in thin plates whose thickness is much smaller than the wavelength of the wave. As shown, there are two types: symmetric and asymmetric.

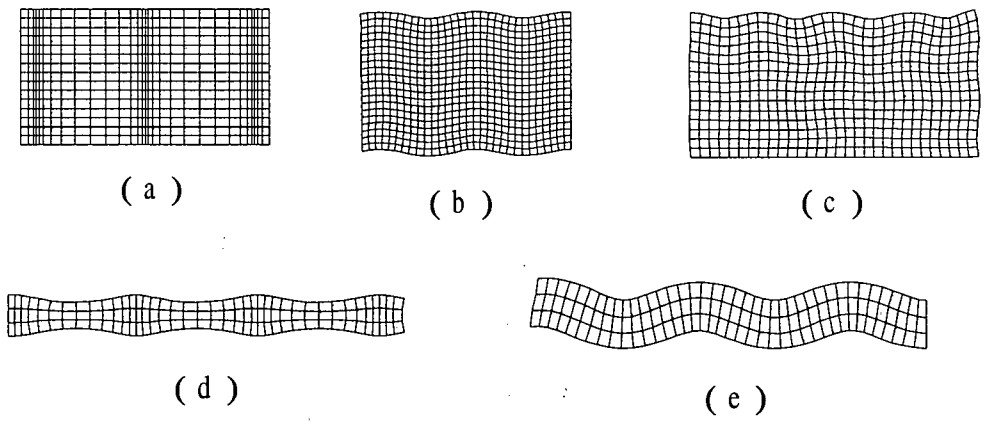

Figure 1-5: Acoustic waves: (a) longitudinal bulk wave, (b) transverse bulk wave, (c) Rayleigh surface wave, (d) symmetric plate wave, and (e) asymmetric plate wave

A surface reflection diffraction grating effect can be obtained from the sinusoidal deformation of a propagating surface acoustic wave. The acoustic wave has a constant wavelength which defines the characteristic d-spacing of the grating. The sinusoidal surface with crests and troughs acts as a series of lenses which scatter the incident radiation. Figure 1-6 shows this phenomenon.

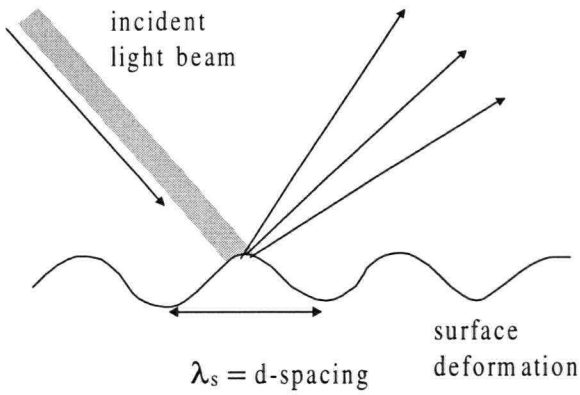

Figure 1-6: A surface acoustic wave acting as a diffraction grating

A bulk transmission grating can be made from a longitudinal bulk wave which affects the localized density and refractive index with a period of the wavelength of the wave. This periodic alteration of the refractive index is called the photoelastic effect and the interaction of incident radiation with this effect periodically alters the phase and acts a diffraction grating[1]. Figure 1-7 shows a bulk acoustic wave propagating with the change in grey-scale indicating a change in density of the bulk material.

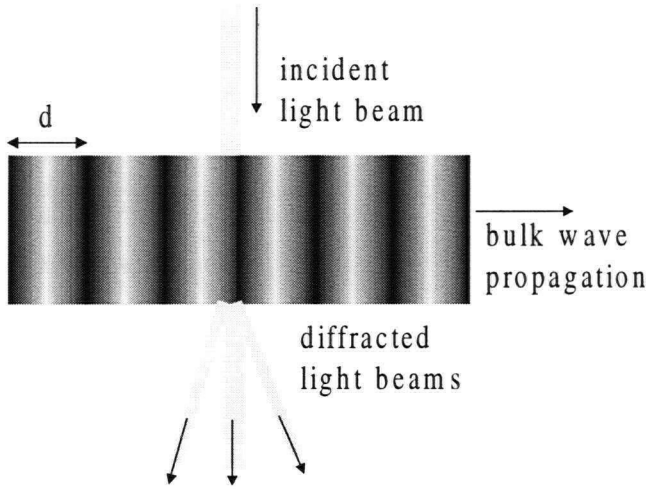

Figure 1-7: A bulk acoustic wave acting as a diffraction grating

The long term aim of this project was to produce gratings of variable d-spacing to control the angular deflection, β, of the first order diffraction beam. A major advantage of using an acoustic wave as a diffraction grating is the ability to change the wavelength of the wave and hence control β. For this purpose we studied various configurations in which different types of acoustic waves generated periodic structures. In order to better understand this work, it is helpful to review previous acoustic wave devices, namely the bulk acoustic wave device and the surface acoustic wave device.

1.2 Bulk Acoustic Wave Devices

Bulk acoustic wave devices are made from a longitudinal bulk wave traveling in a pure piezoelectric crystals. As discussed previously, the action of the photo-elastic effect creates a sinusoidally varying phase grating. These devices can therefore be used as diffraction gratings when a laser beam is directed through the transparent medium.

There are several disadvantages to using this method as a diffraction grating. Since the photo-elastic effect is weak, the incident beam has to interact with a significant portion of the bulk in order to have a reasonable fraction of the beam deflected. Also, the acoustic wave speed dictates that frequencies of order 100 MHz must be used in order reach a suitable wavelength. In short, this is an expensive technology as it necessitates the high power, high frequency actuation of a bulky piece of solid material.

1.3 Surface Acoustic Wave Devices

Surface acoustic wave devices employ a wave that travels in the vicinity of a free surface of a material. There are a variety of solid state surface wave devices which are used primarily for signal processing applications. Their main advantage is that the surface wave is mostly confined to within a wavelength's distance of the surface, making them easy to actuate, detect and interact with. Furthermore, the speed of surface waves tends to be slightly lower than the bulk wave speed, and the fact that the wave energy is confined make these lower power devices.

The energy density of surface acoustic waves (i.e. the energy of the wave per unit area of surface), $\mathcal{E}$, is calculated in Appendix A. It gives the relation given by Equation (1-1), which says that the energy density is proportional to the square of the amplitude, A, and the Young's modulus, E, but inversely proportional to the wavelength, λ_s, of the surface wave. This shows that for a given wavelength and amplitude, (i.e. those that would be necessary for diffraction) the energy density is proportional to the Young's modulus.

$$\mathcal{E} \propto \frac{A^2 E}{\lambda_s} \qquad (1\text{-}1)$$

As is discussed in section 2.2, silicone rubber is a material that has a substantially lower Young's modulus than the solid state crystals used in conventional acoustic wave devices (10^6 versus 10^9 N/m^2). Therefore, surface acoustic waves generated in silicone rubber will automatically have a much lower power load. In addition, the higher flexibility of the material means that wave

amplitudes (~ ½ λ_{light}) necessary to produce substantial diffraction effects are easier to achieve. Also, since wave speed is proportional to modulus, the frequency needed to generate a given wavelength will be lower. For these reasons we speculated that silicone rubber would make a good candidate for the medium in which to propagate acoustic surface waves.

1.4 Scope of this Study

This thesis investigates the possibility of using a surface wave in silicone elastomer to produce a variable spacing surface diffraction grating. Various types of surface waves in silicone structures were characterized, namely Rayleigh, and plate waves. From this work it was possible to determine the suitability of these waves to the application of diffraction gratings. The important parameters of interest were the wave amplitude, the wavelength and wave speed of the waves. Obviously, there must be a certain minimum wave amplitude necessary before a diffraction effect is observed, and we tested our waves to see if this threshold had been reached. Since the wavelength is analogous to the d-spacing of the resultant grating we attempted to minimize the surface wavelengths of the devices. This would maximize the amount of angular deflection, β, that could be achieved. The final design consisted of a plate wave in an elastomer membrane supported by water, a design chosen because it exhibited the most promising characteristics for a practical device.

Chapter 2 outlines the background of the various subject areas included in this study. Firstly, the basic theory of diffraction gratings is discussed with reference to conventional fixed spacing

gratings. Secondly, the mechanical and dynamic properties of silicone rubber are described. Finally, various relevant types of traveling waves are given with the mathematical formulae to describe them.

Chapter 3 discusses the design consideration issues relevant to using elastomeric surfaces waves as a variable spacing diffraction grating. Since we will be making a reflection surface grating, it is important that the surfaces in which the wave is propagating is optically flat. This will ensure that there is a good zero-order spot, and that the waves can propagate unhindered. We will discuss the fact that using a obliquely incident light beam will increase the angular deflection, β, and boost the deflecting power of the device. Four different methods were used to create elastomeric surface waves and they are described in detail. Finally, the advantages of the final design are outlined.

Chapter 4 describes the various methods which were used to model the device. Firstly, a scalar diffraction model is described. This model was used to predict the expected diffraction pattern for reflection from a given surface deformation, at a specified angle of incidence and wavelength of laser light. This allows for a comparison with experimentally measured diffraction patterns, and for the investigation of the various factors which affect the resolution of the diffraction pattern. These factors are wave amplitude, wavelength, and wave attenuation. Secondly, the description of a finite element analysis for the various employed waves in silicone rubber structures is presented. Finite element analysis was used to determine the expected properties of the traveling waves. Finally, an analytical model is given which allows for the complete description of the

water supported plate waves with the following input parameters: rubber modulus, rubber density, membrane thickness and membrane tension.

Chapter 5 explains the results of the models described above along with comparisons to all experimental findings. It is shown that we have a complete understanding of the mechanical phenomena of the surface waves. Furthermore, we demonstrate that it is possible to use these surface waves as variable spacing diffraction gratings

The effectiveness of this device as means of steering a laser beam is limited by the minimum surface wavelength can be achieved. Our main intent in undertaking this project was to prove the concept that an elastomeric surface wave could be used as a variable spacing diffraction grating. Based on these results, future work may concern finding designs which are commercially viable, yield a higher deflection , have high efficiency, in terms of both power and light, and show a fast response time.

2. BACKGROUND

This thesis describes the development of a variable spacing diffraction grating created with the use of surface waves traveling in silicone rubber. As such, the background of several diverse fields in physics and engineering must be covered to fully understand how the concept works and why it is unique. Firstly, the theory of fixed spacing diffraction gratings is discussed. Then the mechanical and dynamical properties of silicone rubber are described, as they are important to the way in which waves will propagate in this medium. Finally, we discuss the propagation of traveling waves in elastic media and show that the use of silicone rubber as a medium can produce waves with exceptionally low wave speeds compared to non-elastomeric solid materials.

2.1 Diffraction Gratings

In order to design a variable spacing diffraction grating, we must first understand the physics and parameters for regular fixed spacing gratings. A conventional diffraction grating is a regularly spaced array of apertures or obstacles which modulates the phase and/or amplitude of incident light beams. This causes interference in the transmitted or reflected light beams which has the effect of emission of light in distinct directions. The spacing of the obstacles, d, controls the angular deflection of each of the diffracted beams, called the orders of diffraction. The pattern that these beams make when they are projected onto a surface is called the diffraction pattern. It is symmetric around the bright spot, or fringe corresponding to the undeflected beam, called the

m=0 order. The higher orders are numbered consecutively and symmetrically around the m=0 order.

A transmission diffraction grating is shown in Figure 2-1, it usually consists of a glass plate scribed with regularly spaced grooves that modulates the phase of the incoming beam. For normal incidence light of wavelength λ_l, a bright fringe of light occurs when the conditions of constructive interference are met according to the grating equation, Equation (2-1), where m denotes the order of the fringe, at angle θ_m to the normal. Since this effect is wavelength dependent, a diffraction grating is used in spectroscopy to view the spectrum of a radiation source. For example, a grating with a 'd-spacing' of 2000 nm spreads the first order visible spectrum over an angle of about 10 °.

$$d\sin(\theta_m) = m\lambda_l \qquad m = 0,1,2,\ldots \qquad (2\text{-}1)$$

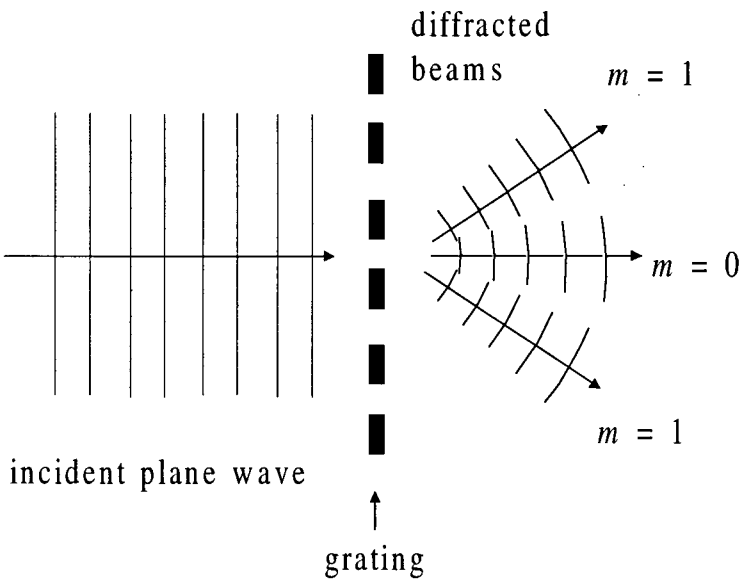

Figure 2-1: Transmission diffraction grating

The incident beam can also come at an oblique angle, either for a transmission grating or a reflection grating. Figure 2-2 shows the configuration for an obliquely incident beam reflecting from a diffraction grating. Equation(2-2) gives the equation for transmission and reflection for obliquely incident light.[2] Figure 2-3 shows how, d, θ_m, and θ_i are defined relative to the diffraction grating. It can be shown from Equation (2-2), that as the angle of incidence approaches 90°, the angular separation between the orders of diffraction increase substantially, therefore, for our application a boost in performance can be achieved easily by using a glancing angle configuration.

$$d\left(\sin\theta_m - \sin\theta_i\right) = m\lambda_l \qquad m = 0,1,2,\ldots \qquad (2\text{-}2)$$

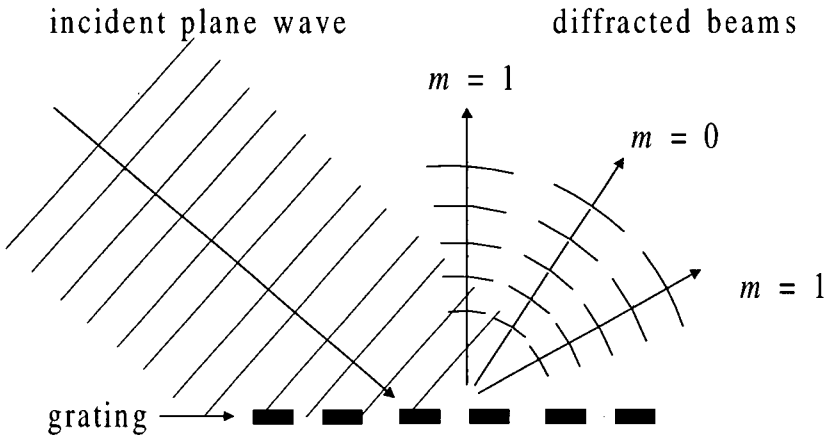

Figure 2-2: Reflection diffraction grating

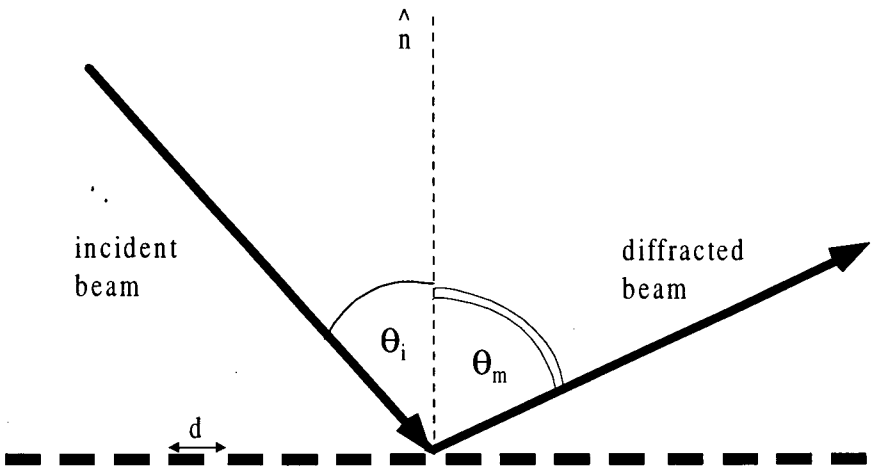

Figure 2-3: Geometry of oblique incidence diffraction

In a regular diffraction grating, a large portion of the incident light energy remains in the undeflected 0^{th} order. For the purposes of beam switching, it is desirable to shift this energy into one of the higher orders, since the $m = 0$ order does not move. This can be done with the use of a blazed grating as shown in Figure 2-4. The orientation of the groove surfaces provides a preferential direction for light to be diffracted corresponding to specular reflection off these blazed surfaces. This depends on γ, the blaze angle which defines the angle between the blazed surface and the plane of the diffraction grating, and θ_i, the angle of incidence. For example, Figure 2-4 shows that normally incident light has a specular reflection at an angle of 2γ from the normal to the plane of the grating. For particular values of θ_i, the diffraction pattern, instead of being symmetric around the 0^{th} order, will have all the light power concentrated into one

particular order. If we could produce a convolution of surface waves that has a profile similar to the blazed grating shown below, the variable spacing grating would be more suitable for the purposed of beam switching.

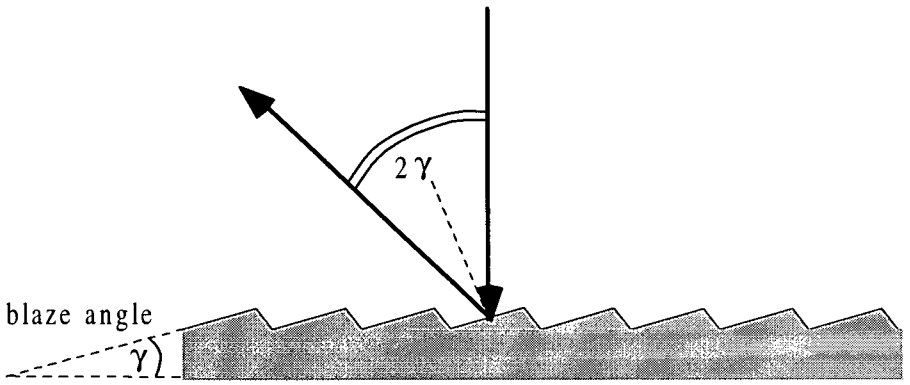

Figure 2-4: Blazed reflection phase grating

A word must be said here about the fact that we intend to use a propagating surface wave as a diffraction grating. The traveling surface wave will have the effect of giving Doppler frequency shifts to the diffracted orders as indicated in Figure 2-5.[3] The frequency of the incident radiation, $\omega_o = 2.98 \times 10^{12}$ kHz, is many orders of magnitude higher than the frequencies of operation we intend to use, ω_a = 1 kHz - 20 kHz. Therefore, this will produce a negligible frequency shift, and the surface waves will appear to be stationary relative to the incident light radiation.

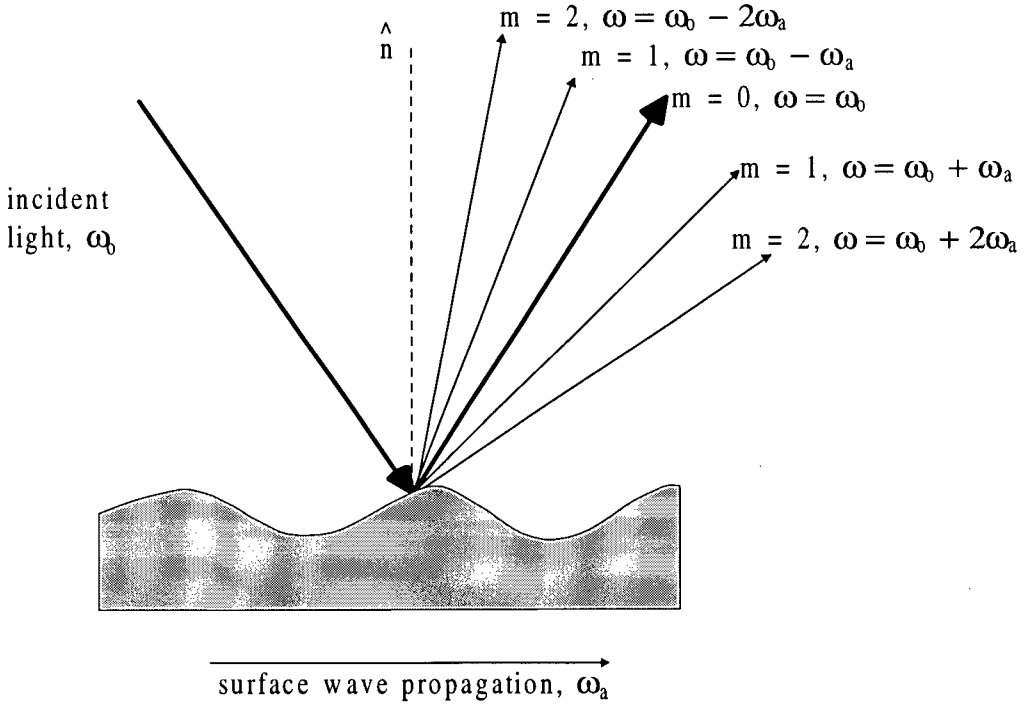

Figure 2-5: Optical interaction with propagating surface waves

Now we have considered the theory of diffraction gratings, we turn our attention to the theory of the silicone rubber, the medium in which we will produce these diffraction gratings. It is important to emphasize again that we wish to produce surface waves with as small a wavelength as possible to maximize the deflecting power of the resultant diffraction grating.

2.2 Silicone Rubber

The reason that silicone rubber was used as the medium for the surface waves in this project was the ability to propagate extremely low wave speeds. This means that we can achieve small surface wavelengths at comparatively low driving frequencies. Silicone rubber is an elastomeric member

of the synthetic polymer family based on a polymer backbone of silicon and oxygen. It has good chemical and physical stability over a wide range of temperatures, which as will be shown, means that it retains its rubbery behaviour up to a high frequency of deformation, a property necessary to achieve small surface wavelengths.

2.2.1 Physical properties

Rubber, or elastomer, is defined as a 'macromolecular material that returns rapidly to approximately the initial dimensions and shape after substantial deformation by weak stress and release of the stress'.[4] It is highly deformable compared to non-elastomeric materials, but has similar compressive stiffness. In other words, it is much easier to stretch that it is to compress.

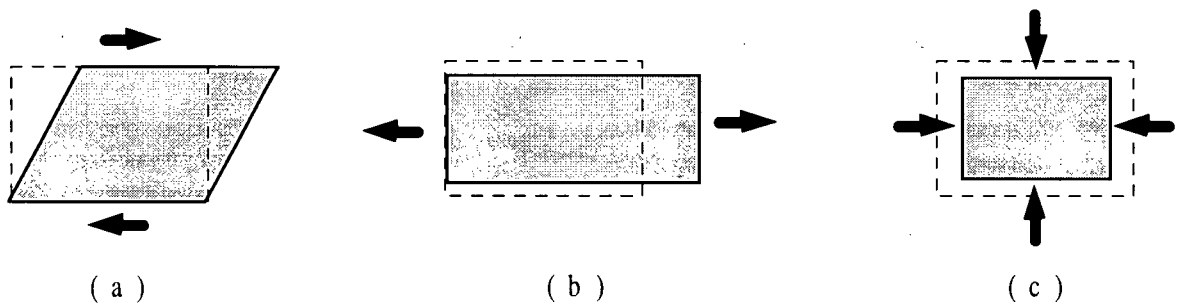

Figure 2-6: A body under: (a) shear stress, (b) tensile stress and (c) bulk compression

At low strains, the classical theory of elasticity can be used to describe the mechanical properties of rubber. Three kinds of elastic modulii are used which describe resistance to shear, tension and bulk compression, each of which is depicted in Figure 2-6. These are, respectively, shear modulus, Y, Young's modulus, E, and bulk modulus, K. Equations (2-3) and (2-4) show how these modulii are related through the Poisson's ratio, ν. These relations are valid for conventional elastic materials, and assume that the physical mechanisms responsible for the different modulii are inter-atomic forces. However, it has been shown that the extremely low shear and Young's modulii for elastomeric materials are in fact due to van der Waals forces, a completely different mechanism.[5] As such, the definition of a Poisson's ratio which relates the different modulii is meaningless for rubber. By measuring both the bulk and shear modulii, values of ν_{rubber} of 0.4997 [6] and 0.499992 [7] have been reported. A Poisson's ration of $\nu_{rubber} = 0.5$ defines an incompressible material and is generally a good approximation for rubber.

$$E = 2Y(1+\nu) \qquad (2\text{-}3)$$

$$E = 3K(1-2\nu) \qquad (2\text{-}4)$$

The Young's modulus is the ratio of the stress versus strain for a material undergoing tension. It is important to this work because, as will be discussed later, wave speed is proportional to the Young's modulus. For most solid materials the Young's modulus, E, is of the order of 10^9 N/m^2. For rubber it is typically measured as the force per unit of original cross-section for an elongation of (usually) 300 percent.[8] Due to the high extensivity of rubber, the Young's modulus is consequently much lower ~ 10^6 N/m^2. Rubber is a non-linear material, meaning that the stress

versus strain curve is not a straight line. Figure 2-7 gives an example of a stress-strain curve for rubber. Over a small range of elongation, such as waves with amplitudes small compared to their wavelength, rubber can be considered linear in behaviour and the classical theories and modulii of elasticity can be applied.

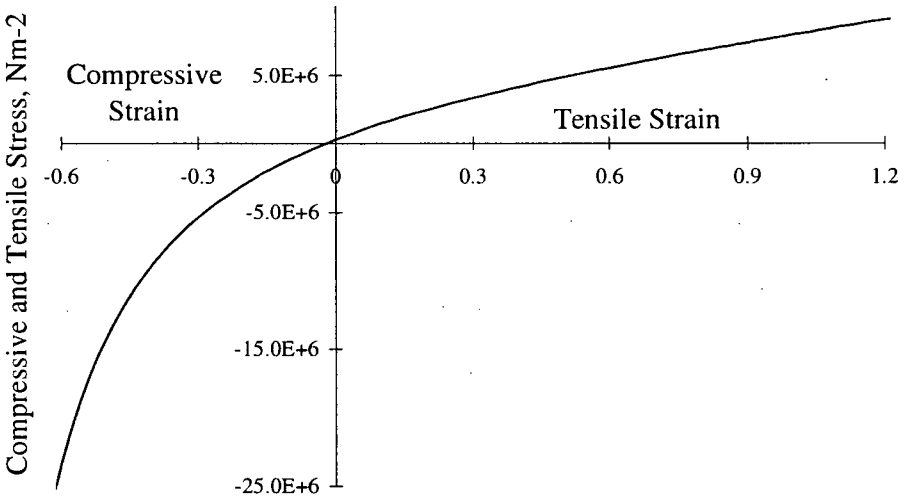

Figure 2-7: Typical stress-strain curve for rubber

The problem arises in choosing a value of modulus to substitute into the wave speed equations to model the surface wave. From a practical point of view, the material data sheets on commercially available silicone rubbers do not state the Young's modulus. The most common value given is the Shore A hardness. This is determined with a machine called a Durometer made by the Shore Instrument Company, which measures the resistance of the rubber to deformation by a ball pressed into the surface. Typical Shore A hardness values range from 15 for a soft silicone, to 80

for a relatively hard one. The value for hardness correlates loosely to the modulus, i.e. a low hardness rubber will have a low modulus. Table 2-1 shows the correlation between the Shore A Hardness value given by the manufacturer and the modulii based on experiments on natural rubber.[9]

Table 2-1: Relationship between hardness and modulus for natural rubber

Shore A Hardness	E 10^6 Nm^{-2}	Y 10^6 Nm^{-2}	K 10^6 Nm^{-2}
28	0.92	0.30	1000
33	1.18	0.37	1000
39	1.50	0.45	1000
44	1.80	0.54	1000
49	2.20	0.64	1030
54	3.25	0.81	1090
59	4.45	1.06	1150
64	5.85	1.37	1210
70	7.35	1.73	1270
75	9.40	2.22	1330

The molecular structure of silicone rubber imparts some unique surface energy properties to the bulk of the material that we found may have affected some of our results. The surface tension or the surface free energy per unit area of the silicone elastomer is known to be low (~0.020 N/m) but also to be dependent on the environment at the interface.[10,11] The silicone is made up of a long flexible siloxane chain with pendant methyl groups, as shown in Figure 2-8. These methyl groups are able to reorient themselves to adopt low energy configurations. In a polar aqueous

environment, the methyl groups, are hydrophobic and orient themselves toward the bulk of the silicone which gives a relatively low interfacial tension with water.

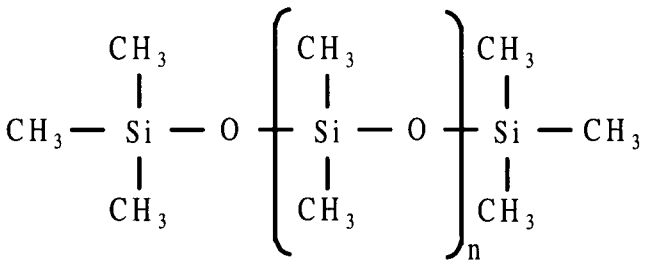

Figure 2-8: Polydimethylsiloxane molecule

2.2.2 Dynamic properties

The behaviour of the silicone rubber depends on the frequency of deformation due to the relaxation time of the long polymer networks in the rubber. Figure 2-9 shows the general behaviour of the Young's modulus as a function of both temperature and frequency. At low frequencies, the solid is in a 'rubbery' state. As the frequency of deformation is increased, the modulus and damping start to sharply rise. Finally, at high frequencies, the modulus levels off to a value comparable to solid amorphous materials and the rubber is said to be in a 'glassy' regime. The frequency at which this transition occurs is called the glass-transition frequency. Since, this behaviour is due to the thermodynamic properties of the macro-molecular chains in the polymer, the effect of raising the temperature counteracts the effect of raising the frequency. This behaviour is described by the frequency-temperature supposition principle. This dictates that at low temperatures and high frequencies the rubber behaves like a conventional solid with a high

Young's modulus. For example, in the figure below, the rubber has a glass transition at -120°C. Alternatively, if it is kept at a constant room temperature and the frequency of deformation is increased, it will have a glass transition around 4 x 10^{11} Hz.

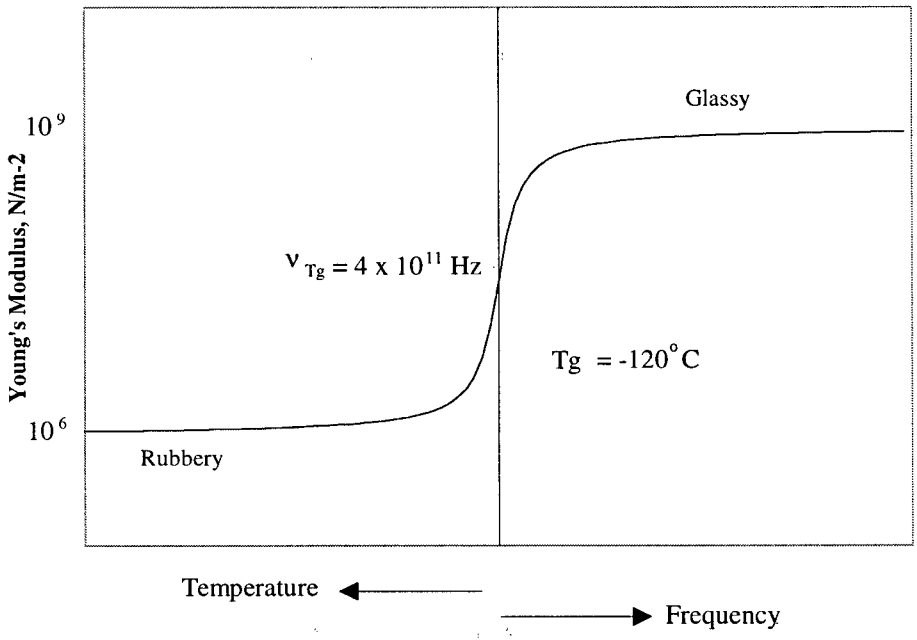

Figure 2-9: Young's modulus of rubber as a function of frequency and temperature

The temperature at which the transition occurs is called the glass transition temperature. The Williams, Landel and Ferry (WLF) equation, Equation (2-5), relates the glass transition temperature, T_g, measured at a frequency, υ_{Tg}, (usually very low) to the corresponding glass transition frequency, υ_T, at a given temperature, T.[12] This equation was developed with the use of the method of reduced variables due to Ferry and Fitzgerald.[13] It takes dynamic property data

measured at a variety of temperatures and reduces it to a master curve for a single reference temperature.

$$\log\left(\frac{\upsilon_{T_g}}{\upsilon_T}\right) = \frac{-16.2\left(T - T_g\right)}{55.6 + T - T_g} \qquad (2\text{-}5)$$

Generally, measurements of the physical properties of rubbers are performed by changing the temperature, rather than the frequency, since it is difficult to change the frequency of operation over many decades, but comparatively simple to change temperature over the corresponding several hundreds of degrees of temperature implied by Equation (2-5). The results are then translated into their frequency dependent values using the WLF equation. Figure 2-10 shows the Young's modulus, *E*, of RTV31 at a reference temperature of 10°C over many decades of frequency.[14] It can be seen that it appears to behave in a rubbery manner up to a high frequency.

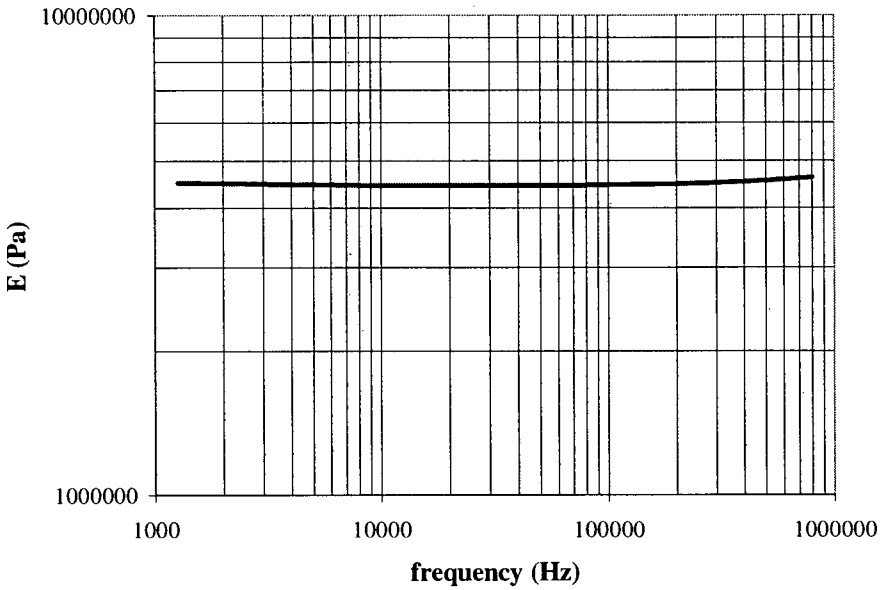

Figure 2-10: Young's modulus of RTV31 as a function of temperature at a temperature of 10°C

However, despite the fact that the silicone rubbers have the lowest glass transition temperature of about -100 °C , experimental findings suggest that this does not necessarily correlate to a high glass transition frequency. Bosc. et al. found a discrepancy between the behaviour predicted by the WLF equation and their experimental values.[15] The theory predicted that at 10 MHz the silicone should still be in the rubbery regime. However, at this frequency, the speed of sound in the rubber was ~1000 m/s indicating that it was in the 'glassy' regime. Their conclusion was that for silicone elastomers at high frequencies the glass transition temperature is above room temperature, in disagreement with the WLF equation. Therefore, it is difficult to trust the given values for the Young's modulus for silicone rubber, since it is unknown how it was measured.

Table 2-2 shows the physical properties as given by the manufacturer of various silicone rubbers used in this experiment. In the next section on traveling waves we will learn how the wave speed of the different wave types depends on the properties of the silicone rubber medium. Using these values we can predict what wave speed we would expect from using each different kind of rubber.

Table 2-2: Physical properties of silicone rubbers used in this study

Silicone Rubber	Density, ρ (kg/m^3)	Shore A Hardness	Glass Transition Temperature T_g (°C)	Coefficient of Thermal Expansion α, (cm/cm/°C)
HSII	1210	16	-	-
Silastic T	1130	38	-	-
RTV31	1420	54	-54	20×10^{-5}
RTV615	1020	44	-60	27×10^{-5}
RTV655	1040	45	-115	33×10^{-5}

2.3 Traveling Waves

A mechanical wave consists of a mechanical disturbance which propagates in a medium, and the research reported here specifically concerns such waves traveling in silicone rubber. A wave can be described by its type and its mode. The wave type describes the way in which the medium is moving as the wave propagates, in particular the relative positions of the wave vector, $\underline{\boldsymbol{k}}$, and the polarization vector, ξ. The wave vector indicates the direction of propagation of the wave and the polarization vector indicates the direction of movement of the particles in the medium. The

wave mode indicates either in which direction the wave is propagating, or it indicates the order of the wave. The wave speed depends upon the type of wave, the medium properties and, in the case of waves being confined to physical structures, which of the wave modes are being propagated.

There are three general wave types to be considered- bulk, surface, and plate waves. A bulk wave consists of either a longitudinal pressure wave or a transverse shear wave. In an elastomer, bulk waves travel at a speed similar to that of sound waves in fluids, while transverse shear waves travel at a substantially lower speed, because of the low Young's modulus of such materials. Surface waves propagate with virtually all of the wave energy confined to within a few wavelengths distance of the top surface. Finally, plate waves travel in thin plates whose thickness is significantly smaller than the wavelength.

2.3.1 Traveling Wave Types

The bulk wave velocity depends only on the modulii of elasticity and the density of the medium. Both longitudinal waves and transverse waves are possible. Figure 2-11 shows how these waves travel through the bulk of the material, given that in the undisturbed state, the material would be represented by a uniform grid. Equation (2-6) gives the bulk longitudinal wave speed and Equation (2-8) gives the bulk transverse wave speed for an elastic material.[16] In the case of rubber, Equation (2-6), which contains the Poisson's ratio, can be simplified to Equation (2-7) using $\nu = 0.5$. For example for RTV31 with $\rho = 1420$ kg/m^3 and $E = 4.5 \times 10^6$ N/m^2, the speed of the bulk longitudinal wave would be 1327 m/s, while that of the shear wave would be 97 m/s.

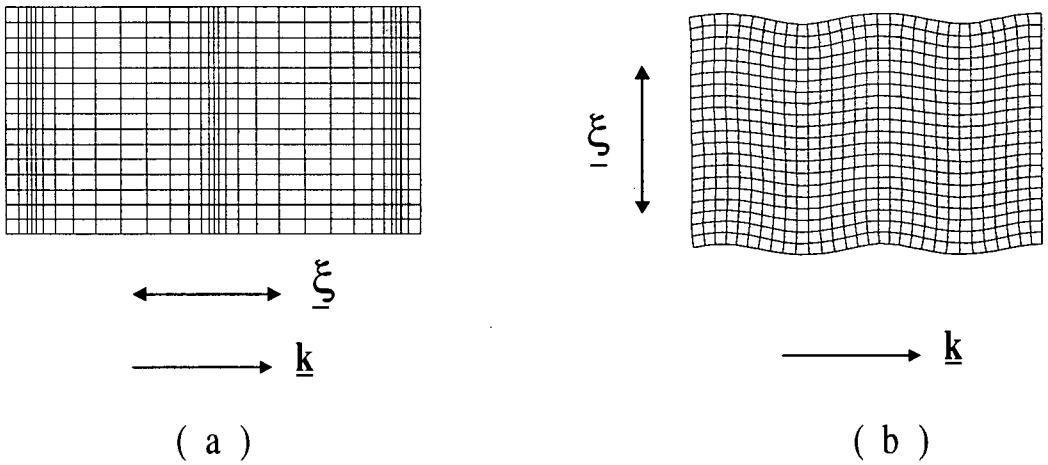

Figure 2-11: (a) Longitudinal and (b) transverse bulk wave modes

Bulk Longitudinal Wave Speed

$$c = \sqrt{\frac{E}{\rho}\frac{1-\nu}{(1+\nu)(1-2\nu)}} \qquad (2\text{-}6)$$

$$c_{rubber} = \sqrt{\frac{K}{\rho}} \qquad (2\text{-}7)$$

Bulk Transverse Wave Speed

$$c = \sqrt{\frac{Y}{\rho}} \qquad (2\text{-}8)$$

A Rayleigh wave is a type of surface wave that travels only along the free surface of an elastic material. It consists of both a longitudinal wave and a shear wave with a relative phase shift of

$\pi/2$. Figure 2-12 depicts a Rayleigh wave propagating along the top surface of the bulk material. The particles at the surface move in elliptical orbits as the Rayleigh wave passes by, as indicated by the precession of the polarization vector, $\underline{\xi}$. The magnitude of this polarization vector dies out exponentially with distance into the bulk of the material

Equation (2-9) gives the approximate wave speed for the Rayleigh mode. The coefficients in the expression are due to an approximation of the solution of an exact equation which has 6 roots. There is only one root which is between 0 and 1 and pertains to a real medium with $0<\nu<0.5$, this corresponds to the Rayleigh mode and gives us the expression in Equation (2-9).[17] For RTV31 the c_R is 31 m/s. This Rayleigh mode is useful because of its comparatively low wave speed and the fact that substantially all the energy is confined to the surface region that is doing the optical work.

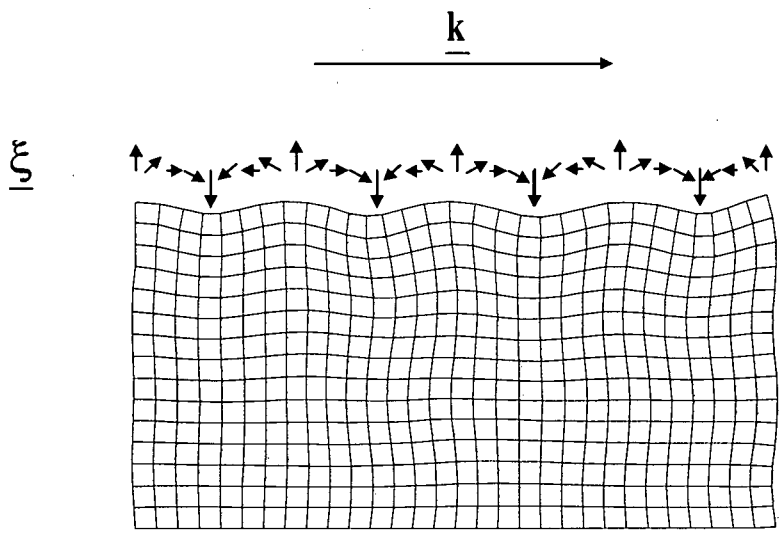

Figure 2-12: Rayleigh wave mode

Rayleigh Wave Speed

$$c_R = \left(\frac{0.87 + 1.12\nu}{1+\nu}\right)\sqrt{\frac{Y}{\rho}} \qquad (2\text{-}9)$$

The last type of wave considered here is known as a plate, or Lamb wave. Such a wave propagates in thin plates or membranes whose thickness is smaller than the wavelength of the wave. The wave is actually a combination of two Rayleigh waves propagating along the top and bottom surfaces. As the relative size of the thickness and the wavelength changes, the speed of propagation is affected. Hence, these waves are highly dispersive, which in some circumstances may be undesirable. On the other hand, it may be advantageous that it is possible to select the wave speed by changing the thickness of the plate, t. Figure 2-13 and Figure 2-14 show two possible plate wave types. Equation (2-10) gives the speed for the symmetric plate mode and Equation (2-11) gives the speed for the lowest order asymmetric plate mode. Since, the asymmetric wave has the lowest wave speed, it is the most useful in terms of generating small wavelengths at low frequencies. For example, with t = 25μm, λ_s = 0.001 m, a typical elastomer has a wave speed of 3 m/s, substantially lower than all other wave types.

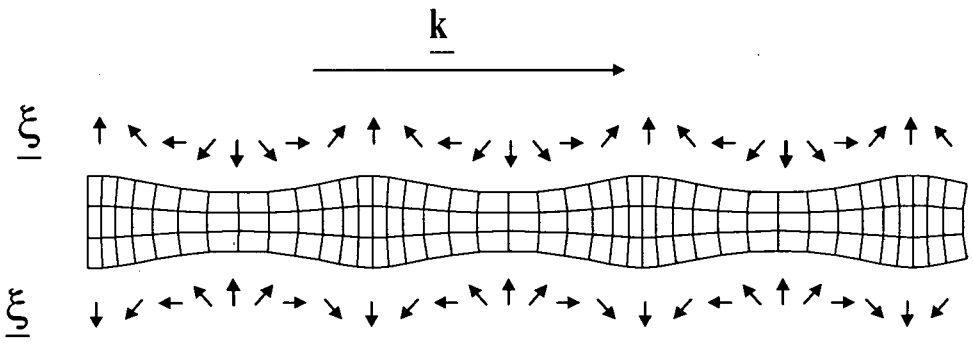

Figure 2-13: Symmetric plate wave

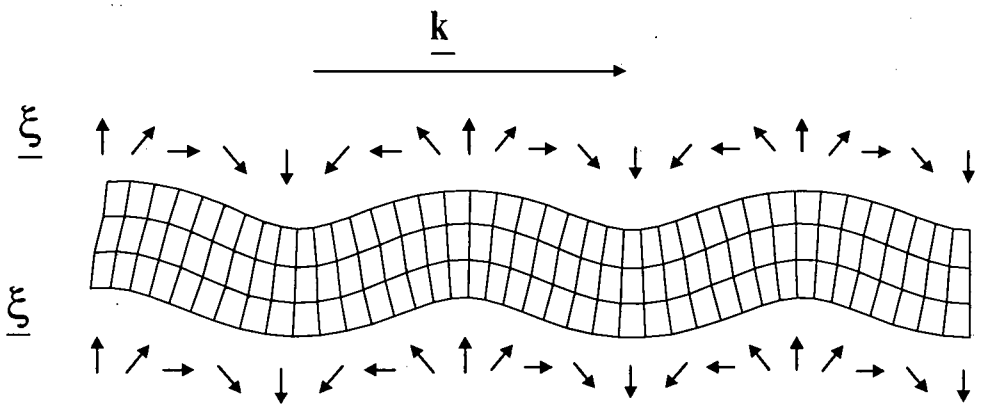

Figure 2-14: Asymmetric plate wave

Symmetric Plate Wave Speed $$c_s = \sqrt{\frac{E}{\rho(1-\upsilon^2)}} \qquad (2\text{-}10)$$

Asymmetric Plate Wave Speed

$$c_a = \left[\left(\frac{2\pi}{\lambda_s} \right)^2 \frac{1}{\rho} \frac{Et^2}{12(1-\upsilon^2)} \right]^{1/2} \quad (2\text{-}11)$$

2.3.2 Characterization of Traveling Waves

In general, a traveling wave has amplitude, A, wavelength, λ, and wave speed, c. The frequency, f, corresponds to the driving frequency of the source creating the wave. Since there are losses in the rubber, the traveling wave attenuates with a damping factor, often referred to as a loss tangent, $tan\delta$. These values are defined and related using the following equations.

Wave Equation

$$c = \lambda f \quad (2\text{-}12)$$

Natural Wave Number

$$\kappa_o = \frac{2\pi}{\lambda} \quad (2\text{-}13)$$

Loss Wave Number

$$\kappa_l = \frac{-\Delta ln(A/A_o)}{\Delta x} \quad (2\text{-}14)$$

Loss Tangent

$$tan(\delta) = \frac{\kappa_l}{\kappa_o} \quad (2\text{-}15)$$

Figure 2-15 depicts these parameters for a typical graph of displacement versus distance for a traveling wave at a particular moment in time.

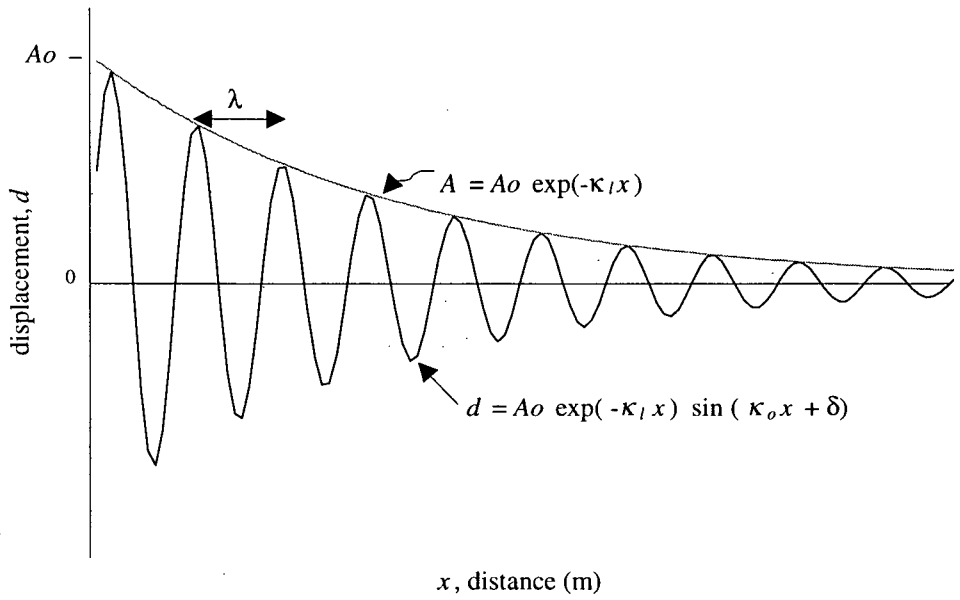

Figure 2-15: Traveling wave parameters

2.3.3 Wave attenuation

The attenuation of the wave amplitude as a function of distance, x, is given by Equation (2-16). The loss number, κ_l, can also be interpreted as an attenuation coefficient, α. The physical cause

of this attenuation is due to the properties of the medium in which the wave is propagating. In fact, attenuation coefficient has contributions from two different mechanisms, absorption and scattering, as given by Equation (2-17) where α_a is the absorption coefficient and α_s is the scattering coefficient.[18]

$$A = A_o \exp(-\kappa_l x) \qquad (2\text{-}16)$$

$$\alpha = \alpha_a + \alpha_s \qquad (2\text{-}17)$$

The absorption coefficient includes energy losses from the rubber itself. This is caused by a heat loss associated with friction from the action of the long polymer molecules as they move past each other in response to an applied stress.

The attenuation of the wave due to scattering is caused by irregularities in the medium in which the wave is propagating. In the case of surface waves in silicone rubber, it will depend on how flat or smooth the surface is. A criteria for efficient diffraction from these surfaces is that they are at least optically flat. This ensures that there is a good zero-order reflection from the surface. Optically flat generally means that the surface is smooth to within a quarter of a wavelength of the incident light radiation. For the case of a HeNe laser this value is $\lambda_l/4 \cong 200$ nm and we can estimate for the purpose of this calculation that D, the characteristic diameter of any surface irregularities or scattering centers, is this value. The surface wavelength of the waves achieved by this device, λ_s, are of order of 10000 nm, therefore, $\lambda_s >> D$. For this case the scattering

coefficient follows the trend given by Equation (2-18). This curve is plotted in Figure 2-16 where D was taken to be 200 nm. It can be seen that up to the driving frequencies being used in this experiment, there will be a negligible contribution from scattering loss, as the surface wavelength is so much bigger than any irregularity on the silicone rubber.

$$\alpha_s \propto D^3 f^4 \qquad (2\text{-}18)$$

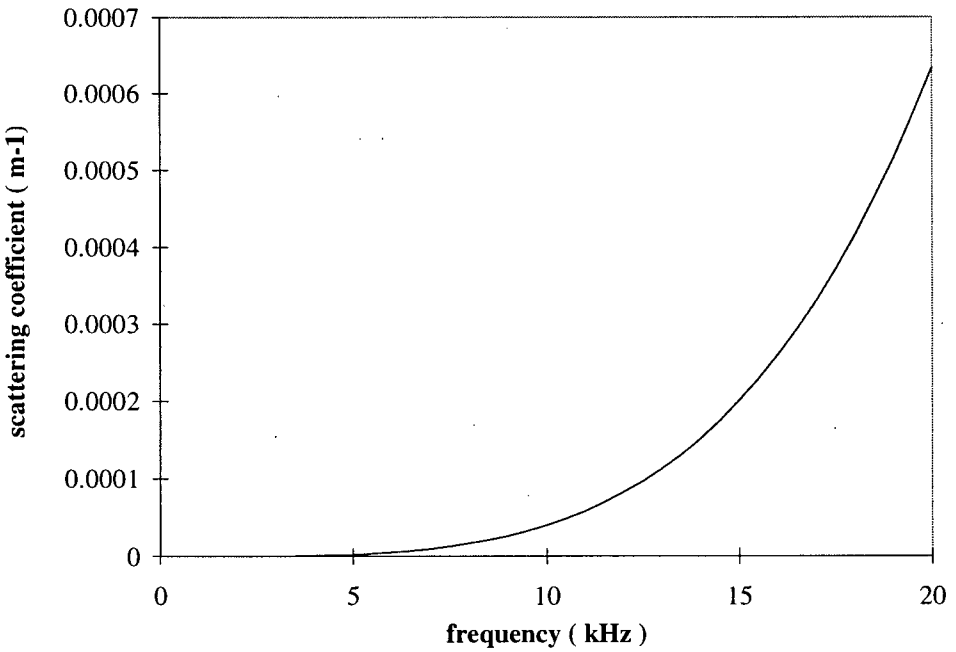

Figure 2-16: Dependence of scattering coefficient on driving frequency

2.4 Impedance Considerations

Impedance considerations are often helpful when understanding the efficiency of power transfer. Generally, impedance is the ratio of the restoring force associated with a traveling disturbance to the rate of change of the associated displacement. For sound this in units of force/velocity, and one normally speaks of this impedance per unit area. For electrical transmission lines, this is voltage/current. This a useful concept because when transferring power from one medium to another, if there is an impedance match between the mediums then there is a maximum power transfer.

A closely related concept is that of matching the internal impedance of a power source to that of its load. It is tricky to do this when dimensions don't match, as in our case, but some general statements can be made. We used two methods of launching surface waves into silicone rubber - a current carrying wire vibrating in the field of a strong magnet and a piezoelectric stack which changed its length in response to an alternating current. In the case of the magnetic drive, the wire attached to the rubber had low impedance relative to the resistance of the rubber to deformation. That is, the rubber represented the main restriction to the range of movement of the wire. In the second case of the piezoelectric stack, it had high impedance relative to the rubber, as its displacement was not limited by the resistance of the rubber, but rather by the stiffness of the crystal. Thus, the power transfer in both cases was not efficient, but this is not an issue since we were still able launch measurable surface waves suitable for the purposes of this study. If this

idea was ever made into a commercial device, there would have to be considerable effort to match the impedance of the actuator and the silicone rubber.

3. EXPERIMENTAL DESIGN CONSIDERATIONS

As mentioned in the introduction, one of the goals of this research was to create a variable spatial frequency diffraction grating through the interaction of an obliquely incident light beam with a surface wave in silicone rubber. This chapter concerns the creation of surface waves with a line driver operating at a variable frequency. The driver produces plane wave fronts in the surface of the rubber. The propagation direction of the surface waves is in the same direction as the plane of the incident and reflected light beams. Figure 3-1 shows the geometry of this design.

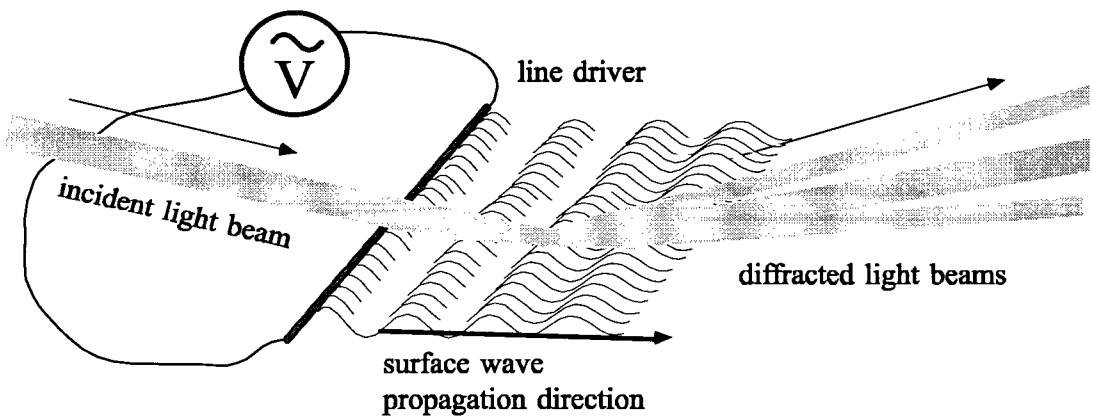

Figure 3-1: Basic geometry of device

This design was conceived for the following reasons: The extremely low Young's modulus of rubber enables a low wave speed and hence, a small wavelength, for the many different types of wave propagation, as described in section 2.3.1. A dynamic, grating with a changeable λ_s and therefore d-spacing can be achieved by changing the oscillation frequency of the line driver, according to Equation (2-12). As will be shown later in this in section, the glancing angle configuration gives a performance boost to the diffraction grating since this makes the diffraction angle more sensitive to changes in the d-spacing.

3.1 Device Parameters

In order for a traveling wave to diffract an obliquely incident laser or light beam, there are several basic requirements for a noticeable effect to be a achieved. The undisturbed surface must be optically flat, and the waves must have a small enough wavelength and a big enough amplitude to produce a readily observable diffracted beam.

The silicone rubber surface, without any wave disturbance, must be considered sufficiently flat that at glancing angles of incidence it produces a good reflected image of the incident beam. Ideally, this would be viewed as a clear, distinct spot on a viewing screen behind the device. This is imperative, for several reasons. Firstly the higher order diffraction spots are simply replicas of the zero order spot, and any noise or aberrations in the zero order would be reproduced in the

higher orders, yielding a fuzzy, indistinct diffraction pattern. Secondly, a distorted surface could disturb the propagation of the surface wave.

The angle of incidence of the light beam and the wavelength of the surface wave determine the angular deflection of each of the orders of diffraction as per Equation (2-2). Figure 3-2 shows the wavelength dependence of the angular deflection of the $m = 0$ beam at various angles of incidence. As previously mentioned, it shows that the bigger the incident angle, the bigger the angular separation of the first order spots. It can be seen that the angle of incidence can be optimized given the available range of surface wavelengths in the device. Notice, also, that because there is an oblique angle of incidence, the angular position of the diffraction spots are not symmetric around the zero-order spot. This is not a problem, as only one of the first order spots need be measured.

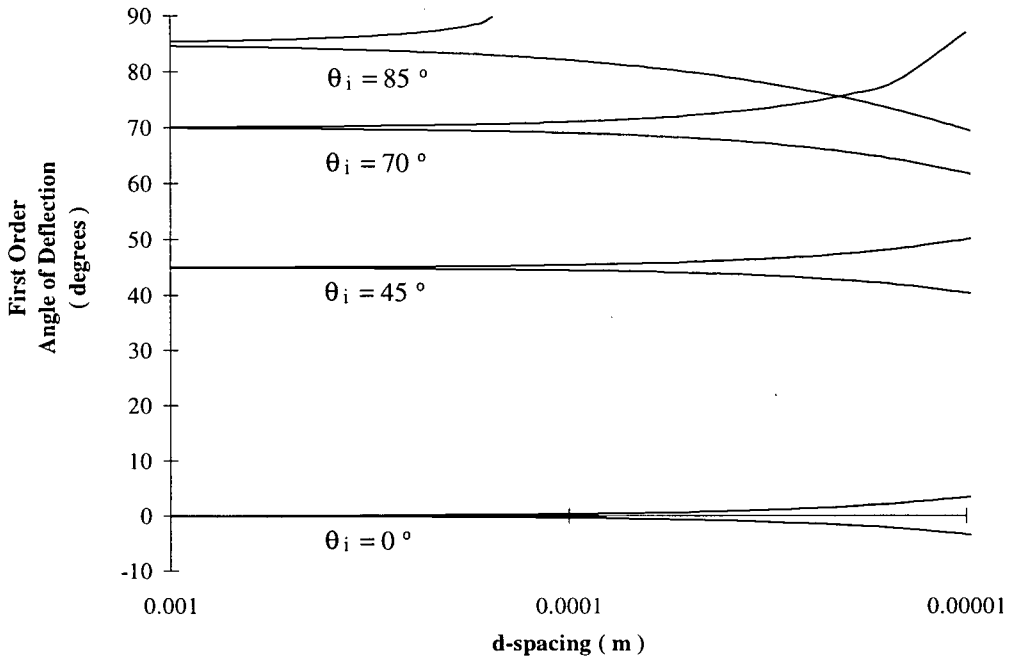

Figure 3-2: Wavelength and θ_i dependence on angular deflection of first order

We must consider what will be an acceptable wavelength in order to efficiently diffract the incident light. Our goal for the device was to reach a surface wave wavelength of 10 to 100 times the wavelength of the incident light. The minimum wavelength is limited by the response of the device at the higher frequencies. Even if the minimum achievable wavelength is relatively big, resulting in small angular deflections, the diffraction effect can be measured by using telescopic lenses, or by imaging the pattern at a sufficient distance from the device.

In order for the intensity of the diffracted wave to be reasonable fraction of the incident intensity, the surface wave amplitude must be of the order of a wavelength of the incident light. From a practical point of view, the device must be able to produce a sufficient amplitude over a range of frequencies, corresponding to a range of different operating wavelengths. The results of a scalar diffraction model are presented in section 5.2.1. In that study, the wave amplitude and damping were varied to see the effect on the relative intensity of the higher order diffraction spots. That work suggested that it should be possible for the arrangement of Figure 3-1 to yield observable diffracted waves.

3.2 Device Design

3.2.1 Preliminary Designs

Several attempts at surface wave propagation in silicone rubber were made before the best performance criteria were met. They include a surface Rayleigh wave traveling in a piece of bulk silicone rubber and surface waves traveling in modes of propagation along the surfaces of a thin slab of silicone rubber.

In the first attempt to propagate surface waves, Rayleigh waves were created on a bulk piece of silicone rubber. Figure 3-3 shows this configuration. The bulk piece of silicone rubber with an optically smooth top surface was attached to the surface of the optical bench. A 10Ω square coil with side length of 28 mm was attached to the surface of the rubber with double-sided tape along the z direction as shown in the figure below. The wire was connected to a function generator so

that a controlled AC current could be applied. A Neodymium magnet was held fixed inside the coil with optical mountings and a clamp where it produced a magnetic field of approximately 0.5 T in the *y* direction. The resultant oscillatory Lorentz force in the wire caused it to oscillate at the frequency of the AC signal in the *x* direction. This movement of the wire actuated the surface of the silicone rubber and launched Rayleigh waves with a wave vector, $\underline{k}$, in the *x* direction. A frequency range of 1kHz to 10kHz was investigated. Given that we expect the Rayleigh wave speed to be approximately 30 m/s, this will give a corresponding wavelength range of 3mm to 3cm.

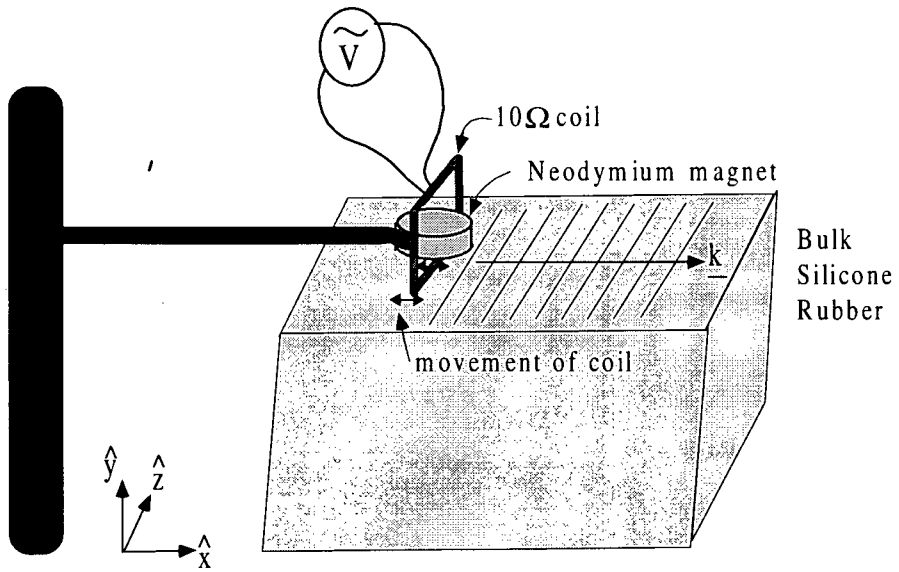

Figure 3-3: Means of launching Rayleigh (Surface) waves in bulk silicone rubber

A second investigation involved launching Rayleigh waves into a structure which would provide transverse confinement, as in a wave guide. We attempted to obtain such confinement on the top surface of a thin slab of silicone. We reasoned that if the wavelength was sufficiently larger than

the width of the structure, it would efficiently guide the wave along the top surface. Figure 3-4 shows the details of this design. Samples of dimensions 7.6 cm x 2.5 cm x 0.3 cm were created from various types of silicone rubber and mounted on a base that was attached to the *xy* translation stage. A piezoelectric stack which changes its length in response to an oscillating voltage served as the means of actuation. It was held fixed in place and attached with double sided tape to the top of the slab so the direction it lengthened was parallel to the *x* axis, as indicated in Figure 3-4. This will launch a Rayleigh wave along the top surface with a wave vector, $\underline{k}$, in the *x* direction. The frequency response of the piezoelectric stack is good up to around 20 kHz. A range of frequencies between 1kHz and 20kHz was therefore investigated. This will produce a range of wavelengths from about 3 cm to 15 mm.

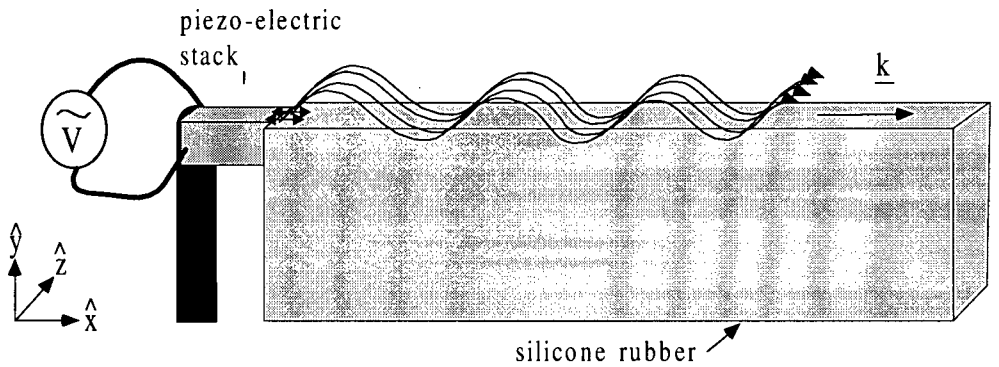

Figure 3-4: Means of launching Rayleigh wave on silicone slab

The penultimate design idea involved using a wave mode of the thin silicone slab to create a 'wiggling' motion such that there would be a transverse wave traveling along the top surface of the slab. Figure 3-5 shows the configuration of this experiment. Samples of size 7.6 cm x 2.5 cm

x 0.15 cm were created from various types of silicone rubbers. The piezoelectric stack was again used as a means of actuating the wave, though in this case it was positioned along the side, close to top of the slab so that the direction it lengthened was in the z direction. It was thought that this would launch a transverse wave with its main deflection vector in the z direction and wave vector in the x direction. In this configuration the incident light beam would be focused onto the side face of the slab, close to the top surface, where the biggest amplitude would occur. Since this idea would use one of the 'modes' of wave propagation of the slab, it would be much more dependent on the geometry of the slab and subject to resonance and standing wave phenomena.

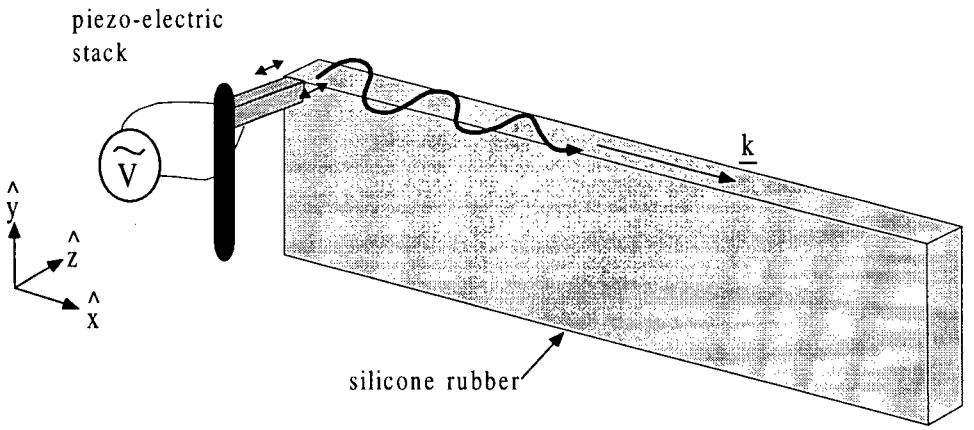

Figure 3-5: Means of launching transverse wave mode in silicone slab

3.2.2 Plate Wave Device

The final design used a thin membrane of silicone rubber supported from below with water. Figure 3-6 shows a cross-section in the *xy* plane of how the plate waves were propagated in the membrane. A single strand of 38 gauge insulated wire was attached to the surface with a small amount of silicone rubber and given an alternating current from a Kepco power supply. A Neodymium magnet was orientated such that the magnetic field was strongest in the *y* direction and was held fixed in place above (or below) the surface of the membrane. The interaction of the AC current in the wire with the magnetic field caused the wire to vibrate back and forth in the *x* direction. This launched plate waves in the membrane with a wave vector, $\underline{k}$, in the *x* direction and the bulk of the deflection in the *y* direction. Since currents above 1 Ampere tended to burn out the wire, the maximum displacement from the wire was limited, especially at the higher frequencies.

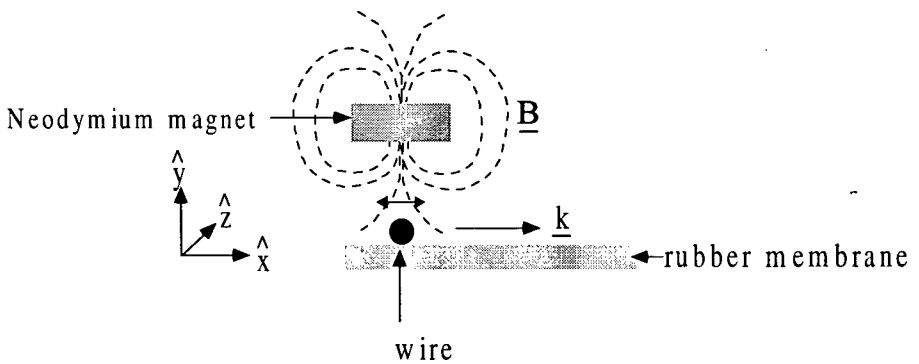

Figure 3-6: Side view of wire actuating rubber membrane

Figure 3-7 shows two of the configurations that were used with this design. The first, Figure 3-7a shows a membrane, attached to a cylindrical, fixed diameter support. The magnet was held suspended above the wire, as close to the membrane surface as possible, while still allowing enough clearance for an obliquely incident laser beam. In this case the tension in the membrane is fixed and is a result of the conditions under which the silicone was cured. The inside of the cylindrical well was filled with water, and a syringe (not shown) was attached and sealed to a hole in the side to allow for minute adjustments to the amount of water inside. It was found that over time the water evaporated, probably through the porous membrane, and it was necessary to adjust the amount of water inside the well to ensure that the top surface of the membrane was lying flat. The second case, depicted in Figure 3-7b shows the membrane attached to a mounting which allows for the width of the membrane in the propagation direction of the wave to be altered. This was achieved by simply connecting two aluminum angle wedges (flat side up) with a long screw. The distance between the two pieces is held fixed with two nuts, the position of which can be adjusted. This width adjustment has the effect of reducing (or increasing) the membrane tension in the propagation direction. Since we discovered that the tension in the membrane contributed to the wave speed in the membrane, reducing the tension allows for us to reduce the wave speed. In this configuration, the magnet can sit below the surface of the membrane allowing for easier access for the obliquely incident laser beam. The whole device must sit in a container in which the water level is increased to the bottom surface of the membrane.

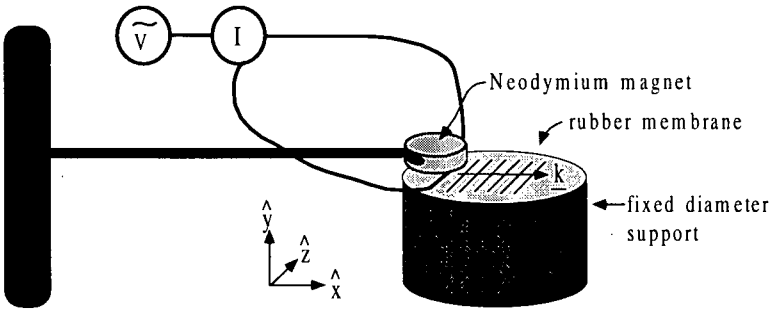

(a) fixed diameter support mounting

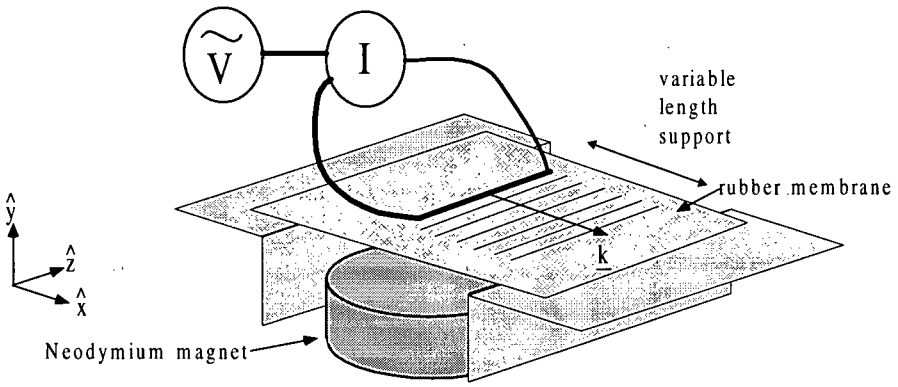

(b) variable length support mounting

Figure 3-7: Means of launching plate wave in thin silicone membrane

Since according to Equation (2-11) the plate wave speed is proportional to the membrane thickness, by reducing the thickness we can reduce the wave speed. Therefore, a design criteria of the plate wave device was to create membranes that were as thin as possible. Luckily, one of the advantages of using silicone rubber as the wave medium is the ability to easily mould it into any desired shape. A procedure was developed to produce thin optically smooth membranes from

silicone rubber. This procedure was devised through considerable experimentation, effort and failed attempts, but provided us with the means to successfully complete this project.

The thin membranes of silicone rubber were created using the following procedure. A smooth sheet of clear 75 μm thick mylar of was cleaned and laid on a clean piece of glass. Then two strips of a spacer material of the desired membrane thickness were laid on the clean mylar a distance of ~ 3 cm apart. Typical spacer materials used were aluminum foil and brass shim stock. The two-part silicone rubber was mixed according to directions and vacuum de-aired to remove all bubbles. A small amount of this uncured fluid was dripped onto the clean mylar between the two spacers. A second sheet of clean mylar was then placed on top, over the silicone rubber and taped down by its edges to the supporting glass plate. A clean, smooth steel rod of ~2cm diameter was used to roll out and smooth down the silicone between the two mylar sheets. The sample was then trimmed down and placed between two clean pieces of thick glass and put under pressure in a vice to squeeze the silicone down the thickness of the spacers. The samples were then either left over night to cure or were cured in an oven at a temperature of 200°F. Once the samples were cured, they were mounted by first peeling off one side of the mylar, while leaving it attached to the other side. This would leave one side exposed, available to be mounted with the use of more silicone rubber on a support. When this "glue" to the support was cured, the second sheet of mylar could be peeled off carefully, leaving the intact membrane attached to the support. With this method we could routinely generate membranes with $t \geq 6$ μm which varied in thickness by not more than ± 2 μm.

As mentioned earlier, one of the advantages of this design is that, as per Equation (2-11), the wave speed can be adjusted by selecting the thickness of the membrane. Since the speed of sound in water (1480 m/s) is considerably higher than the achievable wave speeds from this device, the acoustic energy in the wave is not lost to the surrounding fluid and the wave is guided along the membrane with minimal radiative energy loss.[19] Furthermore, the water loading of the membrane increases its effective density since the membrane has to move a certain portion of the water directly underneath itself. This gives a further reduction in the wave speed from that of an air supported membrane. Further, the wire actuator, attached to the thin membrane, is able to actuate the surface more effectively due the lower mass of the membrane compared to bulk silicone rubber. Finally, the wire can be positioned in contact with the water, which can remove heat more effectively, making higher currents practical.

3.2.3 Additional Considerations

This design inherently has a number of parameters that can be adjusted to further enhance its performance. It can be seen from Equation (2-11) that the speed of the plate wave is proportional to the square root of the Young's modulus. While the Young's modulus does not have a rigorous definition when discussing the elasticity of rubber, a value can be assigned that makes sense relative to other rubbers, such that using a silicone rubber with a low modulus or low Shore A hardness, would reduce the wave speed relative to using one with a relatively higher one. An artifact of the manufacturing process of the thin membranes is that the membranes are left with a certain amount of inherent tension. This tension introduces a term into the wave speed, as per

Equation (**2-11**), which increases the wave speed. By eliminating, or reducing this tension in the films by the method described in section 3.2.2, the minimum wave speed for a given thickness and type of membrane can be achieved.

4. MODELING METHODS

The structures described in the previous chapter were modeled in three different ways. First a scalar diffraction model was constructed to predict the diffraction patterns expected for diffraction of light from a given surface deformation. Secondly, a finite element analysis was carried out in order to predict the expected behaviour of the rubber under the different types of wave propagation. Third, for the case of the plate waves in membranes, predictions were made for the dispersion relationship using existing theoretical results.

4.1 Diffraction Grating Model

A scalar diffraction model was constructed to model the scattering of incident light from an array of scattering points numbered from $i = 0$ to 50. These points were arranged in assigned displacements in a decaying sinusoidal pattern such that the profile of the points represented four wavelengths of a traveling surface wave. The following parameters were varied: the wavelength of incident light, λ_l, the angle of incidence of light, θ_i, the initial amplitude of the wave, A_o, the attenuation of the wave, $tan\delta$, and the wavelength of the traveling wave, d. The diffraction pattern is created by calculating the path length and phase difference, φ_i, for a ray impinging on a scatter point, i, at the angle of incidence, θ_i, and scattering at an angle, θ_d. The details of the calculation of the φ_i for scatter from a given point are given in Appendix B. For a given θ_d, the $cos(\varphi_i)$ and $sin(\varphi_i)$ are summed over the contributions from the scatter from each point in the

array. The relative intensity of the light at the given θ_d is then given by Equation (4-1). A plot of the relative intensity versus angle will give the distribution of the higher order diffraction peaks surrounding the zero-order peak situated at $\theta_d = \theta_i$. Figure 4-1 shows the basic configuration of the model.

$$I(\theta_d) = \sqrt{\left(\sum_{i=0}^{i=50} \sin(\varphi_i)\right)^2 + \left(\sum_{i=0}^{i=50} \cos(\varphi_i)\right)^2} \qquad (4\text{-}1)$$

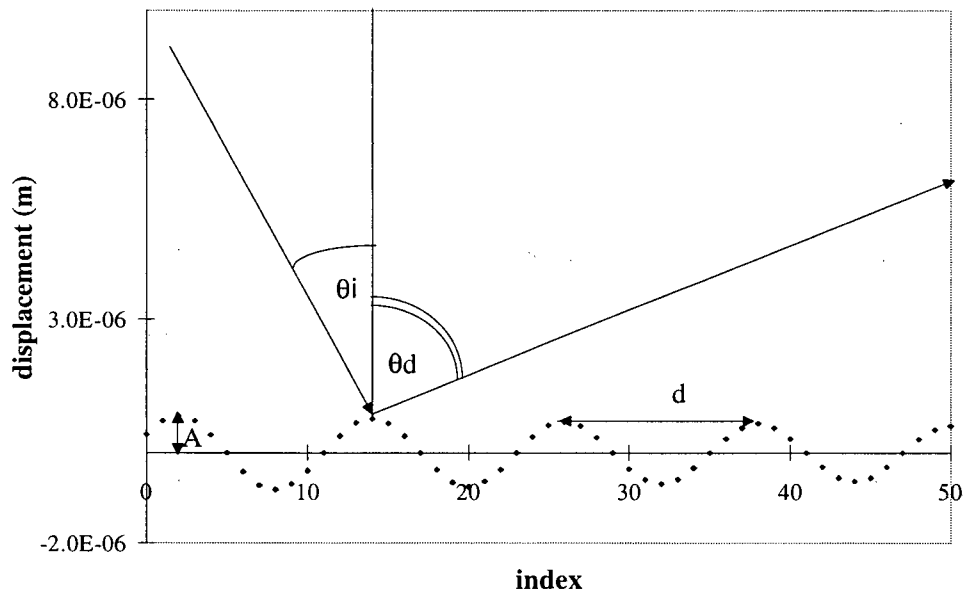

Figure 4-1: Scalar diffraction model configuration

This model is useful in several ways. Firstly, a replica of the wavelength, amplitude, and attenuation of the experimentally created rubber surface wave can be modeled. The scalar

diffraction pattern created from the model can then be compared to that of the one created experimentally. Note, that although this is a scalar model and light is a vector, this should give a reasonable representation of the diffraction pattern, since the key issues are the geometry of the surface and the relative phase of the scattered light. Additionally, the effect of wave amplitude and attenuation on the relative intensity of the different orders of diffraction can be explored. The results from this analysis are discussed in section 5.3.

4.2 Finite Element Modeling

Finite element modeling (FEM) is a useful tool which allows for the investigation of general mechanical properties without having to build and test complete devices. It was used to do a comparison with three of the silicone rubber structures constructed and tested in this research: thin slab Rayleigh waves, transverse thin slab waves and water supported plate waves. A 3D analysis was necessary for the thin slab models. However, for the water supported membranes it was sufficient do a 2D analysis by modeling a cross-section in the xy plane and assuming symmetry in the z direction. In all cases, the actuation of the device is modeled with a harmonic analysis which sinusoidally varies a given load on the model at a specified frequency.

Parameters must be input into the FEM model to describe the mechanical properties of silicone rubber. As discussed in section 2.2.1, rubber is an inherently non-linear material over large deformations. However, since all the surface waves investigated in this research had amplitudes much smaller than their wavelengths, the silicone rubber was treated as a linear elastic material

which required as material parameters the specification of Young's modulus, Poisson's ratio and density. Since the Young's modulus for most of the rubber used in this study was not known, a value was estimated based on the White/Wenzel model fits discussed in section 5.1.4. A Poisson's ratio of 0.4999 was used (since ν=0.5 causes a division by zero error in the software). Finally, the silicone density was taken from the material data sheets supplied with the rubber.

To give an idea of how the surface wave was propagated in the model as a result of the applied loads, a deformed shape of the model can be printed. This is often scaled up and shows for a moment frozen in time, the degree of deformation of the model. A contour map can be overlaid on top of the deformed shape which can show the degree of displacement in a specified direction, indicated by different shades of colour, or grey-scale.

To determine the wave speed from the FEM model results, a path was defined along the top surface of the model. The nodal displacements in a specified direction (*x, y or z*) were mapped onto this path to give a plot of the displacement of this surface as a function of distance. This plot must then be compared and fitted to a sine wave to find the wavelength of the traveling surface wave from the FEM model. These wavelengths predictions will be compared to the experimental results in section 5.1.

4.2.1 Rayleigh wave in thin slab

A rectangular model of dimensions 10 cm x 2.5 cm x 0.31 cm was created with a block mesh of 90 x 20 x 4 elements. To allow a comparison with the RTV655 sample discussed in section 5.1.2, the following material properties were used: $E = 2 \times 10^6$ N/m^2 and $\rho = 1040$ kg/m^3. All nodes on the bottom layer of the xz plane were given zero displacement constraints in the x, y, and z directions. To mimic the actuation of the piezoelectric stack, nodes at the top at one end were given a x displacement constraint with a magnitude of 0.5×10^{-4} m. This model is represented in Figure 4-2. A harmonic analysis was performed for a range of frequencies from 2000 to 6000 Hz. The results are discussed in section 5.1.2.

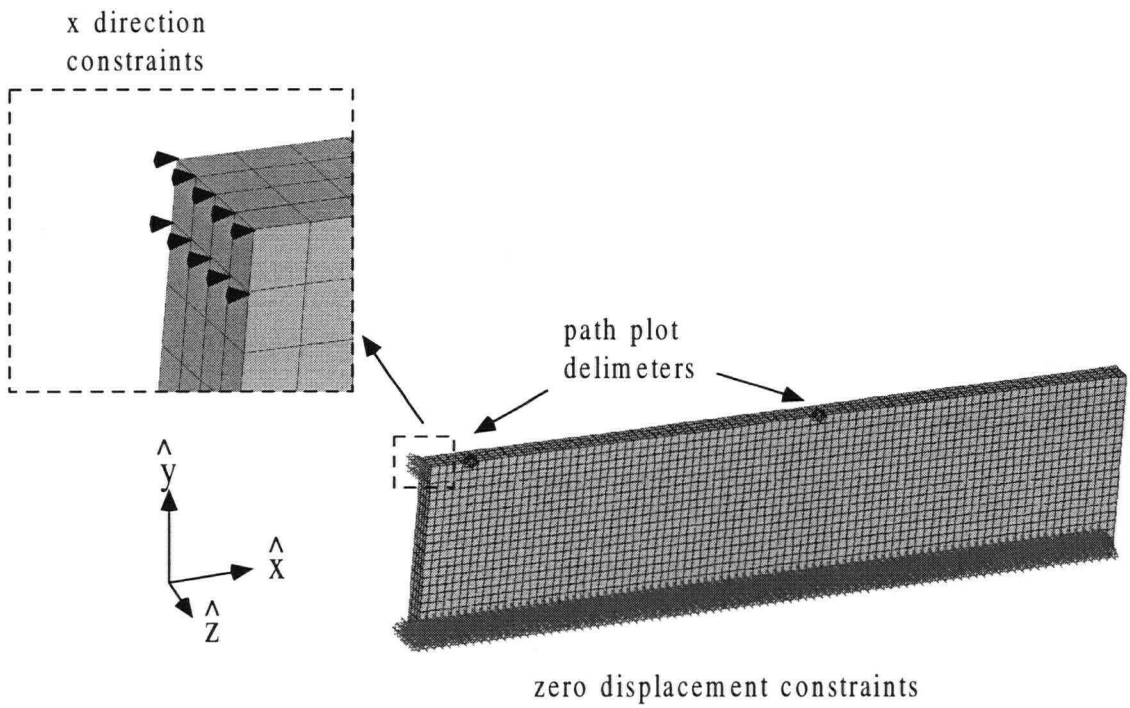

Figure 4-2: Thin slab Rayleigh wave FEM model

4.2.2 Transverse wave in thin slab

A 3D rectangular model of dimensions 7.6 cm x 2.5 cm x 0.15 cm was created with a block mesh of 100 x 25 x 3 elements. To allow a comparison with the RTV31 sample discussed in section 5.1.3, the following material properties were used: $E = 3.5 \times 10^6$ N/m^2 and $\rho = 1420$ kg/m^3. All nodes on the bottom layer of the xz plane were given zero displacement constraints in the x, y, and z directions. To model the actuation of the piezoelectric stack, nodes at the top at one end were given a z displacement constraint with a magnitude of 0.5×10^{-5} m. This model is represented in Figure 4-3. A harmonic analysis was performed for a range of frequencies from 2000 to 5000 Hz. The results are discussed and compared to the experimental results in section 5.1.3.

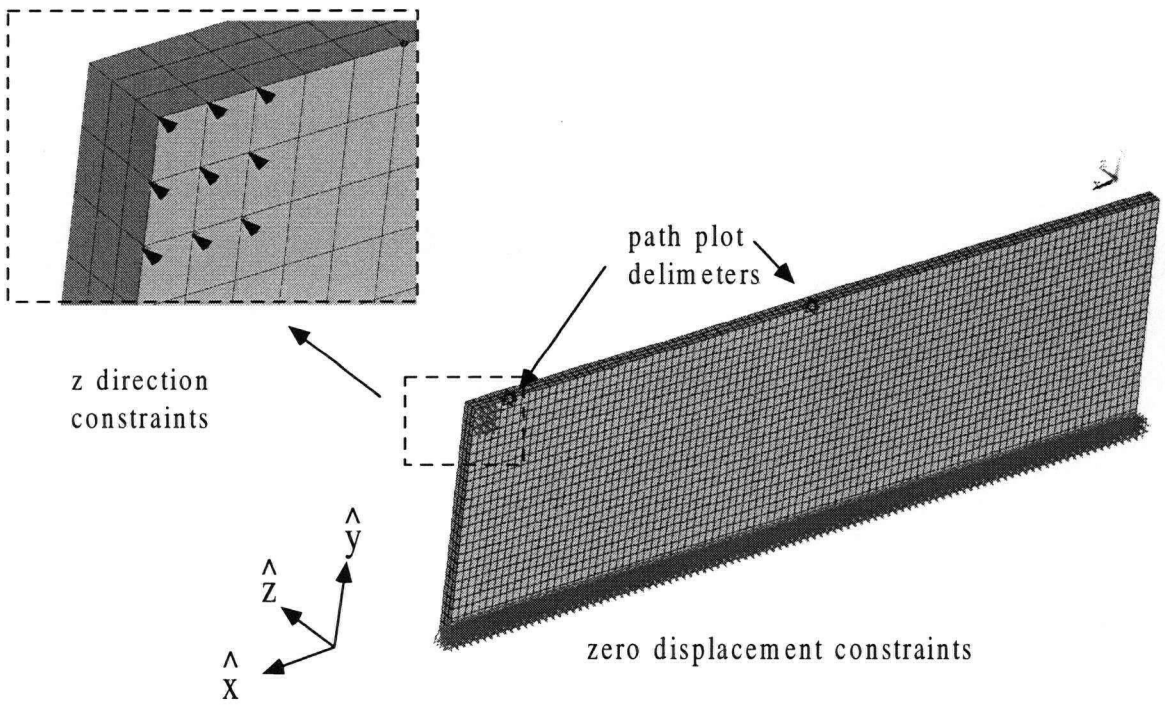

Figure 4-3: FEM model of transversal wave in thin slab

4.2.3 Plate wave in water supported membrane

A 2D model was created with a 25 μm rubber membrane over top of a fluid of depth 1 mm and length 5 mm. The rubber membrane was given the properties of RTV31 with $E = 3.5 \times 10^6$ N/m^2 and $\rho = 1420$ kg/m^2. The water was modeled with a 2D fluid element suitable for contained fluids with no net flow. As its input parameters, the fluid element required the bulk modulus of water, $K = 2.2 \times 10^9$ N/m^2 and the viscosity, $\eta = 1.13 \times 10^{-3}$ kg s/m^2. Several nodes on the top surface of the membrane were given a x and y displacement constraint of 1μm, while all those on the bottom and sides of the water were given zero displacement constraints. A harmonic analysis for a range of frequencies from 1 to 20 kHz was performed. Figure 4-4 shows the FEM model. The results, are discussed and compared with experimental results in section 5.1.4

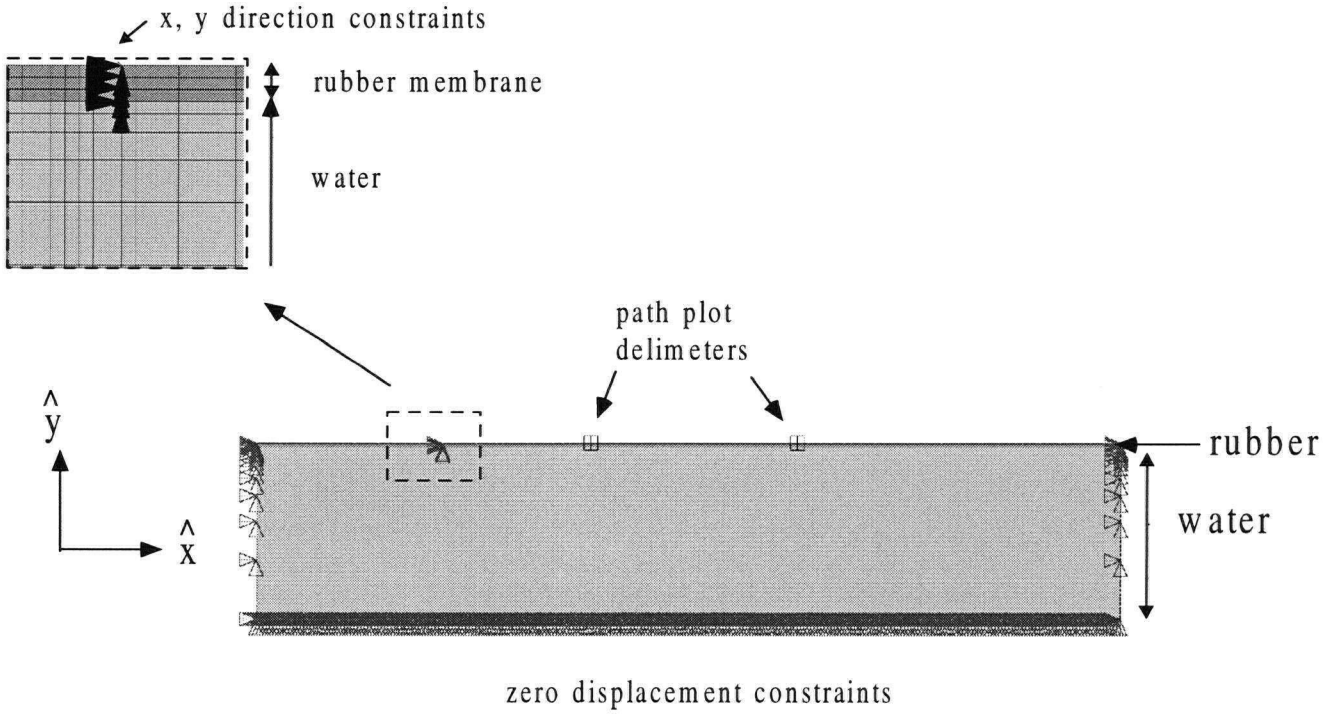

Figure 4-4: FEM model of plate waves in water supported membranes

4.3 Analytical Analysis of Plate Waves

As described in section 3.2.2 the final experimental design used plate waves in water supported membranes. An analytical model is needed to predict the dispersion relationship of this system. Recall that Equation (2-11) gives the asymmetric plate wave speed for a thin membrane, with no boundary conditions. However, the rubber membranes, as an artifact of the manufacturing process, are left with a significant inherent tension which affects the wave speed. The value of tension that will be used is the tension component in the propagation direction. This value, σ, is the force, in the propagation direction, per unit width perpendicular to the propagation direction. Equation (4-2) gives the modification to Equation (2-11) from this tension component, which increases the wave speed.[20] It should be noted that the main factor in this equation is the second one due to the restoring force from the stiffness of the membrane. The membrane tension will increase the wave speed but it is not the dominant factor in the equation.

$$c = \sqrt{\left[\frac{\sigma}{\rho t} + \left(\frac{2\pi}{\lambda_s}\right)^2 \frac{Et^2}{12\rho\left(1-\nu^2\right)}\right]} \qquad (4\text{-}2)$$

The effect of the water loading of the membrane cannot be so easily modeled. A solution to this problem was found in a paper given by White and Wenzel which describes the fluid loading of a silicon nitride Lamb-wave sensor.[21] They give an equation which includes the effect of fluid loading on a plate wave in terms of the speed of sound in that fluid. As long as the speed of the wave in the plate is sufficiently lower than the speed of sound in the fluid, the mechanical wave

can travel in the plate with minimal radiative energy loss.[22] We found that their methodology could also be applied to the case of silicone rubber membranes.

As the plate wave travels in the membrane, it will excite an evanescent wave in the surrounding liquid. The decay length of this evanescent wave into the depth of the liquid, δ_E, is given by Equation (4-3), where c is the speed of the plate wave and c_o is the speed of sound in the fluid. In our case, $c<<c_o$, therefore the depth of water that is being disturbed by the plate wave is approximately $\lambda_s/2\pi$. For example, a surface wavelength of λ_s=300 μm, will give $\delta_E \approx 50\mu m$.

$$\delta_E = \frac{\lambda_s}{2\pi\sqrt{1-\frac{c^2}{c_o^{\,2}}}} \qquad (4\text{-}3)$$

Equation (4-2) can be rewritten in a simpler form as given in Equation (4-4). B is a term which describes the effective stiffness of the plate under tension as given in Equation (4-5) and M is the mass per unit area of the plate as given by Equation (4-6).

$$c = \frac{2\pi}{\lambda_s}\sqrt{\frac{B}{M}} \qquad (4\text{-}4)$$

$$B = \left(\frac{\lambda_s}{2\pi}\right)^2 \sigma + \frac{Et^3}{12\left(1-\nu^2\right)} \qquad (4\text{-}5)$$

$$M = \rho t \qquad (4\text{-}6)$$

We can model the effect the fluid loading has on the plate by adding a term to the mass per unit area of the plate which is the mass per unit area of liquid that is being affected by the plate wave. This term is $\rho\delta_E$, the density of the water times the decay length of the evanescent wave in the liquid. Equation (4-4) then becomes Equation (4-7).

$$c = \frac{2\pi}{\lambda_s}\sqrt{\frac{B}{M + \rho\delta_E}} \qquad (4\text{-}7)$$

Since the wave speed of the waves for the rubber membranes (~ 3 m/s) is well below the speed of sound in air, (c_o=343 m/s), and water, (c_o=1480 m/s), the fluid loading effects on the wave speed of the lowest order asymmetric mode, c, can be calculated from the solution to Equation (4-7). Equation (4-7) can be rearranged to give Equation (4-8). The value of c is readily computed numerically from this relation. We did this using a commercial mathematics software package.

$$\frac{2\pi}{\rho\lambda_s}\left[\left(\frac{2\pi}{\lambda_s}\right)^2\frac{B}{c^2} - \rho t\right]\left[1-\left(\frac{c}{c_o}\right)^2\right]^{1/2} - 1 = 0, \quad c<c_o \qquad (4\text{-}8)$$

For a range of wavelengths, this will yield a range of wave speeds and, hence the dispersion curve. It can be solved for both the cases of water loading and air loading, depending on the value of c_o

used. The results of these calculations are presented in section 5.1.4, and compared to the experimental data.

5. RESULTS

5.1 Surface Wave Measurements

Two methods were used to calculate the surface wave speed. The first method can only be used if the speed is expected to be independent of frequency, as with a Rayleigh wave. The second method measures the wave characteristics of phase and amplitude as a function of distance from the source and, hence, directly determines the wavelength.

The phase and amplitude of the motion were measured with an Angstrom Resolver^{R} Series Dual Channel Model 201 surface motion transducer system which was connected to a Stanford Research Systems lock-in amplifier. The surface motion transducer system employs an optical fiber probe with a central emitting fiber carrying light from a laser diode and surrounding detecting fibers leading back to a photo detector. As the probe is lowered down to a close proximity with a surface (~100-400μm), the magnitude of the collected reflected light varies rapidly with distance away from the surface. The vertical sinusoidal movement of the surface due to the propagating surface wave is thus detected and represented as an AC signal, the amplitude of which will be proportional to the amplitude of the surface wave. The lock-in amplifier detects a response signal at the same frequency as that of a reference signal and gives the amplitude of this signal and the phase difference between the response signal and the reference.

In the case of the Rayleigh wave experiment described in section 3.2.1, it is experimentally simpler to probe the surface at one location and vary the frequency of the source rather than vary the distance away from the source. The phase difference, $\Delta\varphi$ in degrees, a perpendicular distance, x, away from the line driver is given by Equation (5-1). Using Equation (2-12), the wave equation, allows us to find the relationship between the phase difference at a distance , x, and the driving frequency, f, as given by Equation (5-2). The wave speed, c, can be calculated from the slope of the line of $\Delta\varphi$ versus f.

$$\frac{\Delta\varphi}{360^\circ} = \frac{x}{\lambda} \qquad (5\text{-}1)$$

$$\Delta\varphi = \frac{x}{c} f\, 360^\circ \qquad (5\text{-}2)$$

If there is dispersion, it is necessary to use a second method involving the measurement of the relative phase difference between the driving frequency and the surface wave as a function of perpendicular distance from the line driver. The raw data consists of the cumulated phase and amplitude as a function of distance away from the source. From Equation (5-1), the inverse of the slope of the graph of phase difference in degrees versus distance times 360° gives the wavelength of the wave. Care must be taken that data points are measured at points less than a wavelength's distance apart since the relative phase is always represented modulo 360.

Further information can be obtained by plotting amplitude versus distance. First, this gives an indication of how well behaved and stable the surface wave is. If, for example, the amplitude is erratic, the wave could not necessarily be counted on to give a reliable diffraction grating. Ideally, the amplitude should gradually die out exponentially due to the loss mechanisms in the rubber. The size of the damping factor, from Equation (2-15) can be determined by plotting $-ln(A/A_o)$ versus distance, x, calculating the loss wave number from the slope as per Equation (2-14), and dividing by the natural wave number from Equation (2-13).

5.1.1 Rayleigh Wave in Bulk

To measure the wave speed from the Rayleigh wave in a bulk piece of silicone rubber, a device was constructed as described in section 3.2.1, using a cylindrical mold 10 cm in diameter and 2.5 cm deep filled with Silastic T rubber. A 10Ω square coil with a side length of 28mm was attached with double-sided tape to the surface of the rubber. The probe was positioned 2.54 cm away from the line driver. Figure 5-1 shows the phase difference of the response and the driving frequency for a range of frequencies from 1 to 5 kHz. It can be seen that there is a linear region of the graph where it appears that a constant speed Rayleigh wave is propagating. The slope of this linear region was calculated and a wave speed of 27.6 m/s was determined. However, using Equation (2-9) to predict the Rayleigh wave speed based on an estimation of shear modulus from Table 2-1, the wave speed is calculated to be 19 m/s. This may be because the range of wavelengths over this frequency range corresponds to distances comparable to the depth of the

silicone rubber. Hence a pure Rayleigh wave may not be propagating. Nevertheless, this first test was encouraging in that wave propagation was observed at useful amplitudes.

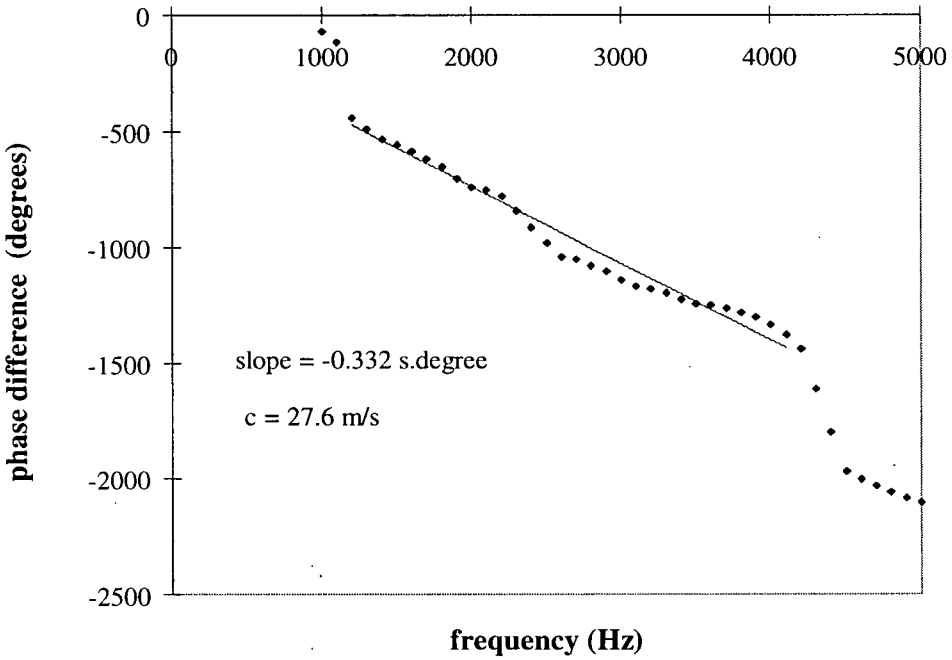

Figure 5-1: Phase difference versus frequency for measured Rayleigh wave

Figure 5-2 shows the amplitude response of the surface wave as a function of frequency. At high frequencies, the response drops off dramatically. This could be for two reasons, first the displacement of the coil due to the Lorentz force drops off as a function of frequency, and secondly there may be a poor coupling of the coil to the surface at higher frequencies.

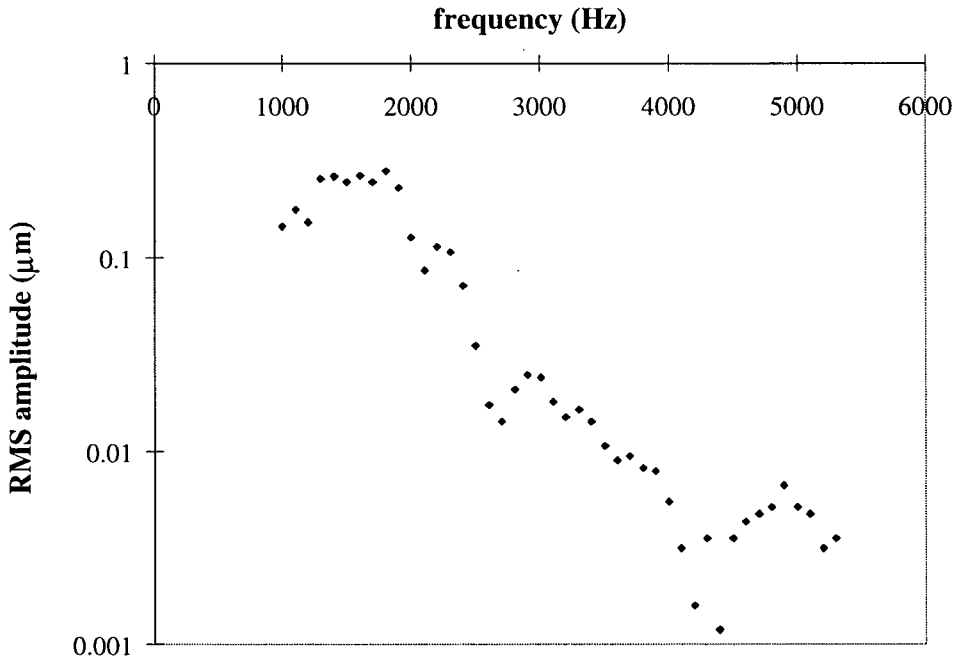

Figure 5-2: Amplitude versus frequency for measured Rayleigh wave

5.1.2 Rayleigh Wave on Thin Slab

The data for the thin slab Rayleigh wave propagation experiments were taken from samples of dimensions 7.6 cm x 2.5 cm x 0.3 cm of several different kinds of silicone rubber. Table 5-1 shows the wave speed, wavelength and damping factor determined for several samples at the given frequencies of operation, according to the procedure described in the previous section. The size of the error bars are determined statistically from the standard errors of the graphs used to determine the values. It can be seen that the wave speed and damping are generally constant at the different frequencies, but tend to rise at the higher frequencies. Notice also that the loss

tangent is high, about 0.2-0.3, which is much higher than would be expected from the intrinsic mechanical loss in the rubber for which the loss tangent is typically or order 0.1. This is probably due to energy leaking into other wave modes along the sides of the slab. Since both the wave speed and the damping is so high, this mode is not suitable to produce a diffraction grating. The lowest wavelength achieved was about 7 mm, but the damping was so high that barely a wavelength of the wave was propagated before the amplitude died out. Figure 5-3 shows the experimentally measured data points for the HSII sample at 3 kHz. The experimentally measured data points of amplitude and phase are compared with the fitted sine wave from the calculated wavelength and damping factor. Figure 5-4 shows, for the same sample, the graph used to calculate the damping factor.

Table 5-1: Wave characteristics for thin slab Rayleigh wave propagation

Silicone Rubber	frequency (Hz)	wave speed (m/s)	wavelength (m)	A_o RMS (μm)	tan δ
RTV 655	2000	37.0 ± 0.4	0.0185 ± 0.0002	0.48	0.20 ± 0.01
	3000	43.2 ± 0.2	0.01439 ± 0.00007	0.70	0.258 ± 0.007
	4000	43.5 ± 0.3	0.01087 ± 0.00008	0.78	0.29 ± 0.01
	5000	41 ± 1	0.0083 ± 0.0002	0.82	0.33 ± 0.03
	6000	45 ± 1	0.0074 ± 0.0002	0.35	0.38 ± 0.03
Silastic T	2000	34 ± 2	0.0171 ± 0.0008	0.37	0.23 ± 0.05
	3000	34.3 ± 0.5	0.0114 ± 0.0002	0.48	0.27 ± 0.03
	4000	36 ± 1	0.0100 ± 0.0003	0.14	0.24 ± 0.04
	5000	44.7 ± 0.4	0.00895 ± 0.00009	0.35	0.18 ± 0.02
HSII	2000	25.2 ± 0.2	0.01262 ± 0.00008	0.04	0.21 ± 0.01
	3000	22.8 ± 0.3	0.0079 ± 0.0001	0.04	0.27 ± 0.02
	4000	25.3 ± 0.2	0.00631 ± 0.00005	0.09	0.53 ± 0.03
	5000	33.4 ± 0.3	0.00668 ± 0.00007	0.13	0.42 ± 0.01
	6000	34.3 ± 0.3	0.00571 ± 0.00004	0.12	0.42 ± 0.01

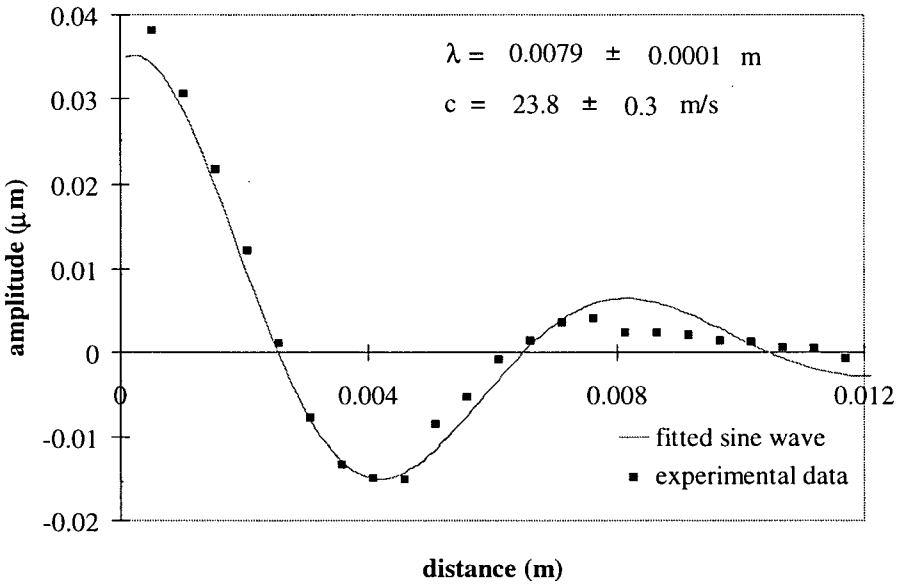

Figure 5-3: Rayleigh wave profile for HSII-1/8" slab at 3 kHz

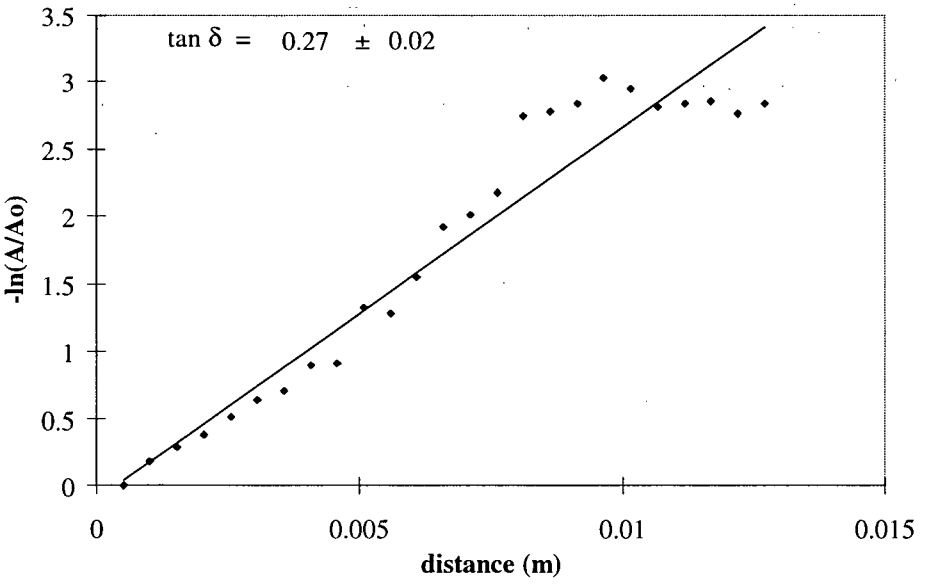

Figure 5-4: Rayleigh wave decay HSII-1/8" thin slab at 3 kHz

As described in section 4.2.1, an FEM analysis was performed on a model of similar dimensions to the physical samples tested in the previous section (the FEM model was a little longer in the x direction). The material parameters of the model were chosen to mimic the RTV655 sample whose results are given in Table 5-1. Figure 5-5 shows the contour map for displacement in y direction on the deformed shape of the sample loaded at 3kHz. Notice that there is a well defined wave traveling along the top surface which dies out exponentially. There is also significant deformation along the side face near the actuated end, indicating that the wave energy is not purely confined to the top surface. This is obviously not a satisfactory system, the traveling wave in Figure 5-6 matches poorly to the sinusoidal fit. However, this motivated the search for a more well-behaved traveling surface wave.

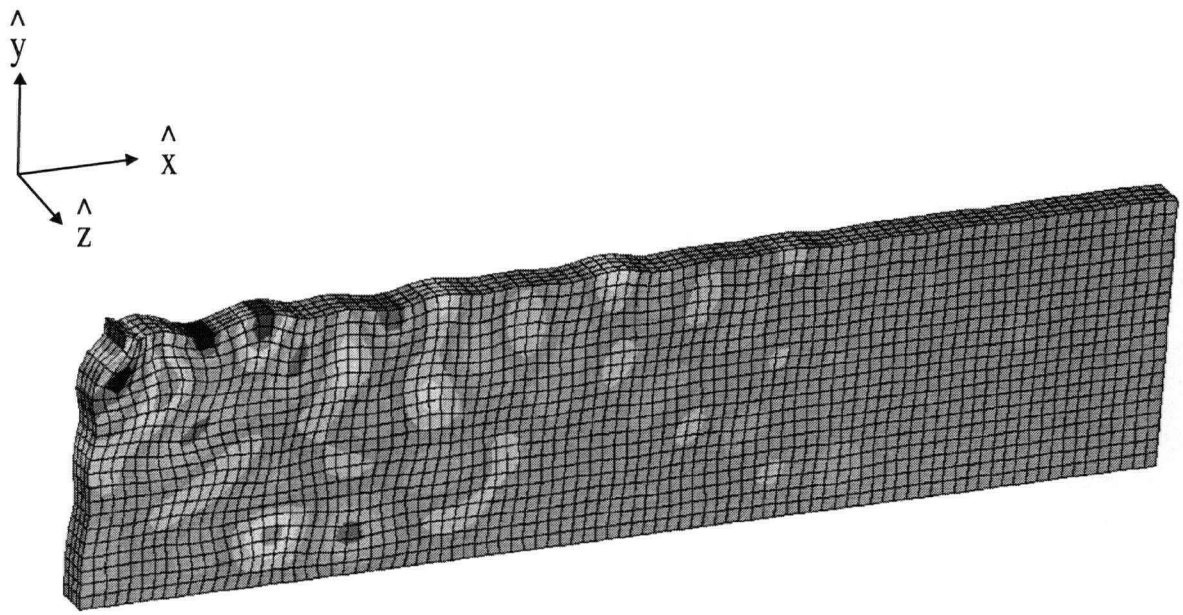

Figure 5-5: FEM deformed shape and contour map in y direction at 3 kHz.

For a driving frequency of 3kHz, Figure 5-6 shows the path plot of the nodal displacement in the *y* direction compared with a sine wave to determine its wavelength. Table 5-2 shows the fitted wavelength and wave speed data derived from the FEM model for frequencies from 2 to 5 kHz. Notice that the resulting wave speeds are considerably lower than the experimentally derived values. This could be due to an underestimation of the Young's modulus in the model. However, these values do follow the same trend that the wave speed increases with driving frequency, at approximately the same rate.

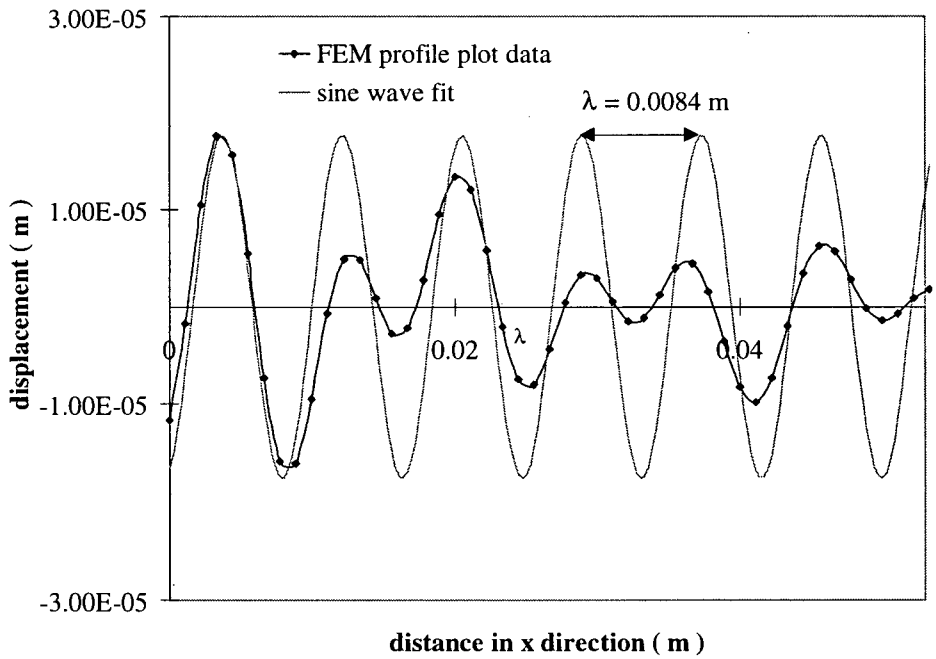

Figure 5-6: Profile plot of thin slab Rayleigh wave FEM model at 3kHz

Table 5-2: FEM results compared with experimental values for thin slab Rayleigh wave.

harmonic frequency (Hz)	λ, wavelength (m)	FEM wave speed (m/s)	experimental wave speed (m/s)
2000	0.0122	24.4	37.0 ± 0.4
2800	0.0089	24.9	-
3000	0.0084	25.2	43.2 ± 0.2
3600	0.0072	25.9	-
4000	0.0065	26.0	43.5 ± 0.3
4400	0.0060	26.4	-
5000	0.0054	26.8	41 ± 1

5.1.3 Transverse Wave in Thin Slab

The experimental data for the transversely loaded thin slabs were taken from samples of dimensions 7.6cm x 2.5cm x 0.15 cm, using several different types of silicone rubbers. Table 5-3 shows the wave speed, wavelength damping factors and maximum measured RMS amplitudes for two different rubbers. In contrast to the previous case, it can be seen that the wave speed has been reduced by about half and the damping factor has been dramatically reduced. The damping of the wave could be entirely due to the intrinsic loss in the rubber and not to loss of wave energy to other modes. This implementation of a silicone rubber surface wave is much more suitable for use as a diffraction grating than the previous case. We were able to observe a diffraction pattern using the Silastic T sample, as is discussed in section 5.2.2. Figure 5-7 and Figure 5-8 show an example of the measured experimental data for the RTV31 sample at 3000 Hz.

Table 5-3: Wave characteristics for transverse wave on thin slab

Silicone Rubber	frequency (Hz)	wave speed (m/s)	wavelength (m)	A_o RMS (μm)	tan δ
RTV 31	3000	16.6 ± 0.2	0.00552 ± 0.00007	0.87	0.03 ± 0.01
	4000	18.1 ± 0.1	0.00454 ± 0.00003	1.00	0.021 ± 0.007
	5000	19.2 ± 0.1	0.00385 ± 0.00003	0.78	0.004 ± 0.007
	6000	20.0 ± 0.1	0.00333 ± 0.00002	0.12	0.032 ± 0.006
Silastic T	2100	16.1 ± 0.1	0.00766 ± 0.00005	0.57	0.055 ± 0.006
	2500	17.9 ± 0.1	0.00716 ± 0.00003	0.47	0.020 ± 0.004
	3000	19.1 ± 0.1	0.00636 ± 0.00003	0.39	0.027 ± 0.004
	3500	20.1 ± 0.1	0.00575 ± 0.00002	0.45	0.036 ± 0.003
	4000	20.5 ± 0.1	0.00512 ± 0.00002	0.61	0.050 ± 0.004

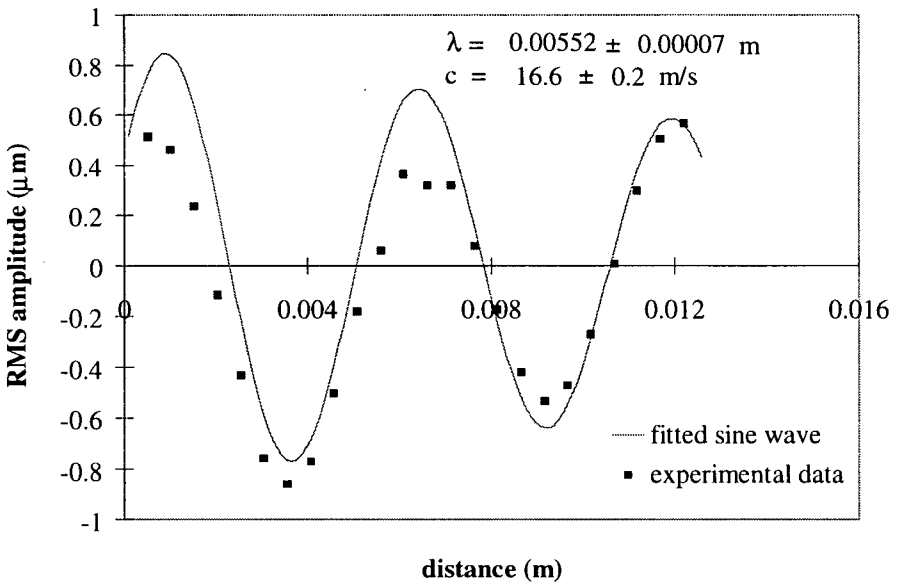

Figure 5-7: Transverse wave profile for RTV31-1/6" slab at 3 kHz

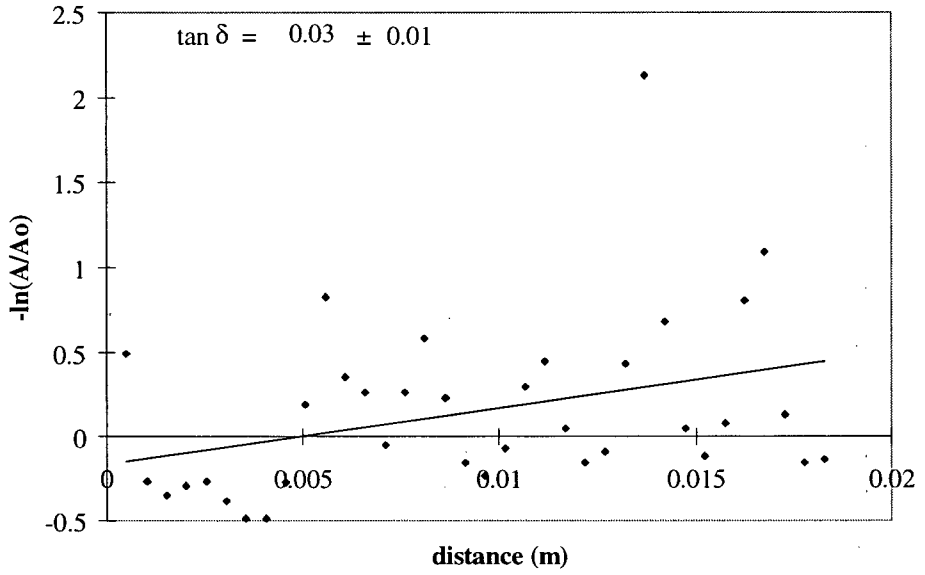

Figure 5-8: Transverse wave decay for RTV31-1/16" slab at 3 kHz

The FEM analysis for the transversely loaded thin slab sample was performed as described in section 4.2.2. The material parameters of the model were chosen to mimic the RTV31 sample whose experimental results are given in Table 5-3. Figure 5-9 shows the deformed shape of the sample at 3 kHz with a contour map of the displacement in the *x* direction. It can be seen that near the end being actuated, there were several well defined wavelengths, however, it doesn't appear that this wave traveled the full length of the slab. Actually, it appears that the main mode that was actuated was a plate wave mode with circular wave fronts originating from the corner being loaded. The measured wave, along the top surface, was simply a projection of the circular wave front along the top surface, which explains why this wave did not propagate along the whole length of the slab.

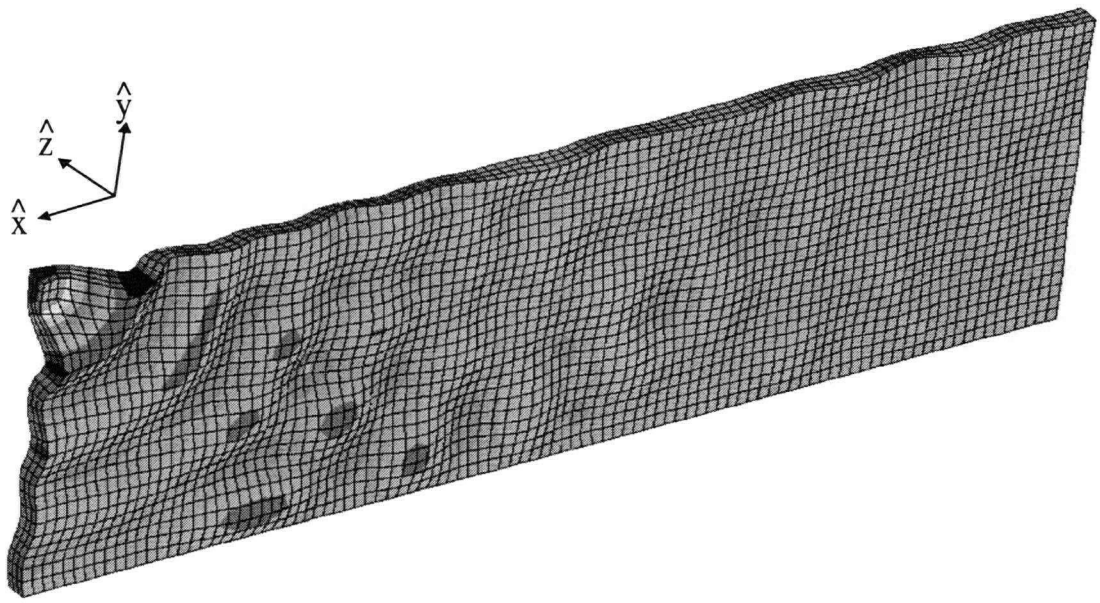

Figure 5-9: FEM deformed shape and contour map of displacement in x direction at 3 kHz

Since it appears that only a few wavelengths of a traveling wave were propagating, the nodal displacements were only taken from the end close to the end being loaded according to the path defined in section 4.2.2. Figure 5-10 shows the path plot data at 3kHz compared with the sine wave used to determine its wavelength. Since, we postulated that this was actually a plate mode of the thin slab the asymmetric plate wave speeds were also calculated from the measured wavelengths according to Equation (2-11). Table 5-4 gives the fitted wavelength and wave speed data from the FEM model and the corresponding pure plate wave speeds. In comparison to the experimental data, at low frequencies, the FEM wave speed is similar, but increases at a faster rate. However, in comparison to the pure plate wave speeds, the FEM wave speed, again starts out at a similar value, but increases at a slower rate. This could be due to the fact that is unlikely that a pure plate wave mode would be able to propagate since the height of the slab bounds the

mode and restricts its propagation. The FEM model shows us which mode of the thin slab is most likely to be excited, and, that it isn't a pure traveling wave mode along the top surface. Hence, this system, despite the fact that we used it successfully as a diffraction grating, is not sufficiently well-behaved, as indicated by the poor match of the sine wave in Figure 5-9.

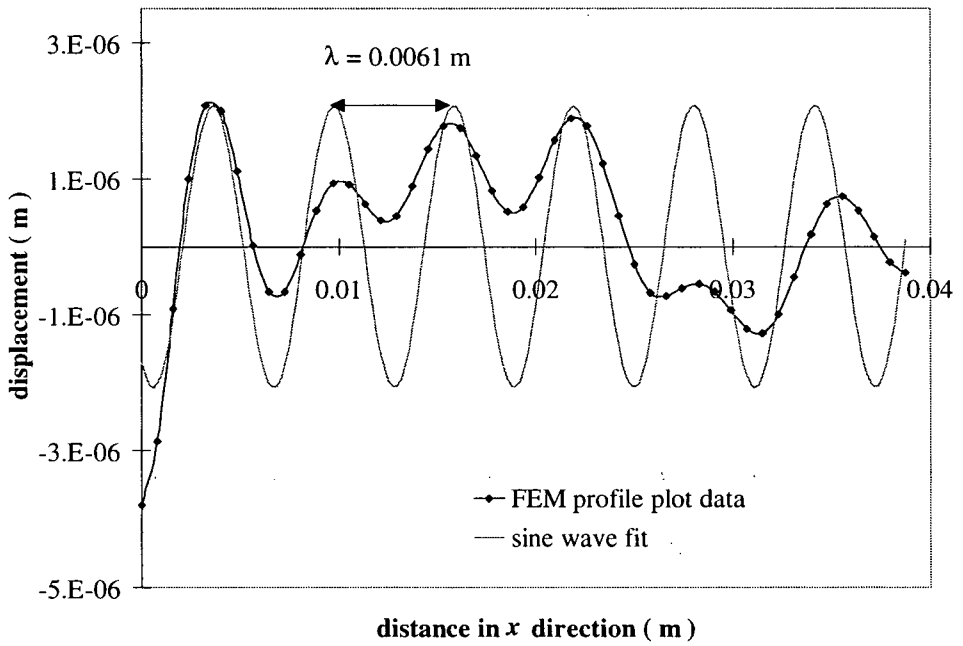

Figure 5-10: Profile plot of transversely loaded FEM model at 3kHz

Table 5-4: FEM wavelength and wave speed results for transversly loaded thin slab.

harmonic frequency (Hz)	λ, wavelength (m)	c, wave speed (m/s)	plate wave speed (m/s)
2000	0.0083	16.6	18.8
3000	0.0061	18.3	25.5
4000	0.0053	21.2	29.4
5000	0.0049	24.5	31.8
6000	0.0044	26.4	34.5

5.1.4 Water supported plate wave device

Numerous samples of the water supported plate wave device were constructed with various thicknesses and types of silicone rubbers. The samples were mounted in two ways. In the first, the membrane is mounted on a round, fixed diameter support, and thus the inherent tension in the membrane from the manufacturing process cannot be altered as in Figure 3-6a. In the second method the membrane is mounted on a variable width rectangular support, which allows the tension in a specific direction to be controlled as in Figure 3-6b.

Figure 5-11 shows the data collected for a sample with an RTV655 membrane having a thickness of ~50μm at 3 kHz. In comparison to the two previous cases, there are noticeable improvements. The propagating wave is very well behaved, with a precisely defined wavelength and damping factor. This is illustrated by the fact that the fitted sine wave is a very good match to the collected experimental data. Also, the wave speed, and subsequently the wavelength, for this mode are reduced by a factor of 10 from the previous cases (~ 3 m/s vs. ~30 m/s). The amplitude, also, is

high enough to be useful as a diffraction grating over many complete wavelengths. Figure 5-12 shows the exponential decay of the wave, and it can be seen that despite the fact that the damping is low, ~1%, there is not a lot of scatter in the amplitude data compared to the previous cases.

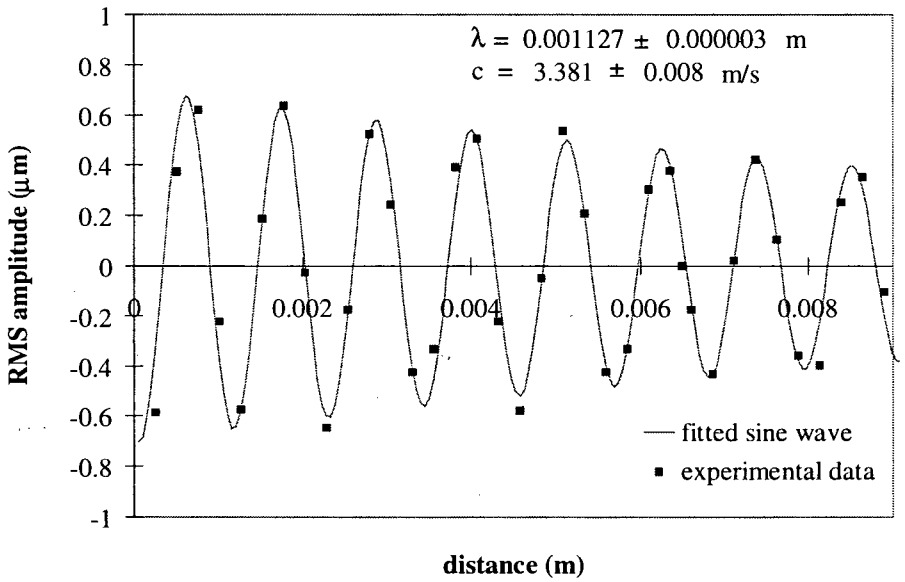

Figure 5-11: Wave profile for an RTV655 0.002" water loaded membrane at 3 kHz

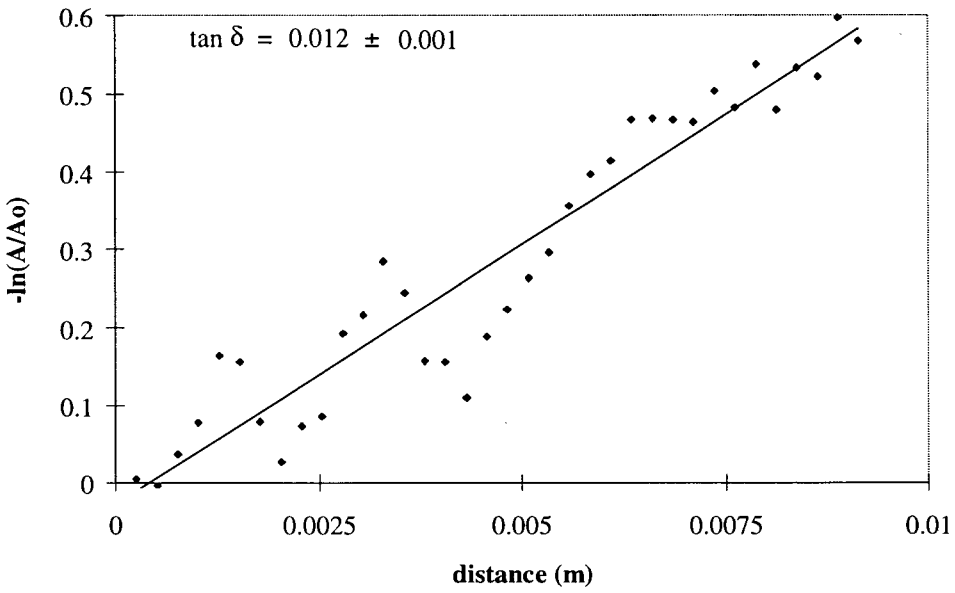

Figure 5-12: Wave decay for an RTV655 0.002" water loaded membrane at 3 kHz

As mentioned previously, these samples should exhibit a wave speed which decreases as the wavelength increases. This dispersion relation was studied by collecting wavelength data at different frequencies, and calculating the wave speed. Comparisons will be made with the White/Wenzel model described in section 4.3, for both air loaded and water supported cases. There are three independent parameters in that model; membrane thickness, Young's modulus and membrane tension. Although, these parameters are independent, the thickness and the modulus are known approximately and the tension can be measured. as will be described in Appendix D. For the various cases to be discussed, the dispersion curves are shown with the calculated curve from the White/Wenzel model. The model parameters are given in a table below each dispersion

curve. Furthermore, comparisons will also be made with the FEM analyses described in section 4.2.3.

The biggest gain in performance for this system is obtained by loading one side of the membrane with water. Figure 5-13 shows the dispersion curves for a sample of RTV31 rubber of ~15μm in thickness. The curve for the air loaded case is flatter at the lower frequencies than the water loaded case and is substantially higher in wave speed for all wavelengths. The solid line shows the data generated from the air loading and the water loading White/Wenzel model with the parameters given in Table 5-5. It can be seen that both curves were fit with a common value for membrane thickness and Young's modulus and only a slight difference in film tension. It is possible that the water loading one side of the membrane affected the surface energy of the rubber as discussed in section 2.2.1, thus slightly reducing the film tension. Alternatively, the presence of water could cause a slight dimensional change in the rubber, which would also change its tension.

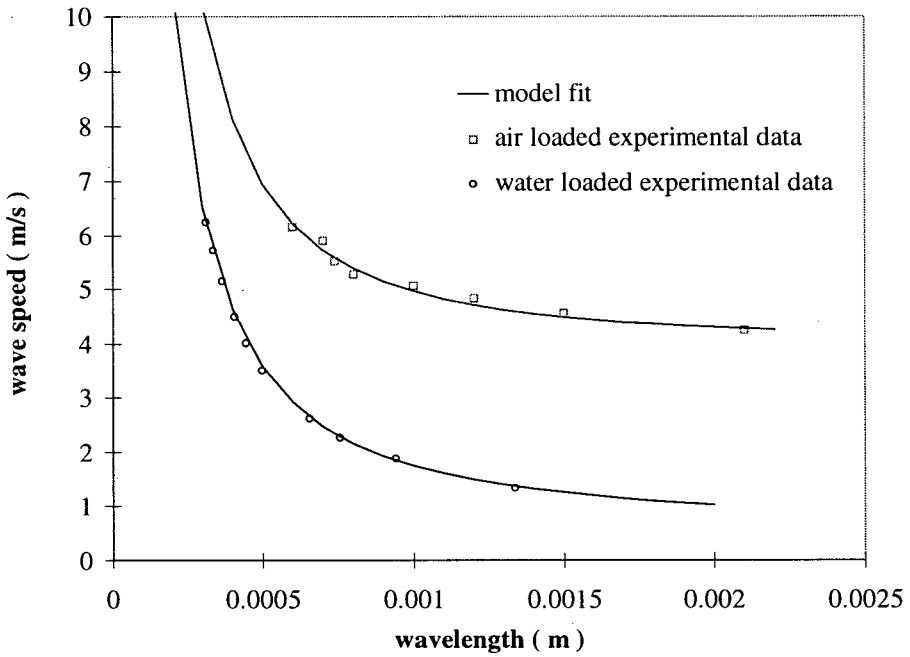

Figure 5-13: Air and water loaded dispersion curves for an RTV31 membrane

Table 5-5: White/Wenzel model parameters for an RTV31 membrane

Loading Fluid	Fitted Thickness t (μm)	Tension σ (N/m)	E (N/m^2)
air	16	0.75	1.3×10^6
water	16	0.65	1.3×10^6

Figure 5-14 shows the dispersion curves for four thickness of RTV655 ranging from 6 - 60 μm. It can be see than with each reduction in thickness there is a significant decrease in wave speed at

any given wavelength. Table 5-6 shows the parameters used to fit the White/Wenzel model to the experimental data. The design thickness indicates the thickness of the spacer used to manufacture the membranes. Also it can be seen that with each reduction of thickness, the tension in the membrane decreases as well. The tension, σ, indicates the tension in the direction of propagation per unit width perpendicular to the direction of wave propagation. Hence, for a given manufacturing process, one would expect that this value be proportional to the thickness, consistent with the trend in the tension values determined from the model. Therefore, a big gain in performance for the device can be expected by using the smallest possible thickness of rubber membrane.

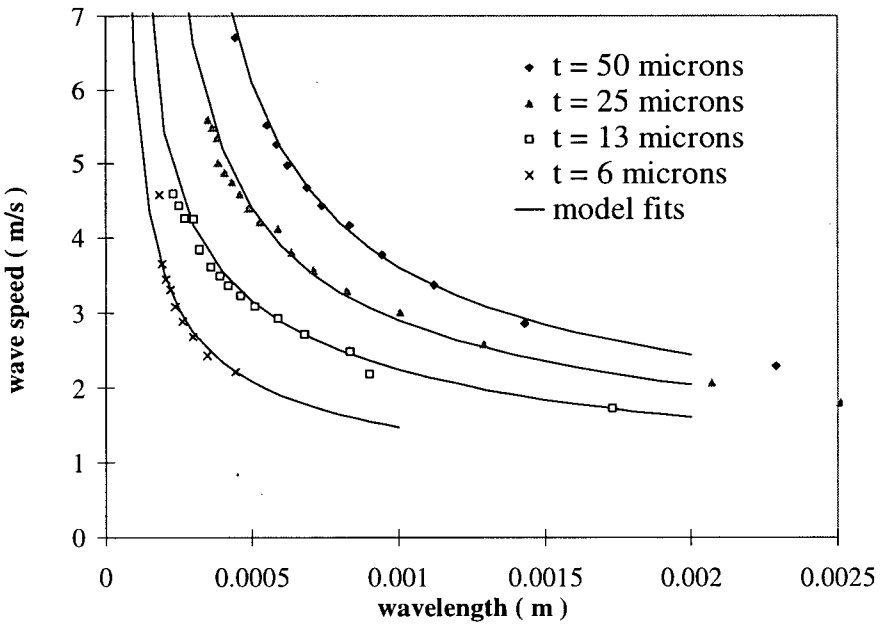

Figure 5-14: Dispersion curves for different thicknesses of a water loaded RTV655 membrane

Table 5-6: White/Wenzel model parameters for different thicknesses of an RTV655 membrane

Design thickness (μm)	Fitted Thickness t (μm)	Tension σ (N/m)	E (N/m^2)
51	42	2.00	2×10^6
25	27	1.40	2×10^6
13	13	0.85	2×10^6
6	8	0.36	2×10^6

It is interesting to note that this effect of the tension on the wave speed was not immediately apparent. The first clue that there might be a significant contribution came with the noted difference between the shape of the dispersion curves for samples of similar thickness which were cured under different temperature conditions. Figure 5-15 shows this difference for samples of RTV31 with thicknesses of ~ 25μm, one cured over-night at room temperature, and the other for 1 hour at 200 °F, or 93 °C. Table 5-7 gives the model parameters that were used to fit the two sets of experimental data. It can be seen that the main difference between the two sets is that the tension for the oven cured sample is higher. This is to be expected since the sample cured at a higher temperature, will expand, cure, and then attempt to contract as the sample is brought down to room temperature.

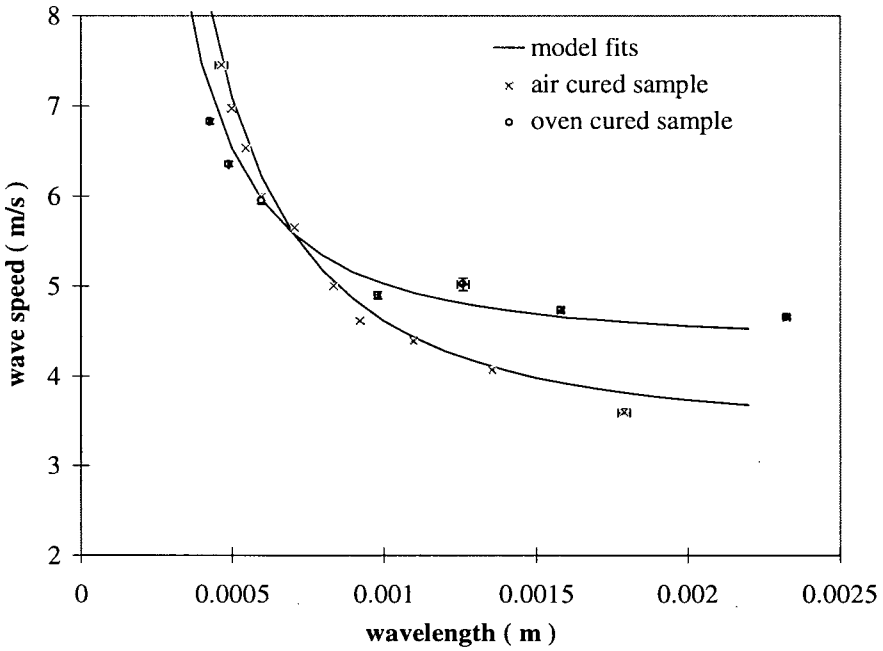

Figure 5-15: Air cured (room temperature) and oven cured dispersion curves for RTV31 samples

Table 5-7: White/Wenzel model parameters for air cured and oven cured samples of RTV31

Cure temperature (°C)	Fitted Thickness t (μm)	Tension σ (N/m)	E (N/m^2)
(air) 20	30	0.5	3.5×10^6
(oven) 93	25	0.7	3.5×10^6

To further test the theory that increased membrane tension affected the wave speed, an air-tight air loaded sample of RTV31 was measured at various minor degrees of membrane inflation. The mounting method depicted in Figure 3-7a was used without the water inside the support well.

The tension in the membrane was increased by pressurizing the air inside of the support well with an attached syringe as shown in Figure 5-16. As the membrane bulged out in response to the increased pressure, its overall length changed and therefore increased the tension. The pressure inside the support well was measured with an attached manometer. Appendix D shows how we can calculate the tension in the membrane from the pressure, P and the increase in membrane height, h. In each case the wave speed was measured at a constant driving frequency of 3 kHz. Figure 5-17 gives the wave speed plotted versus applied differential pressure. It clearly shows that the measured wave speed increases with the tension in the membrane caused by the applied differential pressure.

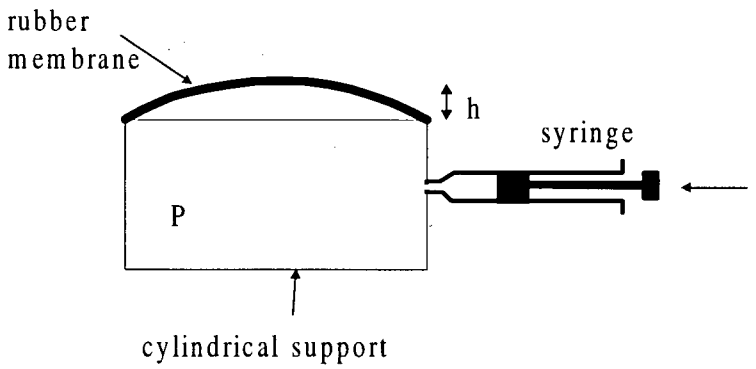

Figure 5-16: Increasing tension in membrane by pressuring air inside support

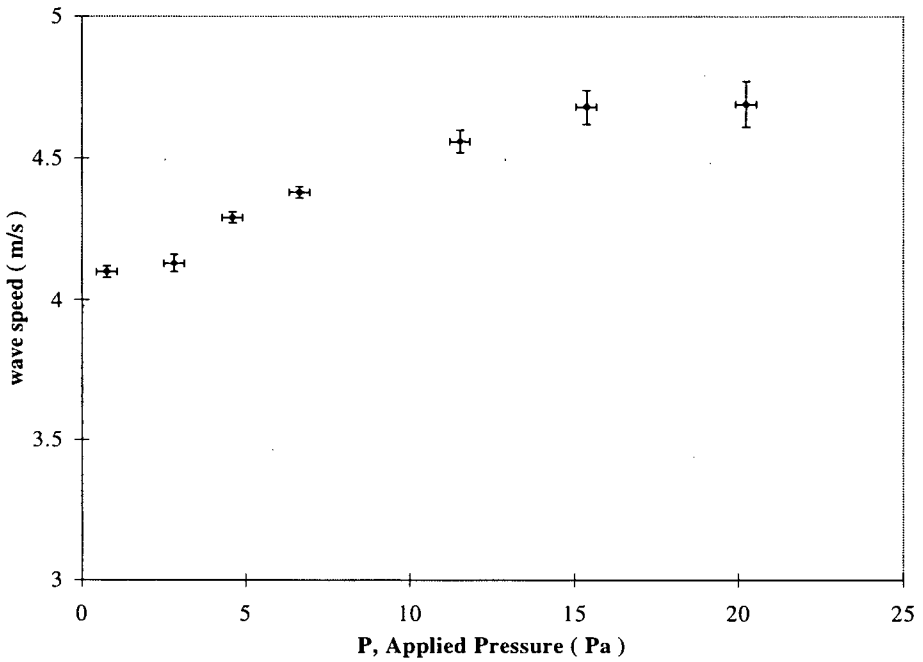

Figure 5-17: Wave speed versus applied pressure at constant excitation frequency of 3 kHz

According to the procedure described in Appendix D, it was possible to calculate the effective total membrane tension at each of these levels of increased air pressure and membrane tension. Figure 5-18 shows the same measured wave speeds versus the calculated membrane tension. Also plotted is a prediction of wave speed from the White/Wenzel model based upon the same tensions. However, in order to match the White/Wenzel model data with the experimental data, a different value of membrane thickness was used (45 versus 25 μm). This could be due to our poor understanding of the way in which waves might travel in inflated membranes, or perhaps the contribution of a some unknown surface energy effects in inflated membranes.

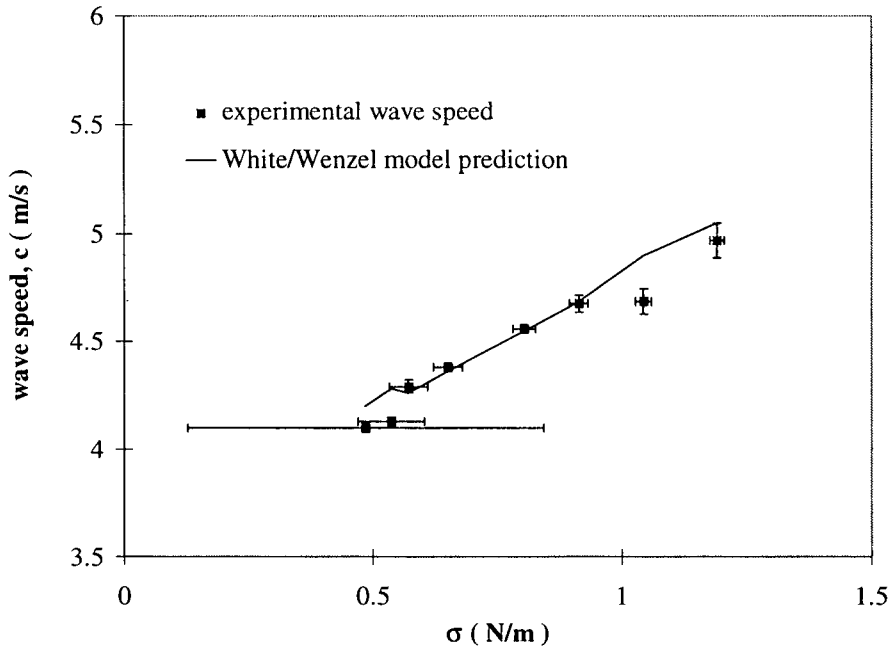

Figure 5-18: Wave speed versus levels of increased tension

Figure 5-19 shows the experimental data and the White/Wenzel fit for the same for the case of zero added pressure. This indicates that there is an inherent membrane tension of 0.45 N/m. The sample was also tested to measure the inherent tension as described in Appendix D. Figure 5-20 shows this data with a fitted parabolic curve to determine the most likely y-intercept (the inherent membrane tension). The fitted curve intercepts the y-axis at 0.47 N/m. Since these two values are close, this is further proof that the White/Wenzel model is providing a consistent description of the behaviour of the elastomeric membranes.

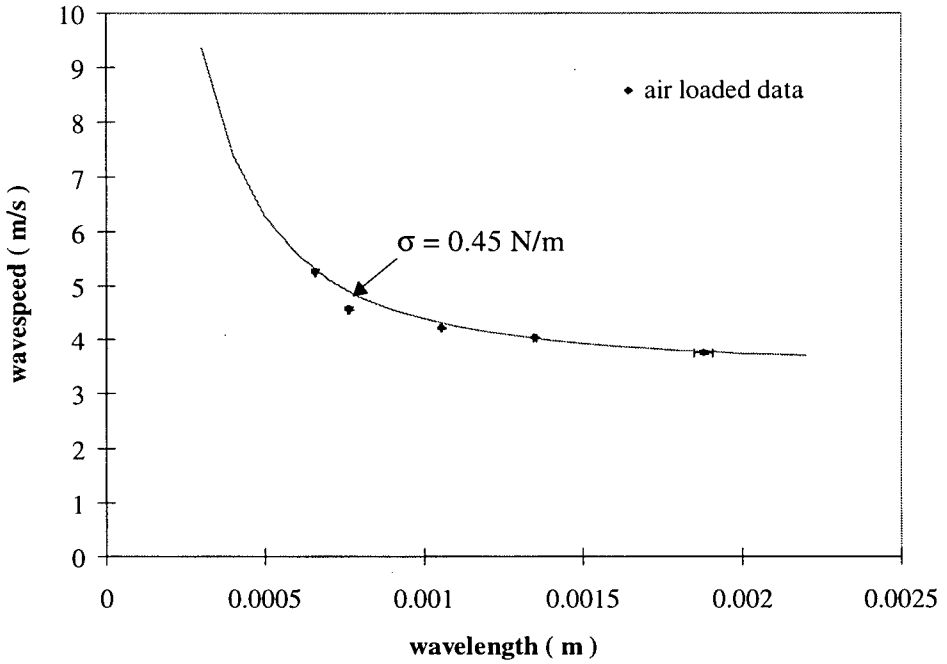

Figure 5-19: Dispersion curve for RTV31 sample at zero added pressure

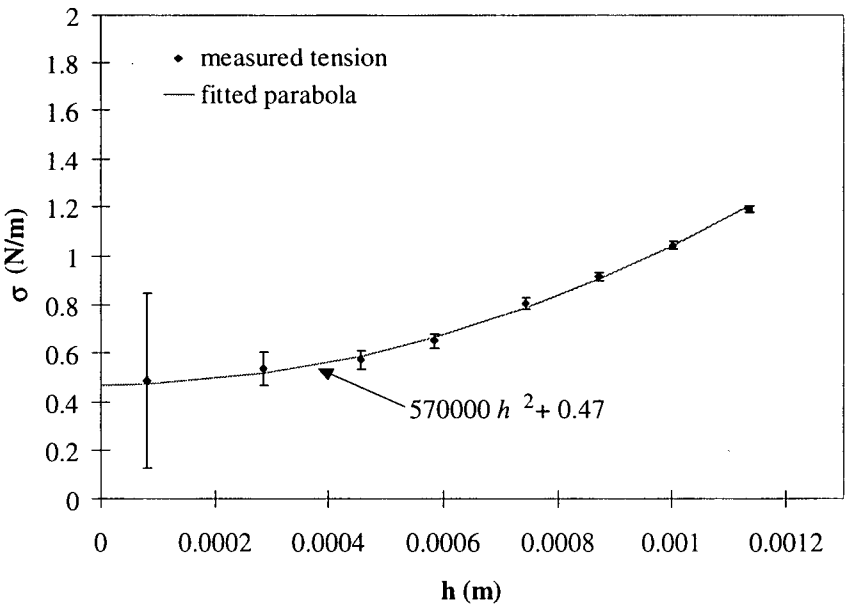

Figure 5-20: Measured tension for RTV31 sample at increased inflations

In order to reduce this inherent membrane tension, we studied the effect of increasing the temperature of a water loaded sample. Increasing the membrane temperature will cause the silicone rubber to expand. However, since the circumference of the membrane is fixed to the support, increasing the temperature would have the effect of increasing the surface area of membrane. If there was any inherent membrane tension, this would minimize the surface area and therefore reduce the tension. The sample was an RTV615 sample with a thickness of ~30 μm. The first data set was taken at a room temperature of 23°C. The second data set was taken with the same sample at an elevated temperature of 51°C. At temperatures above this, there were too many air bubbles generated in the water to give a stable surface to the membrane. Figure 5-21 shows the experimental data along with the fitted curves from the White/Wenzel model. Table 5-8 shows the parameters used to fit the data. It can be seen that the main difference between the two can be attributed to a difference in the tension, of 0.3 N/m. The model parameters indicate that there is also a slight reduction in the Young's modulus. If the tension reduction from a temperature difference of $\Delta T=29°C$ is calculated from the coefficient of thermal expansivity, the difference in tension generated is 0.4 N/m. This is comparable to the difference derived from the fitted model, which is strongly suggestive that the root of the extra term in the wave speed equation is in fact due to membrane tension. However, the benefit from the increasing the temperature to reduce this tension is limited, since it is not practical to raise the temperature much above 50°C.

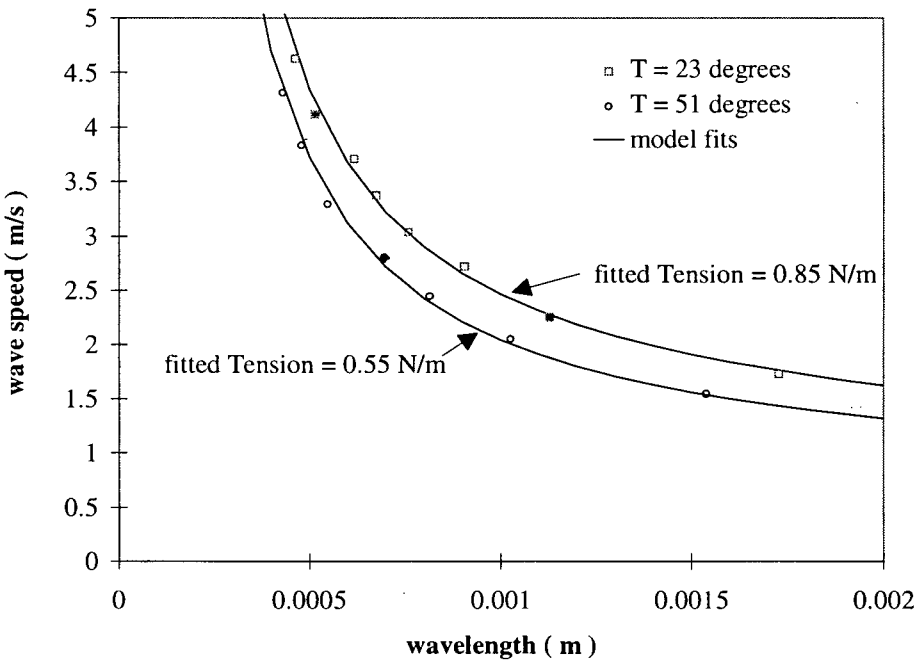

Figure 5-21: Dispersion curves for RTV615 sample at different temperatures

Table 5-8: White/Wenzel model parameters for sample at different temperatures

Sample Temperature (° C)	Fitted Thickness (μm)	Tension (N/m)	E (N/m^2)
23	34	0.85	1.9×10^6
51	34	0.55	1.5×10^6

Since the tension is an obvious contribution to the wave speed of these membranes, in order to minimize the wave speed this tension has to also be minimized. The samples were usually produced under pressure and/or elevated temperatures, therefore it seems unlikely that samples

produced under this methodology will be tension free. We therefore sought an alternate, mechanical means to eliminate the tension. It would be difficult to completely remove all the tension in the membrane in an isotropic fashion. However, it was noted that only the component of tension in direction of propagation of the wave influences wave speed. Hence, to reduce the wave speed it is necessary only to remove the tension in this direction, and this can be done by allowing the rubber to shrink in one dimension. This was done with the simple mounting apparatus shown in Figure 3-7b and the procedure described in section 3.2.2.

Figure 5-22 show the dispersion curves for a sample for various degrees of tension reduction. Table 5-9 shows the White/Wenzel model parameters used to fit the data from the experimental curves. It can be seen that with each reduction in length the tension, also, is reduced. The sample measured with the lowest tension, was actually floating on the surface of the water. The remnant modeled tension therefore, must be attributed to some sort of surface energy in the rubber, or surface tension in the water. This is not unreasonable as the surface tension of an air-water interface at room temperature is 0.023 N/m and the surface tension of the silicone/water interface is 0.0204 N/m. This suggests that in a future investigation, studies of this intrinsic tension as a function of fluid chemistry are warranted.

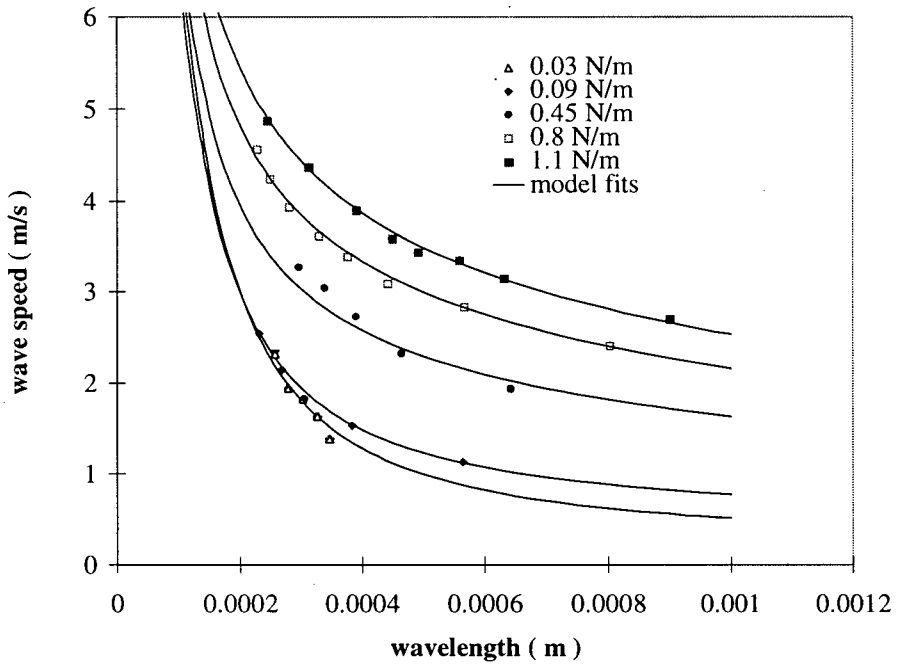

Figure 5-22: Dispersion relationships for HSII sample at different tensions

Table 5-9: Parameters for HSII sample at different tensions

Tension (N/m)	Thickness (μm)	E (N/m^2)
1.10	14	0.9×10^6
0.80	14	0.9×10^6
0.45	14	0.9×10^6
0.09	15	0.9×10^6
0.03	16	0.9×10^6

It has been shown that the White/Wenzel model is a reliable and consistent way of describing the water loaded silicone rubber membranes being used in this experiment. Knowing the membrane

thickness, rubber modulus and membrane tension is sufficient to completely describe the behaviour of surface waves propagating in water loaded membranes.

As described in section 4.2.3, an FEM analysis was performed to model a 25 μm RTV31 membrane supported with water. Figure 5-23 shows the deformed shape results with a contour map showing the degree of displacement in the *y* direction. This shows that there is a very well defined wave traveling along the surface of the rubber/water interface. The shaded arcs underneath the membrane also indicate that the there is only a small layer of water which is actually being moved by the traveling wave. Furthermore, it shows that the thickness of this layer is comparable to the wavelength of the traveling wave.

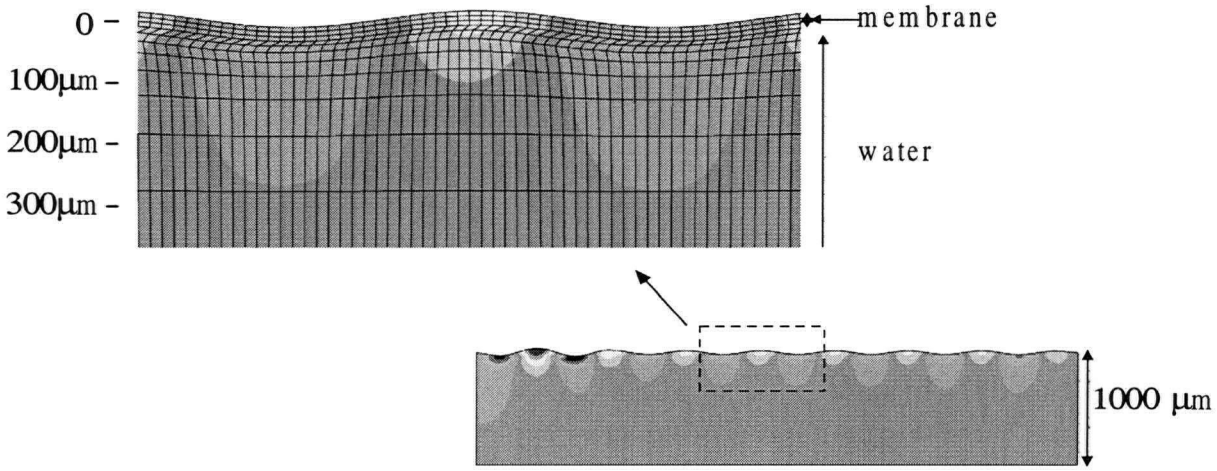

Figure 5-23: Deformed shape from FEM analysis of water supported membrane

To validate the use of the White/Wenzel model, the dispersion curve generated from the model was compared to a dispersion curve generated from the FEM analysis described in section 4.2.3. In both cases the membrane thickness was set at 25.4 μm with a Young's modulus of 3.5×10^6 N/m^2 and zero tension. Figure 5-24 shows these dispersion curves. It can be seen that the FEM model data consistently underestimates the curve predicted by the White/Wenzel model, but has exactly the same shape of curve. The slight systematic underestimation of the White/Wenzel curve indicates that this is probably due to the difficulty of reliably modeling the mechanical properties of water in the FEM model, and/or the finite mesh size needed to keep the computation time manageable.

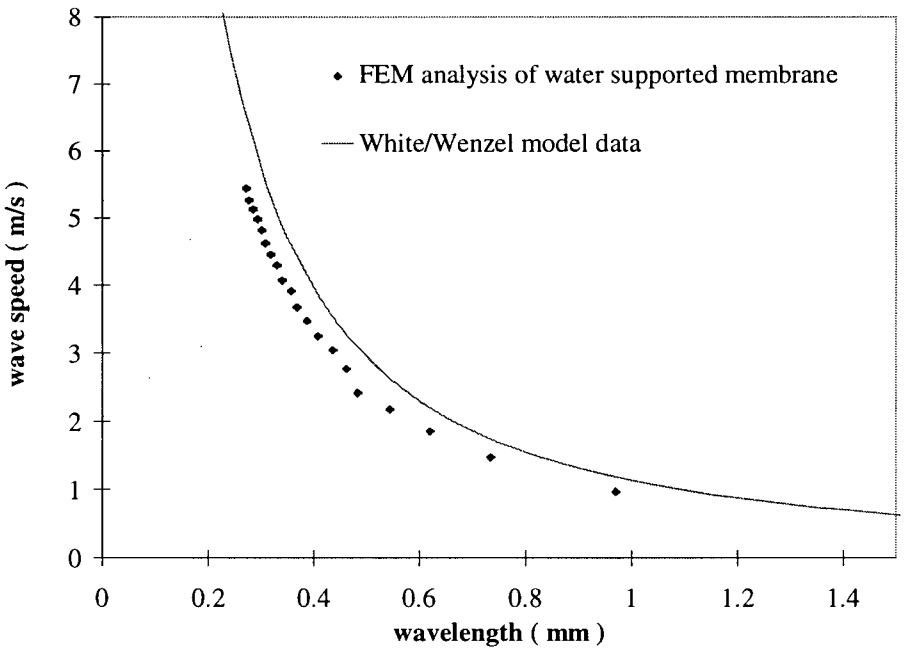

Figure 5-24: Comparison of FEM and White/Wenzel models for water supported membrane

5.2 Monochromatic Diffraction Patterns

5.2.1 Scalar Diffraction Model

The scalar diffraction model described in section 4.1 was used to gauge the effect of wave amplitude and rate of attenuation on the quality of the diffraction pattern. Additionally, the effect of the wavelength and the angle of incidence on the position of the $m=1$ and higher order diffraction peaks was readily studied.

The most important information to be determined is the amplitude required to see a substantial diffraction effect. As a first study, the values of incident light wavelength, surface wavelength, and incidence angle, were held constant at $\lambda_l = 632.8$ nm, $\lambda_s = 0.3$ mm and $\theta_i = 80°$, respectively, and the wave amplitude A_o was varied with zero damping. Figure 5-25 shows the diffraction patterns generated for amplitudes varying from 0.05 μm to 0.50 μm RMS. The ratio of the wave amplitude, A_o, to the incident light wavelength, λ_l, is given as a_o. As expected, at low amplitudes, the zero order peak is dominant. As the amplitude is raised, the higher order peaks rise in prominence. At an amplitude of $A_oRMS = 0.30$ μm, there is equal contribution from the zero order and the 1st order peaks. If the amplitude is raised above this, the amplitude of the zero-order peak actually decreases, while the higher order peaks emerge above the noise. This effect may be an artifact of the resolution of the model. However, this method gives a range of amplitudes for this particular wavelength and angle of incidence that will produce a strong diffraction pattern.

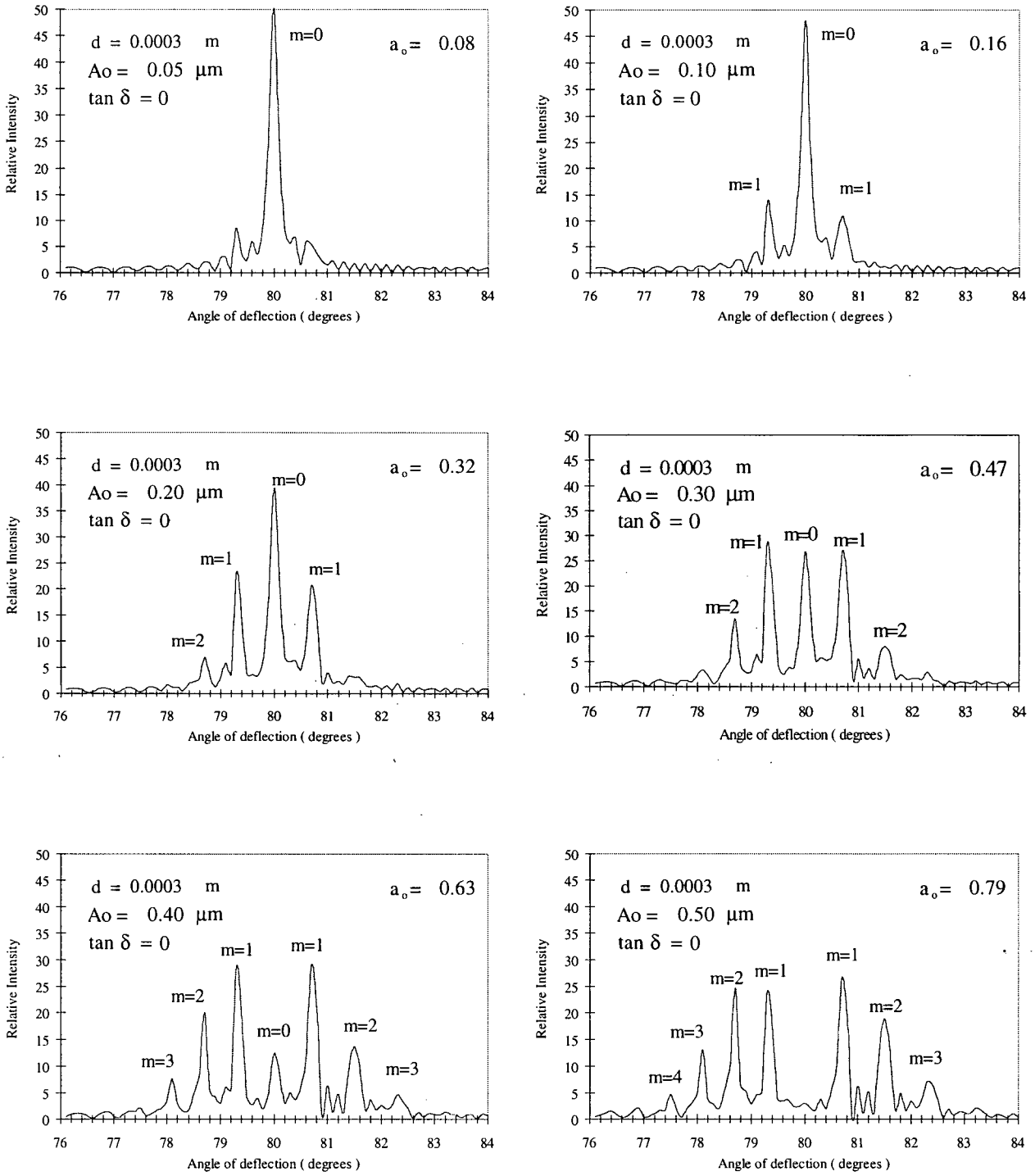

Figure 5-25: Scalar model scattering results for various values of surface wave amplitude, *Ao*

Figure 5-26 shows the diffraction patterns generated for a given angle of incidence and an increasing surface wave wavelength. The surface wavelength is varied through a typical range of 100 μm to 350 μm. The fraction of the d-spacing, d, to the incident light radiation, λ_l, is indicated on the graphs as δ. It is evident that at the smaller wavelengths, there is a substantial improvement in the angular separation of the diffraction peaks.

Figure 5-27 shows the effect that damping in the wave will have on the quality of the pattern. The damping is defined as described in section 2.3.2. It is varied between $tan\delta = 0$ to $tan\delta = 0.10$. At $tan\delta = 0$ the amplitude was chosen that gives approximately equal contribution from the $m = 0$ and $m = 1$ peaks. It can be seen that as the damping factor is raised, the $m = 1$ peaks decrease in prominence, but since our assemblies have damping factors substantially less than 0.1, this is not a problem.

Figure 5-28 shows the variation in the angle of incidence for a given wavelength. The angle of incidence is varied between 60° and 85°. It can be seen that as the angle of incidence is varied, the amplitude needed to produce a similar quality diffraction pattern changes. In each case an amplitude was chosen that gave an even contribution from the $m = 0$ and $m = 1$ peaks. At $\theta_i = 60°$, the amplitude required is 0.1 μm, this increases slowly until at near glancing angles are reached and then it increases sharply. At $\theta_i = 85°$, an amplitude of $A_o RMS = 0.49$ μm is required.

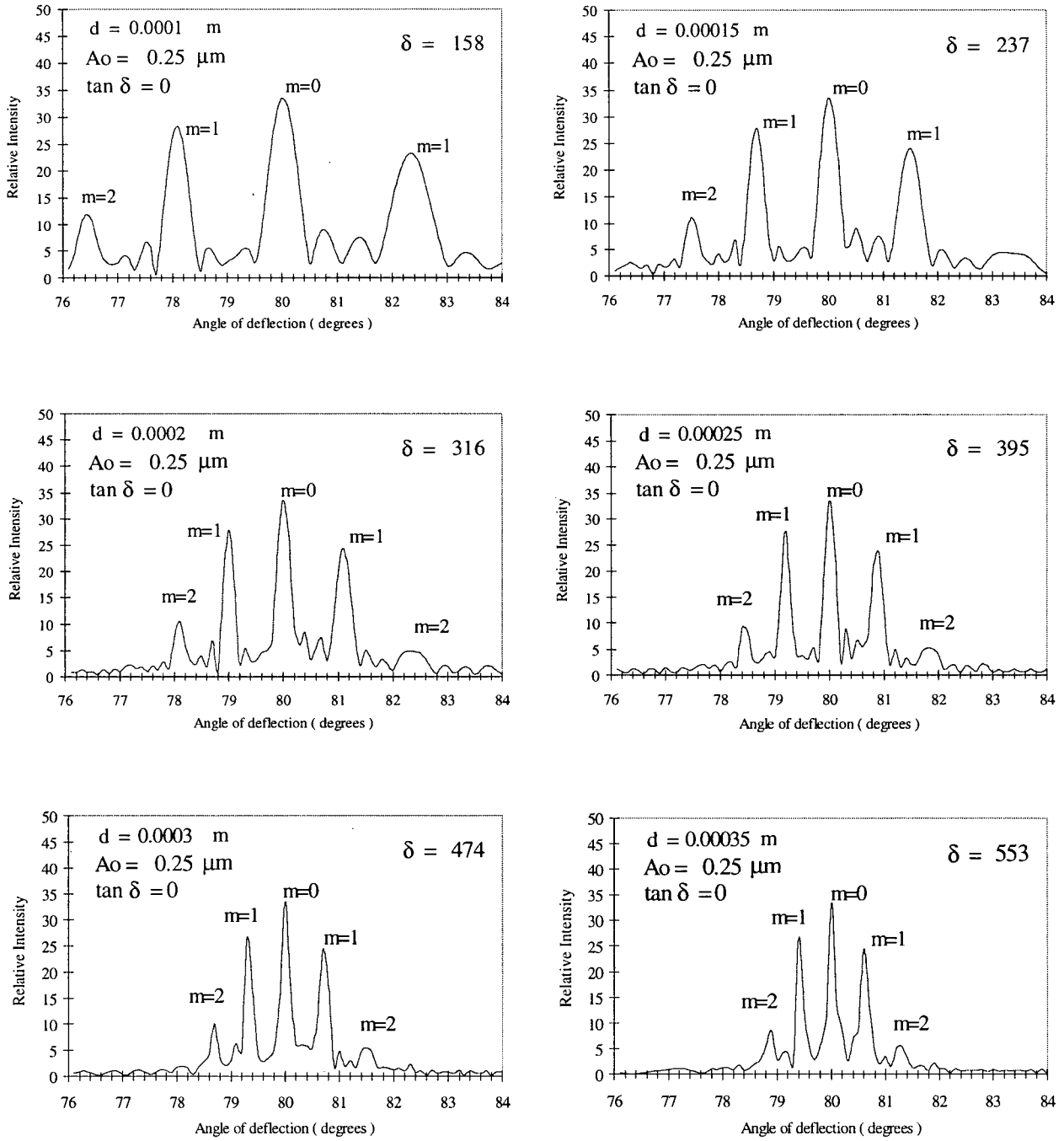

Figure 5-26: Scalar model scattering results for various values of surface wavelength, λ_l

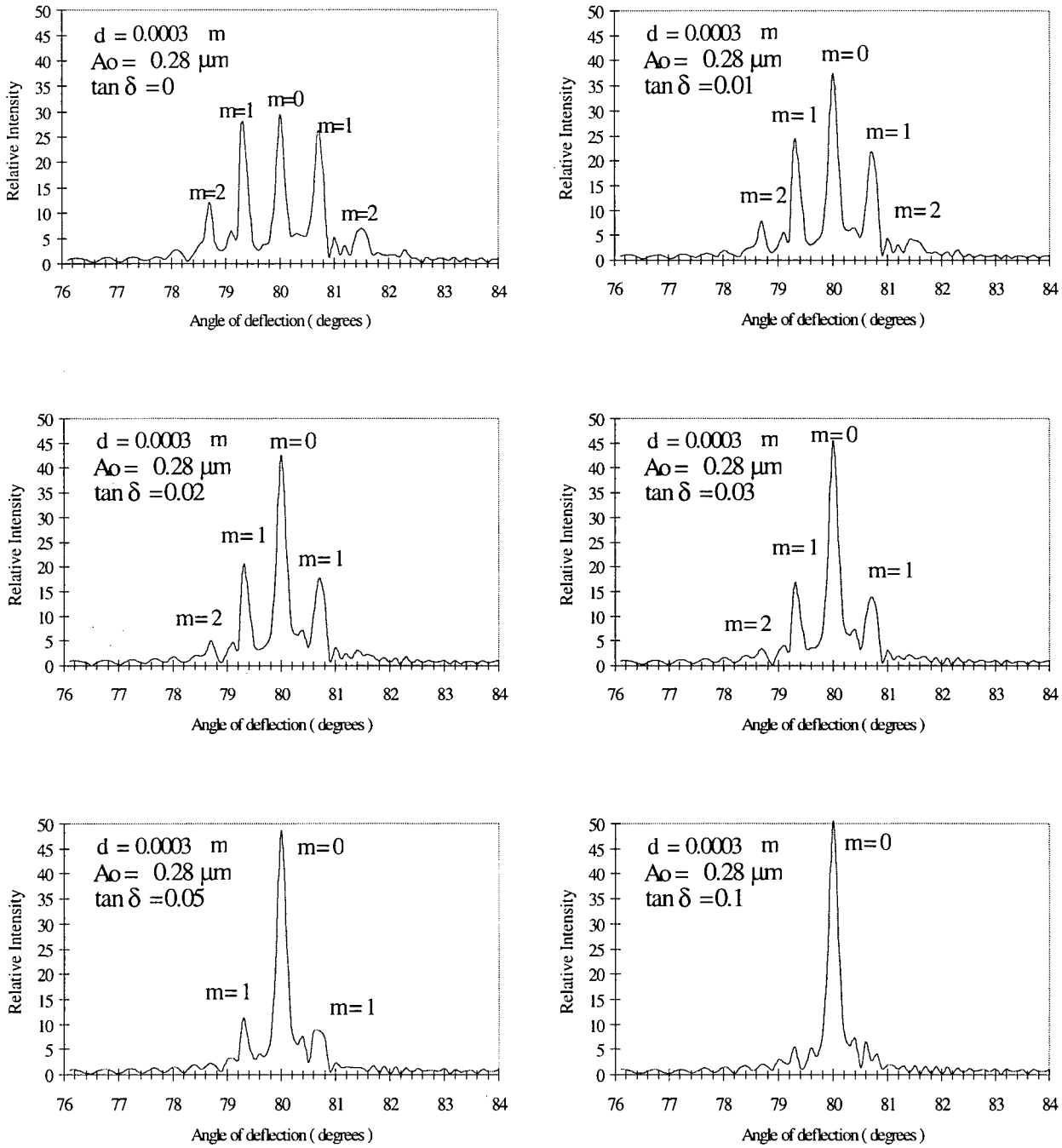

Figure 5-27: Scalar model scattering results for various values of wave damping, $tan\delta$

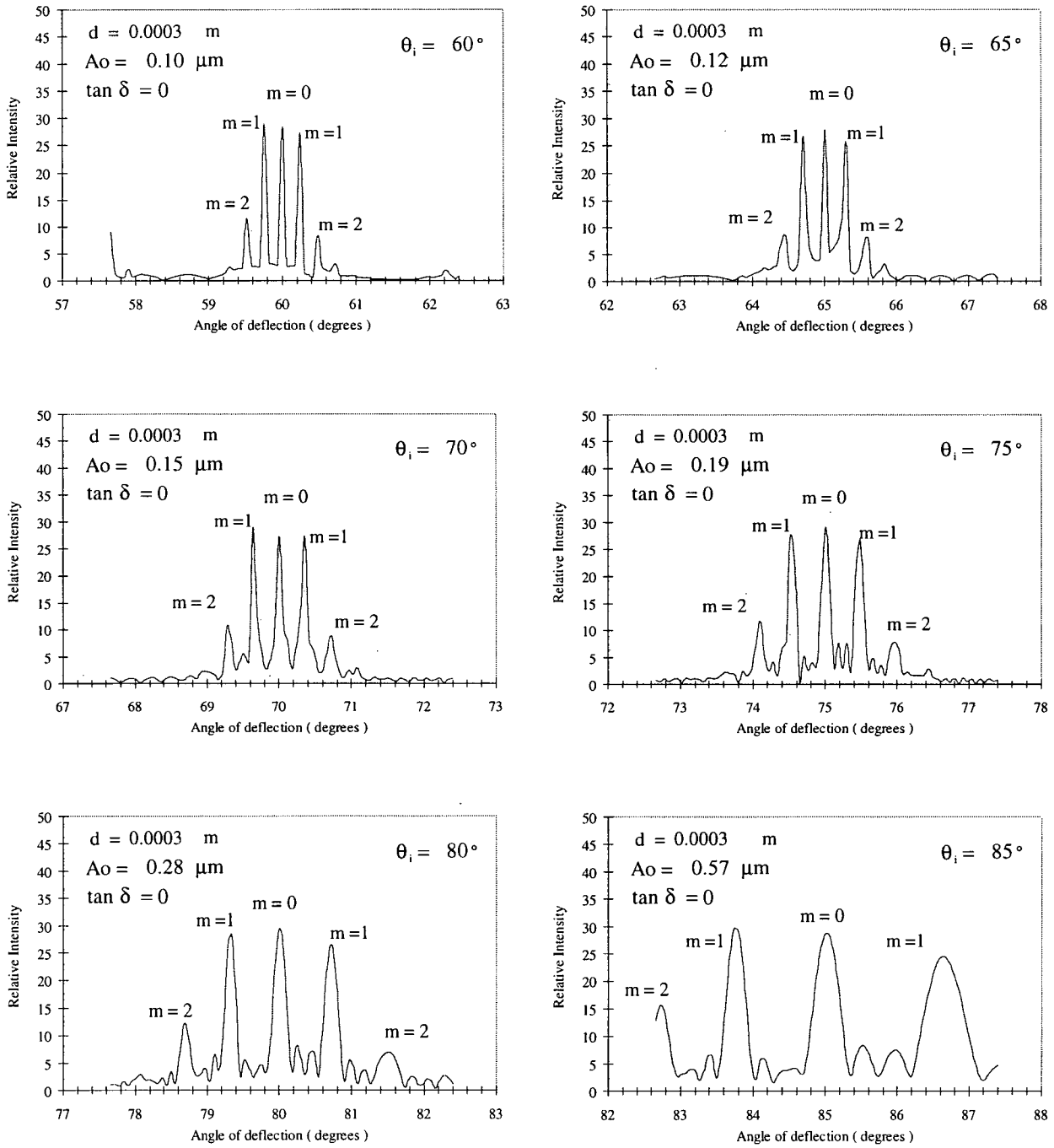

Figure 5-28: Scalar model scattering results for various values of angle of incidence, θ_i

The scalar diffraction model is useful in determining the how the experimental parameters will affect the quality of the resultant diffraction pattern. We describe the experimental procedure used to measure real diffraction patterns created by reflecting an obliquely incident laser beam from the device.

5.2.2 Experimental Results

A measurable diffraction pattern was first achieved from a transversely loaded thin slab sample of Silastic T sample 1/16" in width. The sample was obliquely illuminated along its side face by a HeNe laser beam at angle, $\theta_i = 83°$ from the normal to the side face of the slab. A telescope set at 20X angular magnification, ($m_\theta = 20$) was used to expand the size of the resulting diffraction pattern projected on a screen a distance, $L = 2.35$m, away from the sample. The geometry of the experiment is shown in Figure 5-29. From the diffraction pattern projected on the wall, the quantity measured was $2\Delta x_1$, the horizontal distance between the first order diffraction spots in the pattern. This value was used to determine the angular separation of these first order spots, $2\Delta\theta_1$, from the geometry of the experiment. The details of the geometry of this experimental set-up and the calculation of the angular deflection values, $\Delta\theta_n$, are given in Appendix C.

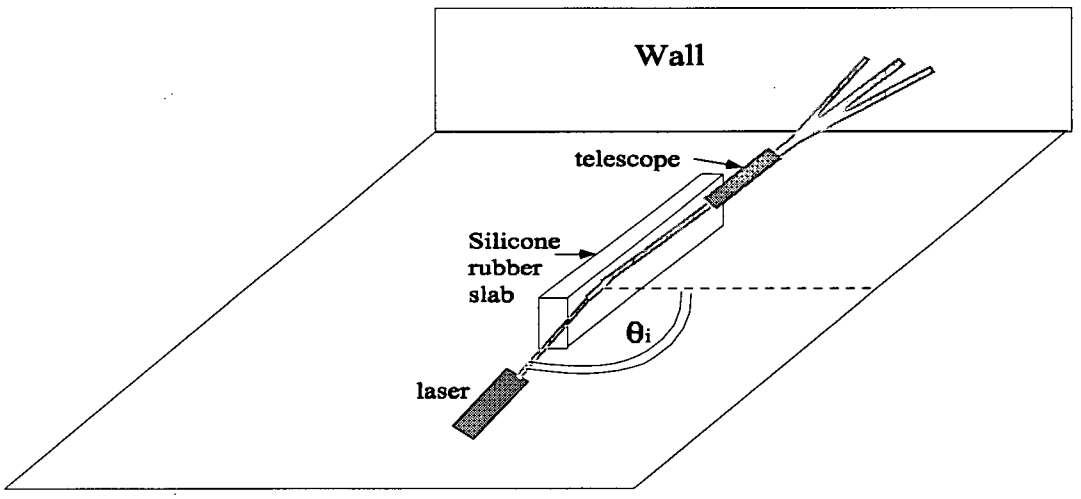

Figure 5-29: Geometry of diffraction patterns measured from thin slab

The wave speed and wavelength characteristics for this sample are listed in Table 5-2. This wavelength, along with the initial RMS wave amplitude and damping factor were used to produce the expected diffraction pattern from the scalar diffraction model. The expected angular separation of the first order diffraction spots can be determined from Equation (2-2) given the angle of incidence, $\theta_i = 83°$, and m=1.

Table 5-10 gives the comparison between the experimental and the modeled $2\Delta\theta_1$ values in tabular form and Figure 5-30 shows it in graphical form. In the case of the experimental data, the size of the error bar is determined by assuming that all measured lengths were accurate to the nearest 0.1 cm. For the model data, there is an error in the measured wavelength which was

determined statistically from experimentally measured data, and an error in the value of θ_i which is determined from two lengths, each with a 0.1 cm error. Since, this method involved measurement of distances and conversions to angles, there is a fair amount of measurement error introduced into the experiment. However, it can be seen from Figure 5-30 that there is good agreement between the modeled and experimentally derived values for most of the points. Since the experimentally determined value systematically underestimate the modeled values, this could be due to a slight systematic error associated with our assessment of the center of the diffraction spots.

Table 5-10: Comparison of modeled and experimental $2\Delta\theta_1$ values

frequency (Hz)	wavelength (m)	Modeled $2\Delta\theta_1$ (°)	Experimental $2\Delta\theta_1$ (°)
2100	0.00766 ± 0.00005	0.084 ± 0.002	0.0792 ± 0.002
2500	0.00716± 0.00003	0.090 ± 0.002	0.0854 ± 0.002
3000	0.00636± 0.00003	0.101 ± 0.002	0.0994 ± 0.002
3500	0.00575± 0.00002	0.112 ± 0.002	0.1066 ± 0.002
4000	0.00512± 0.00002	0.126 ± 0.002	0.1170 ± 0.002

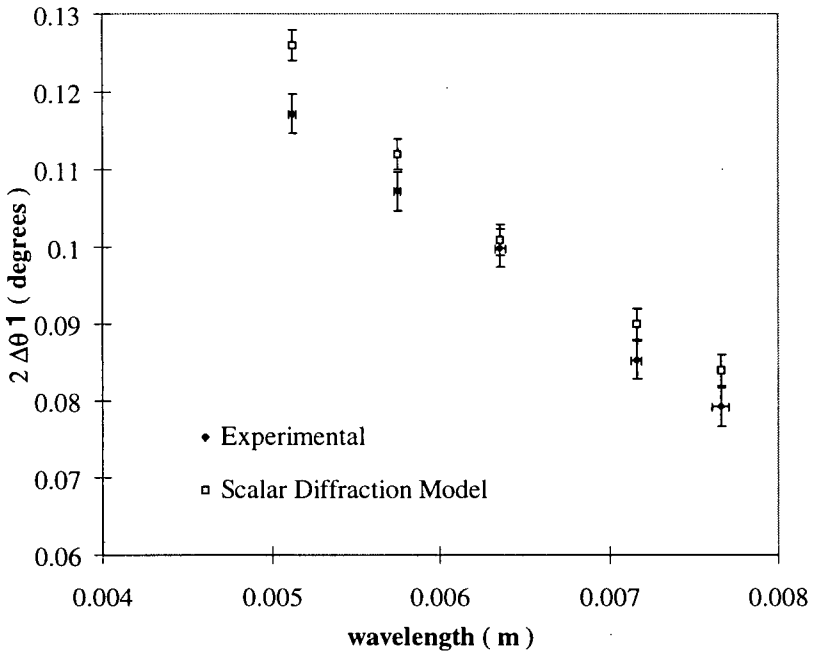

Figure 5-30: Comparison of $2\Delta\theta_1$ values from model and experiment

Diffraction patterns were also collected from a ~17μm water supported RTV615 membrane sample. The experiment was set-up as shown in Figure 5-31. The angle of incidence of the laser was chosen to be as close to glancing angle as possible, in order to maximize the deflection of the diffraction spots. However, as the angle of incidence increased, the laser came in contact with more of the surface of the membrane, and surface defects degraded the quality of the reflection. The optimum θ_i was a bit more than 80°. It was also found that if all the inherent tension in the membrane was removed, there was very poor quality to the zero order reflection. Without some minimum tension in the membrane, the surface was not sufficiently optically flat. As such, it was necessary to introduce a small amount of tension into the membrane.

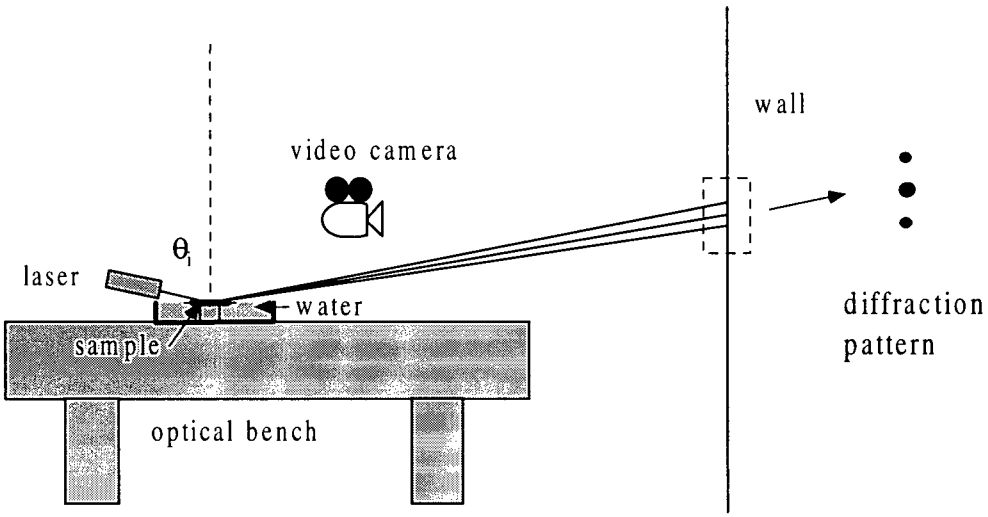

Figure 5-31: Set-up to measure diffraction patterns from water supported membranes

In order to calibrate the experiment, the geometry and distances had to be carefully measured to allow for a comparison with the scalar diffraction model. The angle of incidence of the laser was measured relative to the surface of the optical bench, by moving the sample (on an *xy* translation stage) out the beam of the laser and measuring the height of the emergence of the laser beam and distance to where the laser beam struck the table. This angle was measured to be $\theta_i = 82.26 \pm 0.08°$. The distance from the sample to the zero order spot on the wall was measured to be L=197.6 cm.

To consistently measure each diffraction pattern, they were recorded using a video camera and a frame grabber card and associated image processing software. The video camera was set up square-on to the wall where the diffraction patterns were projected as indicated in Figure 5-31.

Once the images were captured, they were converted to grey-scale intensity maps which listed pixel-by-pixel the relative intensity at each x,y position in the image. To plot out the diffraction pattern profile, we would simply choose the appropriate y value which would yield a cross-section through the middle of the diffraction pattern, and plot the intensity value versus x (in pixels). The next step was to convert the distance in pixels to an angular deflection in degrees. This can be done with a modification to Equation (C-3), in Appendix C, which includes the conversion from pixels to distance. Since this conversion depends on the zoom and the distance of the camera from the wall, it was calibrated for the camera configuration used for the duration of the experiment. The diffraction patterns were projected onto a ruled piece of graph paper with 1 cm by 1 cm squares. From an image of the paper, it was possible to determine that 1188 pixels = 21 cm, therefore, 1 pixel = 0.017676 cm. By substituting this value into Equation (B-3), we obtained the following conversion between distance in pixels and angular deflection in degrees: 1 pixel = 0.00512°. With this calibration, we could plot the intensity of the image versus angular deflection. To produce a plot that can be compared to the output of the scalar diffraction model, the zero-order peak had to be centered on the angle corresponding to the angle of incidence.

Diffraction patterns were captured for a range of frequencies from 1 kHz to 6.3 kHz. Above this frequency, the surface wave amplitude was not high enough to produce measurable first order diffraction spots. Some frequencies, which corresponded to system resonances, gave a higher response and more of the higher order diffraction spots were evident. At each of these frequencies, the wavelength was measured as described in section 5.1. The measured wavelength and the angle of incidence were then input into the scalar diffraction model in order to compare

the experimentally measured diffraction pattern with the model. Figure 5-32 shows the image of the reflected laser beam spot, measured with the device turned off, compared with the corresponding intensity map profile through the center of the spot. It can be seen that the reflected beam produced a clean, well defined first order diffraction spot. Figure 5-33 through Figure 5-41 show for each frequency, the frame-grabbed image of the diffraction pattern with the profile plots generated from the image and the scalar model. It was found that the scalar model plots corresponding to an angle of incidence of $\theta_i = 82.26°$ didn't produce a good agreement with the measured diffraction plot profiles. Although we were able to measure this angle of incidence accurately relative to the table, it was quite possible that the surface of the sample was not lying perfectly parallel to the surface of the table. The angle of incidence that produced an excellent agreement for all of the diffraction patterns shown below is $\theta_i = 84.5°$. Since the sample was not only floating on the top of the water, but was under stress from the wire actuator attached to its surface, a disparity of ~2° between the two surfaces is quite plausible, but difficult to measure.

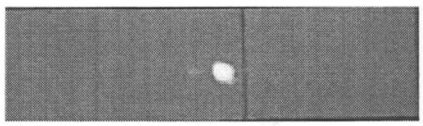

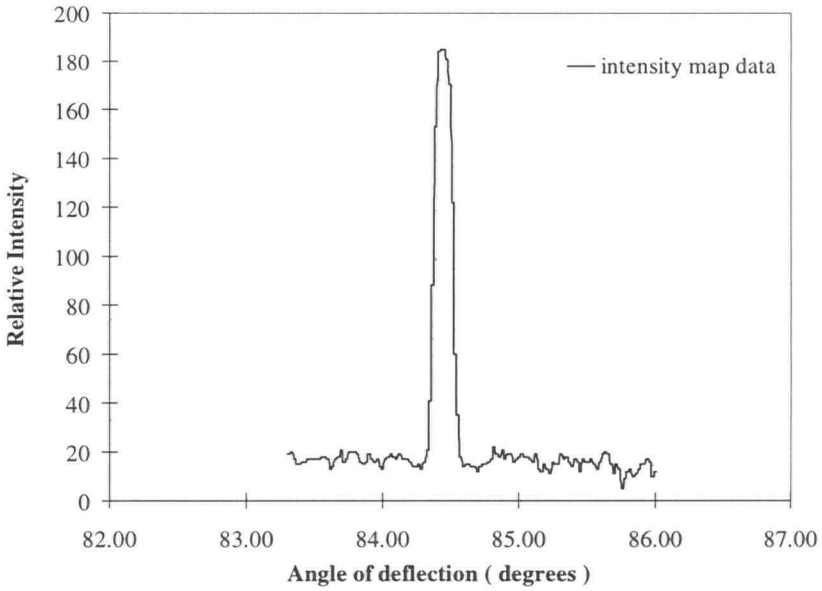

Figure 5-32: Reflection of laser from unexcited surface of water supported membrane

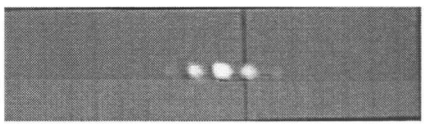

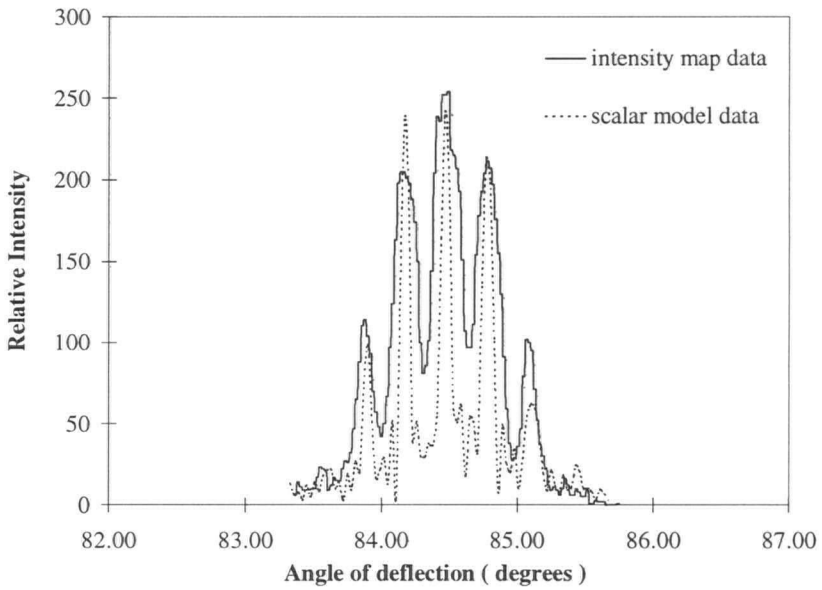

Figure 5-33: Diffraction patterns measured at 1 kHz and compared with scalar model

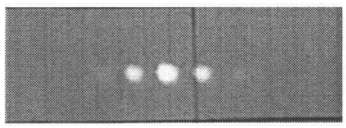

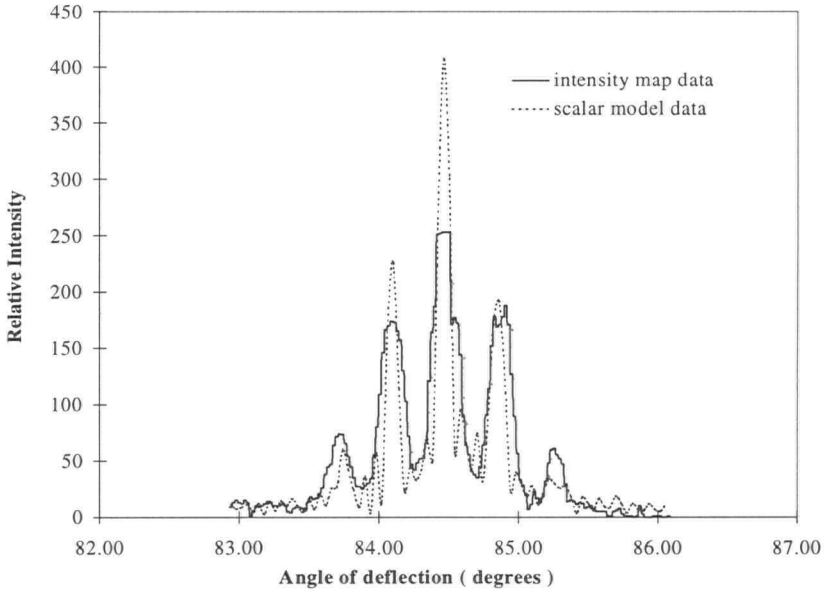

Figure 5-34: Diffraction pattern measured at 1.5 k Hz and compared to scalar model

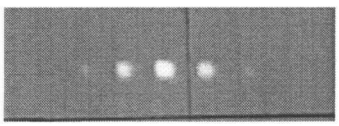

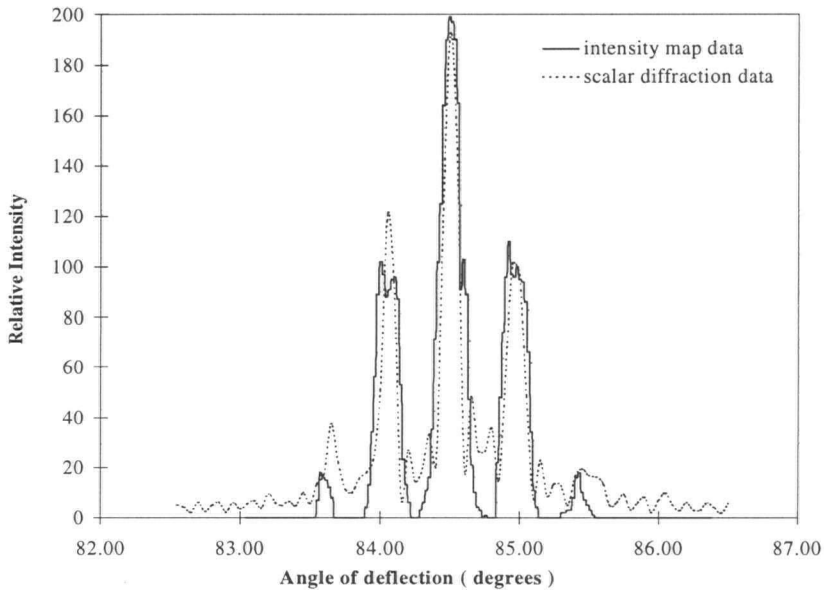

Figure 5-35: Diffraction pattern measured at 2kHz and compared to scalar model

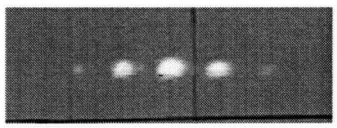

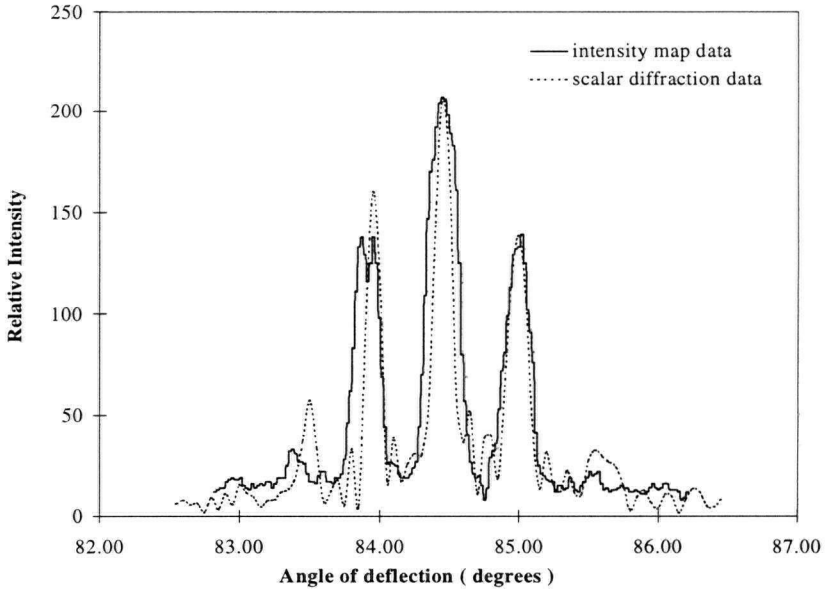

Figure 5-36: Diffraction pattern measured at 2.5 kHz and compared to scalar model

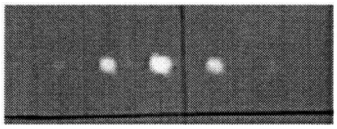

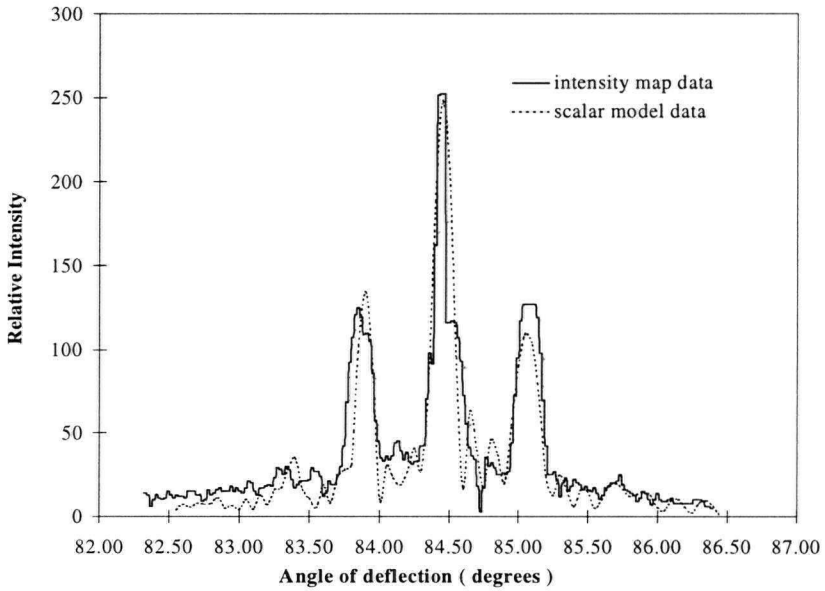

Figure 5-37: Diffraction Pattern measured at 3 kHz and compared to scalar model

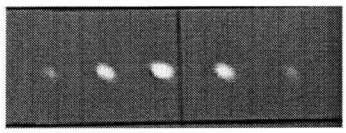

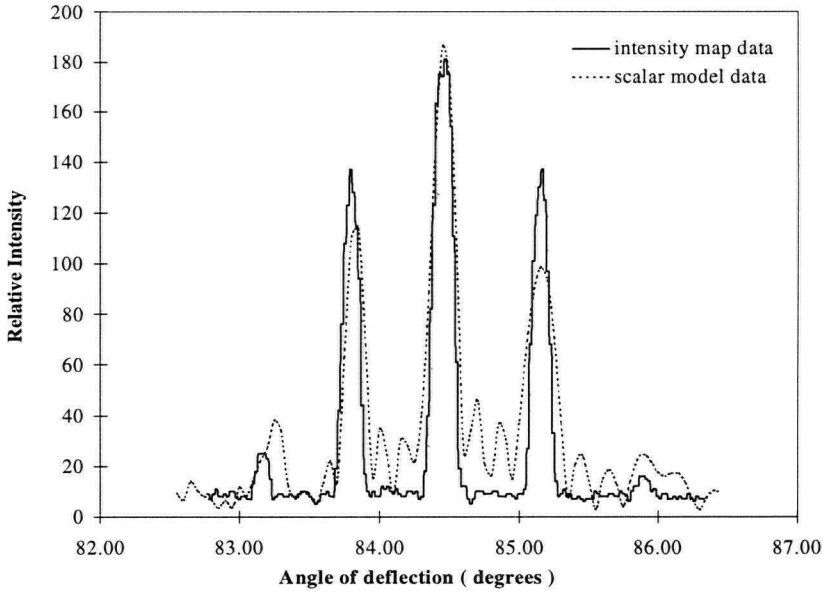

Figure 5-38: Diffraction pattern measured at 3.6 kHz and compared to scalar model

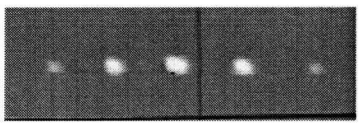

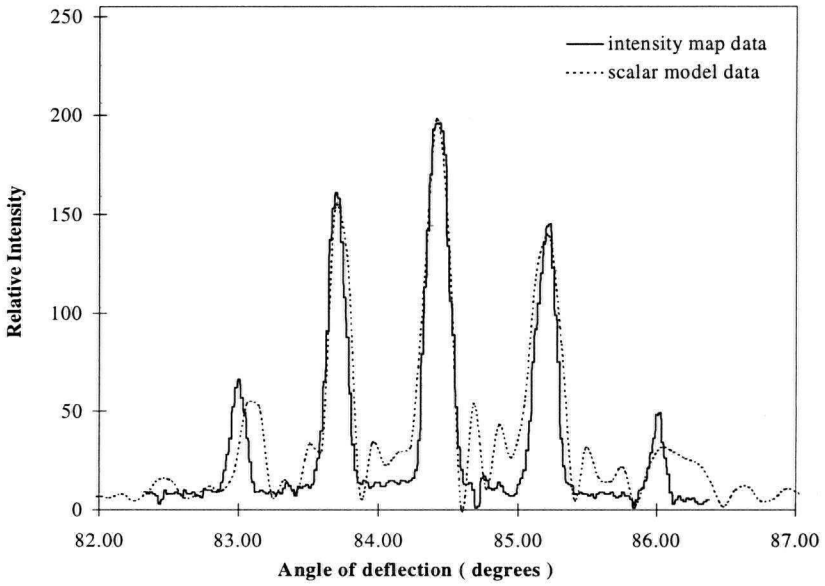

Figure 5-39: Diffraction pattern measured at 4.3 kHz and compared to scalar model

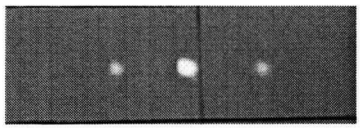

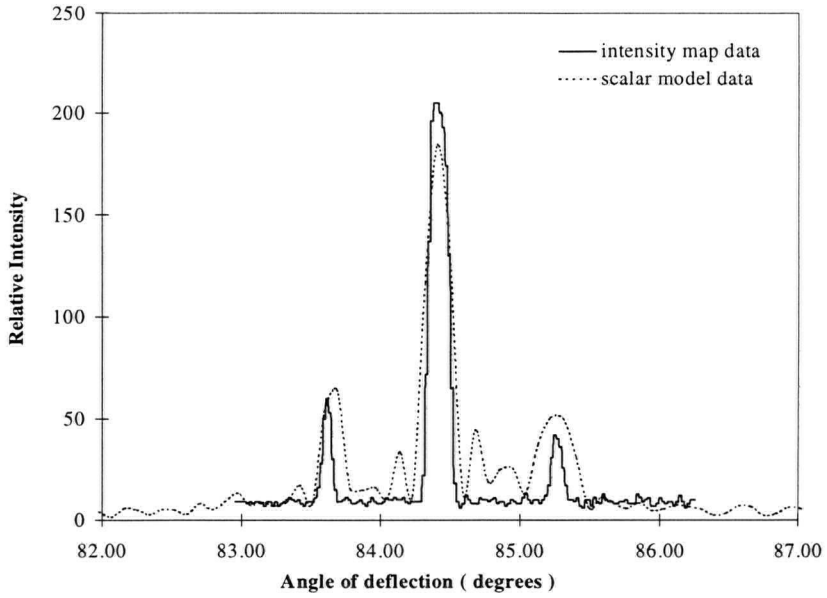

Figure 5-40: Diffraction patterns measured at 5.0 kHz and compared to scalar model

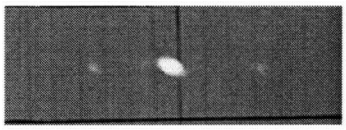

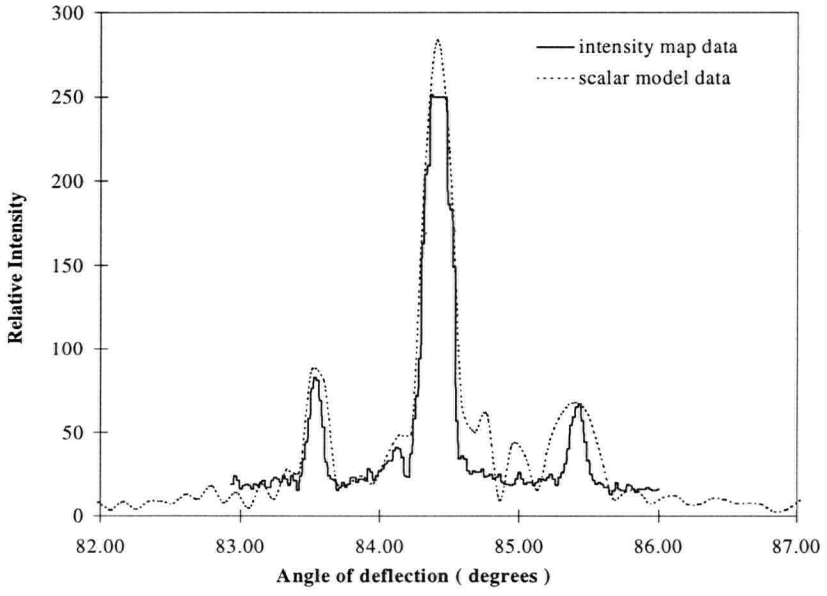

Figure 5-41: Diffraction pattern measured at 6.3 kHz and compared to scalar model

These results are important for the following reasons. We were able to demonstrate that the plate waves in the water supported membranes could be used as a diffraction grating. We showed that by increasing the driving frequency of the line driver launching the waves, we could decrease the wavelength of the surface wave and increase the angular deflection of each of the orders of diffraction. Furthermore, we were able to accurately measure the wave characteristics of the propagating surface waves and input these details into the scalar diffraction model to see the expected diffraction pattern from the measured surface deformation. We also demonstrated a way of measuring the experimental diffraction patterns with a frame-grabber and processing the images so that they could be compared to the output from the scalar diffraction model. These experimental procedures can be used in the future to test the performance of the next generation of devices.

6. DISCUSSION

We have demonstrated, as far as we know, the first ever achievement of a variable spacing diffraction grating using elastomeric surface waves. Four different kinds of surface waves in silicone rubber were characterized. Two of these experiments produced surface waves with a small enough wavelength and high enough wave amplitude that a measurable diffraction effect was realized. The advantages and limitations of this technology will now be discussed.

The unique properties of silicone rubber enable it to be used successfully in this application. First and foremost, the extremely low Young's modulus of ~ 10^6 N/m^2 yields a low acoustic wave speed and low wave energy density which enable the waves to be easily actuated. It is relatively cheap (~20-50$ per lb.), compared to pure crystal materials, and it moulds easily and accurately into a variety of shapes and membrane thicknesses. Furthermore, silicone rubber maintains its elastomeric properties over a wide temperature range, is chemically inert and long lasting.

Surface waves were launched into three different structures before the final design idea was formulated. Firstly a Rayleigh wave was propagated into a bulk piece of silicone, yielding a wave speed of 27 m/s. Then an attempt was made to confine the wave mode in thin slab silicone structures. A Rayleigh wave confined to the top surface of one of these slabs yielded a wave speed of ~30 m/s, but had very high damping due to loss of energy to other wave modes along the side face of the slab. A transverse wave along the top edge of the slab provided a promising option with a wave speed of ~ 20 m/s and low damping. However, a finite element analysis of

this structure indicated that this was simply a plate mode of the slab propagating within the slab and that the wave was not confined to the top surface.

The most promising candidate to be used as a variable spacing diffraction grating device was the use of plate waves in water supported membranes. The wave speed of this mode is dependent on three main things: rubber modulus, membrane thickness and membrane tension. Through considerable trial and error, we developed a procedure to make these thin silicone rubber membranes. Membranes as thin as 6 microns were made, which yielded wave speeds from 1 - 6 m/s. This was a dramatic improvement over the previous attempts to create surface waves. With the ability to reduce the tension in the membranes, the lowest possible wave speeds for a given membrane thickness were achieved.

We showed it was possible to completely describe this wave mode, using the White/Wenzel model to predict, for a given rubber density, modulus, membrane tension and thickness, a dispersion curve for a range of wavelengths. These dispersion curves are flatter at the bigger wavelengths, but curve upwards dramatically at the lower wavelengths. Typically, wavelengths from 200-1000 μm were easily achieved with the current means of actuation.

A scalar diffraction model was constructed which predicted, for a surface deformation determined experimentally, what kind of diffraction pattern could be expected. It demonstrated that the angular separation of the orders of diffraction was inversely proportional to the wavelength of the surface wave, and that the constant of proportionality increases with the angle of incidence of the

laser beam. Furthermore, the relative intensity of the higher orders of the diffraction pattern depended on the wave amplitude and the attenuation of the wave. This gave us an indication what wave amplitudes were necessary in order to see an observable diffraction effect at the various angles of incidence. We also learned that the damping factors measured in the water supported plate waves (~1-3%) were small enough not to degrade the quality of the diffraction pattern.

Diffraction patterns were carefully measured from a water loaded ~16 μm membrane of RTV615 rubber using a video camera and frame grabber. Unfortunately, in order to achieve a sufficient optical quality surface to bounce the laser beam off, a small amount of tension had to introduced into the membrane which increased the available wavelengths produced by the device. The angular deflection values of the diffraction spots were calculated and compared with the scalar diffraction model. Diffraction patterns were measured for a range of frequencies from 1 kHz to 6.3 kHz. At 1 kHz the first order spots were deflected ~0.3° away from the zero-order spot. Above the maximum frequency of 6.3 kHz no diffraction effect was observed. At this frequency, the first order diffraction spots were deflected ~1° from the zero-order spot. The measured diffraction patterns compared favourably with scalar model diffraction patterns, with the exception that the measured angle of incidence of the laser beam had to be adjusted to account for the fact that the surface of the sample was not exactly parallel to the surface of the optical bench.

The ability of this device to produce large angular deflections was limited by the response of the system at higher frequencies. This is mainly due using a wire responding to a Lorentz force as a

means of actuation. The displacement of this wire drops off as a function of frequency, meaning it is difficult to actuate the surface at the higher frequencies. The dynamic properties of the silicone indicate that the elastic properties should remain intact up to the glass-transition frequency. At the operation frequencies used in this experiment, we should be well below this limit. It remains, then, to find another means of actuation that can provide a constant displacement up to a higher frequency. A second limitation was the inability to easily produce thin membranes of silicone rubber below about ~6 μm. Perhaps some methods involving spin coating, or solvents could be investigated in order to produce uniform thin membranes of silicone.

There are several obvious next steps which the time constraints of this project did not permit. Attempting to propagate a non-sinusoidal wave pattern that could created a surface deformation that might approximate a blazed grating. This would have the advantage that all of the transmitted light energy could be concentrated into one order. This case would be favourable in order to efficiently steer the beam.

The fact that we have a very well behaved propagating surface wave indicates that there are some very different applications from a diffraction grating. At these low thicknesess, the novel surface energy characteristics could affect the wave speed and produce some interesting effects. For example, this system could be used as a sensor for surface tension changes, perhaps in response to surface adsorption from bio-materials.

In conclusion, we have demonstrated that it is possible to use elastomeric surface waves as a means of producing a variable spacing diffraction grating. While far from producing an effect that can be exploited commercially, it demonstrates the feasibility and proof of concept and suggests several new directions for further work.

GLOSSARY OF SYMBOLS

β	angular deflection of first order beam
$\mathcal{E}$	wave energy density per unit area
d	d-spacing of diffraction grating
θ_m	angular deflection of m^{th} order diffraction peak
m	order of diffraction peak
λ_l	wavelength of light radiation incident on grating
λ_s	wavelength of surface wave
θ_i	angle of incidence of radiation from normal to diffraction grating
ω_o	angular frequency of incident light radiation
ω_a	angular frequency of acoustic wave
ν	Poisson's ratio
ν_{rubber}	Poisson's ratio of rubber
Y	Shear modulus
E	Young's modulus
K	Bulk modulus
T	temperature
T_g	glass transition temperature
υ_{Tg}	frequency at which glass transition temperature was measured
υ_g	glass transition frequency

υ_T	glass transition frequency measured at temperature, T
ρ	density
α	linear coefficient of thermal expansion
t	thickness of plate or membrane
$\underline{\xi}$	polarization vector
$\underline{\boldsymbol{k}}$	wave vector
c	wave speed
c_R	Rayleigh wave speed
c_s	symmetric plate wave speed
c_a	asymmetric plate wave speed
A	wave amplitude
A_o	initial wave amplitude
f	driving frequency
$tan\delta$	loss tangent
κ_o	natural wave number
κ_l	loss wave number
α	attenuation coefficient
α_a	absorption attenuation coefficient
α_s	scattering attenuation coefficient
D	characteristic diameter of scattering centers on surface of rubber
$\underline{\boldsymbol{B}}$	magnetic field vector
i	index of scattering points in scalar diffraction model

θ_d	angle at which phase differences are calculated for rays scattering in scalar model
φ_i	phase calculated for ray scattering from point i and deflecting to angle θ_d
$I(\theta_d)$	relative intensity of light at scattering angle θ_d
η	viscosity of a liquid
σ	force in the propagation direction per unit width perpendicular to this direction
δ_E	decay length of evanescent wave from plate wave in the liquid
c_o	speed of sound in fluid
B	effective bending stiffness of plate under tension
M	mass per unit are of plate
$\Delta\varphi$	phase difference between driving frequency and wave at distance x from source
L	distance in experimental set-up from sample to wall along the path of the zero order spot
P	pressure on one side of membrane
h	height of inflated membrane above equilibrium
K	kinetic energy
m_θ	angular power of telescope
$\Delta\theta_n$	angular distance between n^{th} order diffraction spots on either side of zero order
Δx_n	spacial distance on projection screen between n^{th} order spots on either side of zero order
R	radius of cylindrical support for water support membranes
r	radius of curvature of inflated membrane

GLOSSARY OF TERMS

blazed grating: A diffraction grating with a repeated array of angled surfaces which concentrates the transmitted beam into one diffraction order.

bulk modulus: The modulus of elasticity which describes the resistance to bulk compression.

bulk wave: An acoustic wave traveling through the bulk of the material.

diffraction grating: A regularly spaced array of apertures or obstacles which affects the phase or amplitude of a light beam with the effect of having transmitted beams traveling only in distinct directions.

d-spacing: The distance between the apertures or obstacles in the diffraction grating.

FEM: Finite Element Modeling: A commercial software package that models the effect of loading an object by meshing the object into elements and solving the equations of motion for each element.

glass transition frequency: The frequency at which a polymer undergoing a cyclic deformation enters the glassy regime, with a high modulus of elasticity.

glass transition temperature: The temperature at which a polymer becomes glassy, with a high modulus of elasticity.

manometer: A device to measure the difference in pressure between the atmosphere and a vessel to which it is attached.

modulus of elasticity: The constant of proportionality between an applied stress and the resultant strain.

piezoelectric stack: A rectangular piece of a piezoelectric material which will cyclically change its length under an applied AC current, the magnitude of the length change being proportional to the applied voltage.

plate wave: An acoustic wave traveling in a thin plate whose thickness is much smaller than the wavelength of the wave.

Poisson's ratio: A factor indicating the compressibility of a material, with a value of 0.5 meaning a virtually incompressible substance.

scalar diffraction model: A model devised for this thesis which can predict the expected diffraction pattern from a given surface deformation by calculating the phase differences from rays scattered from the surface.

shear modulus: The modulus of elasticity which describes a materials resistance to shearing.

Shore A hardness: A number which describes the resistance of a rubber material to the action of having a ball pressed into its surface.

silicone rubber: An elastomeric material made of long polymer networks with a siloxane backbone with pendant methyl groups.

surface wave: A wave which travels along the free surface of a material with most of its wave energy being confined to within a wavelength's distance of the surface.

White/Wenzel model: An analytical model used in this thesis to calculate the wave speed of a fluid loaded plate wave for a given wavelength, fluid, plate thickness, modulus and plate tension.

WLF equation: Williams Landel, Ferry Equation: An equation to show the relationship between the glass transition temperature and the glass transition frequency.

Young's modulus: The modulus of elasticity which describes the resistance of a material to axial tension or compression.

REFERENCES

[1] Pinnow, D.A., Guidelines for the selection of Acoustooptic Materials, IEEE Journal of Quantum Electronics, Vol.QE-6, No. 4, April 1970.

[2] Hecht, E. and Zajec, Z., Optics, Addison Wesley Publishing Company, 1974.

[3] R. M. White, Surface Elastic Waves, Proceedings of the IEEE. Vol. 58, No. 8, 1970.

[4] ASTM D1566-90.

[5] Tabor, D., The bulk modulus of rubber, POLYMER, **35**, (13), p.2759-2763.

[6] Lindley, P.B., J.Strain Anal.,**2** (3), p.142, 1968.

[7] ibid 5.

[8] Harper, Charles, A., editor in chief, Handbook of Plastics, Elastomers and Composites, 3rd. ed., McGraw-Hill, 1996.

[9] Payne, A.R., and Freakley, P.K., Theory and Practice of Engineering with Rubber, Applied Science Publishers Ltd., London.

[10] Owen, M.J., The Surface Activity of Silicones: A Short Review, Ind. Eng. Chem. Prod. Res. Dev., **19**, p. 97-103, 1980.

[11] Kim, S., Cherney E.A., Hackam, R., Hydrophobic Behaviour of Insulators Coated with RTV Silicone Rubber, Proceedings of the 3rd International Conference on Properties and Applications of Dielectric Materials, July 8-12, 1991, Tokyo, Japan.

[12] Willliams, M. L., Landel R.F., and Ferry, J.D., J. Amer. Chem. Soc.,**77**, p. 3701, 1955.

[13] Ferry, J.D., and Fitzgerald, E.R. J. Colloid. Sci., **8**, p. 224., 1953.

[14] Handbook of Sonar Transducer Passive Materials, R.N. Capps, F.J.Weber, C.M.Thompson, Naval Research Laboratory, Memorandum Report 4311, October 30, 1981.

[15] Bosc, D., and Maugen, P., 'Acoustic Properties of Transparent Polysiloxanes', Journal of Applied Polymer Science, Vol. 40, p. 135-142, 1990.

[16] Szilard, J., Ulrasonic Testing, John Wiley and Sons, 1982.

17 Viktorov, I.A., Rayleigh and Lamb Waves, Plenum Press, 1967.

[18] Szilard, J., ed., Ultrasonic Testing, John Wiley & Sons, 1982.

[19] B.J Costello, B.A. Martin, and R.M. White, Ultrasonic Plate Waves for Biochemical Measurements, Ultrasonics Symposium, p. 977-981, 1989.

[20] R.M.White and S.W.Wenzel, Fluid Loading of a Lamb -wave sensor, Applied Physics Letters, **52** (20), p. 1653-1655, 1988.

[21] ibid 20.

[22] ibid 19.

Appendix A: Calculation of Energy Density in Surface Wave

To estimate the energy density per unit area, $\mathcal{E}$, of a surface wave, we consider the configuration shown in Figure A-1, where a surface wave with wavelength, λ, and amplitude, A, is propagating in a medium with Young's ,modulus, E.

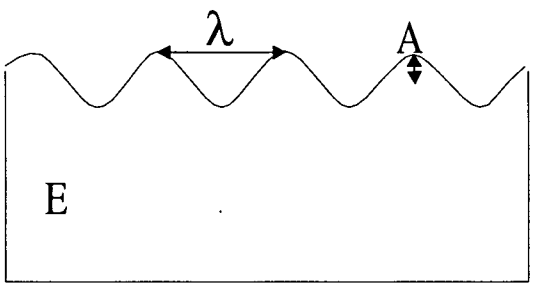

Figure A - 1: Surface wave with wavelength, λ and amplitude, A, propagating in medium with modulus, E.

The maximum kinetic energy is given by Equation (A-1). We assume that all the wave energy is confined to within a wavelength's distance from the top surface, therefore, the maximum kinetic energy per unit area is approximately given by Equation (A -2).

$$K_{\max} = \frac{1}{2}mv^2 \qquad \text{(A-1)}$$

$$\frac{K_{\max}}{area} \cong \frac{1}{2}(\rho\lambda)\mathrm{v}^2 \qquad \text{(A-2)}$$

To calculate the speed we consider a small element near the surface of the medium. It has an approximate angular velocity given by Equation (A-3). The frequency of the wave can be written as Equation (A-4).

$$v \cong \omega A \qquad \text{(A-3)}$$

$$\omega = \frac{2\pi c}{\lambda} \qquad \text{(A-4)}$$

The wave speed of the Rayleigh surface wave is given in Equation (A-5). Therefore we can rewrite the ω^2 term as given by Equation (A-6).

$$c \cong \sqrt{\frac{E}{\rho}} \qquad \text{(A-5)}$$

$$\omega^2 \cong \frac{4\pi^2}{\lambda^2}\frac{E}{\rho} \qquad \text{(A-6)}$$

The energy density can now be written as given in Equation (A-7). Which can be reduced to Equation (A-8), the expression which shows that the parameters affection the energy density per unit area are the amplitude, modulus and wavelength.

$$\mathcal{E} \cong \frac{1}{2}\lambda\rho\frac{4\pi^2}{\lambda^2}\frac{E}{\rho}A^2 \qquad \text{(A-7)}$$

$$\mathcal{E} \propto \frac{A^2 E}{\lambda} \qquad \text{(A-8)}$$

Appendix B: Scalar Diffraction Model Calculations

In the array of points of the scalar diffraction model, it is necessary to calculate the accumulated phase for incoming light scattering from a point at ($x, f(x)$) in the array. This phase for each point is measured *from* an arbitrary line constructed perpendicular to the incoming light ray, at an angle θ_i, and measured *to* another arbitrary line drawn perpendicular to the outgoing, scattered light ray at an angle θ_d. Figure B - 1 shows this geometry. The phase from line 1 to the scatter point is called ϕ_1 and ϕ_2 is the phase from the scatter point to line 2.

Figure B - 2 shows how ϕ_1 was calculated from the geometry of the model. We consider the case that the scattering point at index, i, is given a displacement in the y-direction of y_i. All other

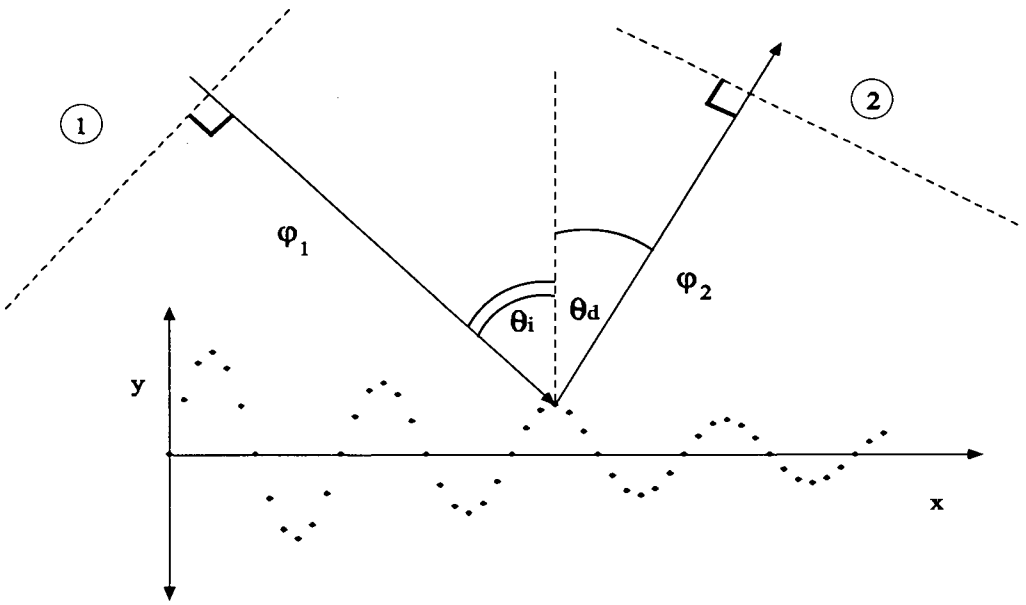

Figure B - 1: Basic Geometry of Scalar Diffraction Model

scattering points are shown with zero y displacement. A light ray incoming at θ_i to the normal scatters from a point of index, i, x-position, $i*dx$, and a y-position of y_i. Notice that line 1 is drawn from $x = 0$ and $y = 0$ and is perpendicular to the incoming light ray. In the diagram we are interested in the distance ED, from this we can calculate ϕ_1. From the geometry it can be seen that the following relationships are true:

$$ED = AC = AB - CB \tag{B-1}$$

$$FB = i * dx \tag{B-2}$$

$$DB = y_i \tag{B-3}$$

Looking at triangles FAB and CDB we can now determine the lengths AB and CB in the following way:

$$Sin(\theta_i) = \frac{AB}{FB} = \frac{AB}{i * dx}$$
$$\therefore AB = i * dx * Sin(\theta_i) \tag{B-4}$$

$$Cos(\theta_i) = \frac{CB}{DB} = \frac{CB}{y_i}$$
$$\therefore CB = y_i * Cos(\theta_i) \tag{B-5}$$

$$\therefore ED = AC = i * dx * Sin(\theta_i) - y_i * Cos(\theta_i) \qquad \text{(B-6)}$$

$$\phi_1 = ED * \frac{2\pi}{\lambda_l} = \left\{ i * dx * Sin(\theta_i) - y_i * Cos(\theta_i) \right\} \frac{2\pi}{\lambda_l} \qquad \text{(B-7)}$$

Similarly, it can be shown that:

$$\phi_2 = \left\{ Sin(\theta_d) * (50 - i) * dx - Cos(\theta_d) * y_i \right\} \frac{2\pi}{\lambda_l} \qquad \text{(B-8)}$$

The net accumulated phase, ϕ_i, for each point at index, *i*, is then given as follows:

$$\phi_i = \phi_1 + \phi_2 \qquad \text{(B-9)}$$

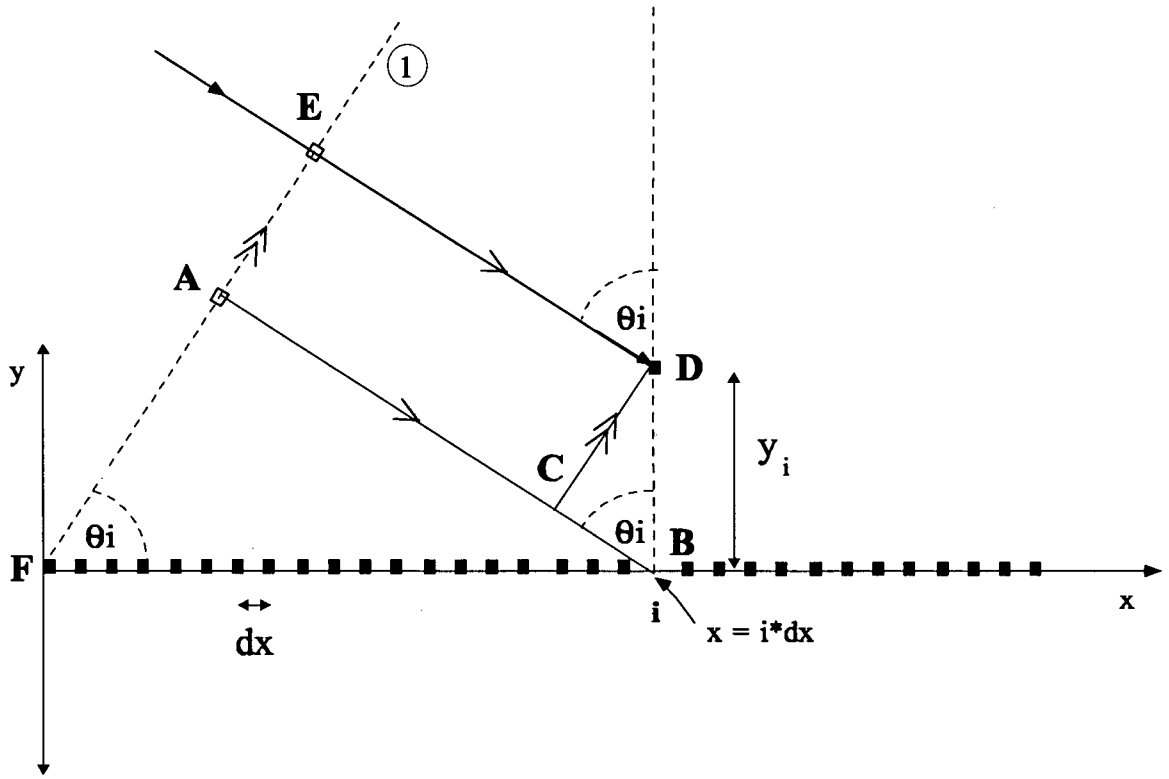

Figure B - 2: Geometry need to calculate ϕ_1 in Scalar Diffraction Model

Appendix C: Geometry for the Calculation of Angular Deflection Values

In order to calculate the angular deflection of each of the higher order diffraction spots, it was necessary to measure the angle of incidence and the distance, *L*, from the sample, along the path of the zero-order spot, to the wall. A telescope with angular power mθ can be used to expand the angular deflection of the diffraction pattern. From the geometry in Figure C-1, the distance, Δx_n, of the n^{th} order from the zero order spot can be converted into an angular deflection value, $\Delta\theta_n$ in degrees according to Equations (C-1) to (C-3).

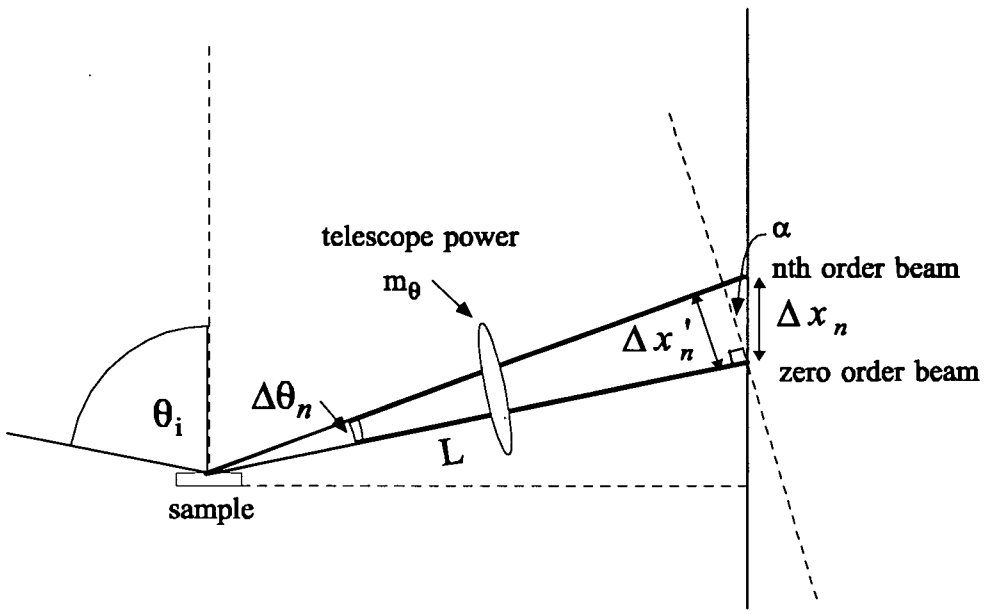

Figure C-1: Geometry of experimental set-up to measure angular deflection values

$$\tan(m_\theta * \Delta\theta_n) = \frac{\Delta x_n'}{L} \qquad (C\text{-}1)$$

$$\Delta x_n' = \cos\alpha * \Delta x_n \qquad (C\text{-}2)$$

$$\because \alpha = \frac{\pi}{2} - \theta_i \qquad (C\text{-}3)$$

$$\cos\alpha = \sin\theta_i \qquad (C\text{-}4)$$

$$\Delta x_n' \cong \sin\theta_i * \Delta x_n \qquad (C\text{-}5)$$

$$\therefore \Delta\theta_n = \frac{1}{m_\theta}\arctan\left(\sin\theta_i \frac{\Delta x_n}{L}\right) \qquad (C\text{-}6)$$

Appendix D: Measurement of Inherent Tension

The tension inherent in the thin rubber membranes can be determined by measuring the pressure at various air pressure levels inside the device. The membranes have enough flexibility to inflate like a balloon when the air pressure inside the device is increased. As described in section 3.2.2, the thin rubber membranes are mounted on a circular support of inner radius, R = 1.5 cm. Figure D-1 shows schematically how the distances used in the calculation are defined, where h is the distance of the top of the membrane from the equilibrium point and a, is the distance from the centre of curvature of the arc of the membrane to the equilibrium point. From the relationships between r, h, and a given in Equations (D-1) and (D-2) we can derive Equation (D-3) which allows us to determine r for various values of h.

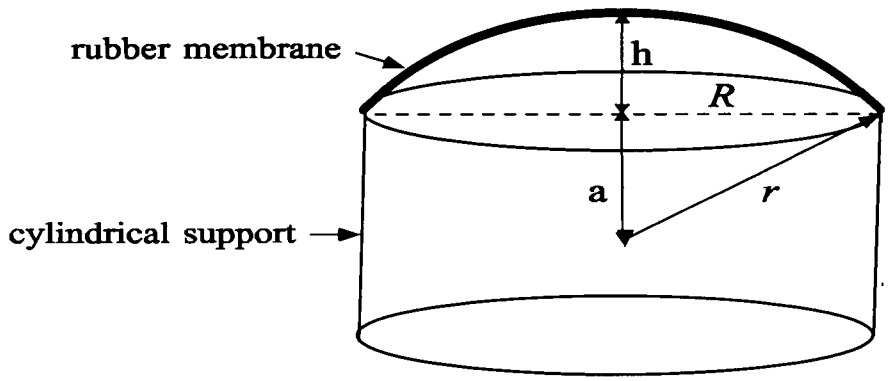

Figure D-1: Inflated rubber membrane

$$r = a + h \tag{D-1}$$

$$r^2 = a^2 + R^2 \tag{D-2}$$

$$r = \frac{h^2 + R^2}{2h} \tag{D-3}$$

The pressure inside a spherical balloon, P, is related to the tension in the rubber, σ, by Equation (D-4) where r is the radius of curvature of the balloon.

$$P = \frac{2\sigma}{r} \tag{D-4}$$

By measuring the height of the peak of the inflated membrane above the equilibrium point, h, the radius of curvature of the membrane can be calculated. The applied pressure can be measured by a manometer attached to the pressurization line. Thus, the tension, σ, in the inflated membrane can be determined. Combining equations (D-3) and (D-4), we can derive the following relation:

$$\sigma = \frac{P}{2}\frac{\left(h^2 + R^2\right)}{2h} \tag{D-5}$$

Using this relation, σ could be determined for a range of displacement values h. For small values of h/R, we expect σ to have some constant value, corresponding to the intrinsic tension, plus a term proportional to h^2 corresponding to the stretching of the rubber. For example, Figure D-2

shows results for a membrane of RTV31, ~25μm thick. The best fit line produces an inherent tension value of 0.041 N/m from the y-intercept.

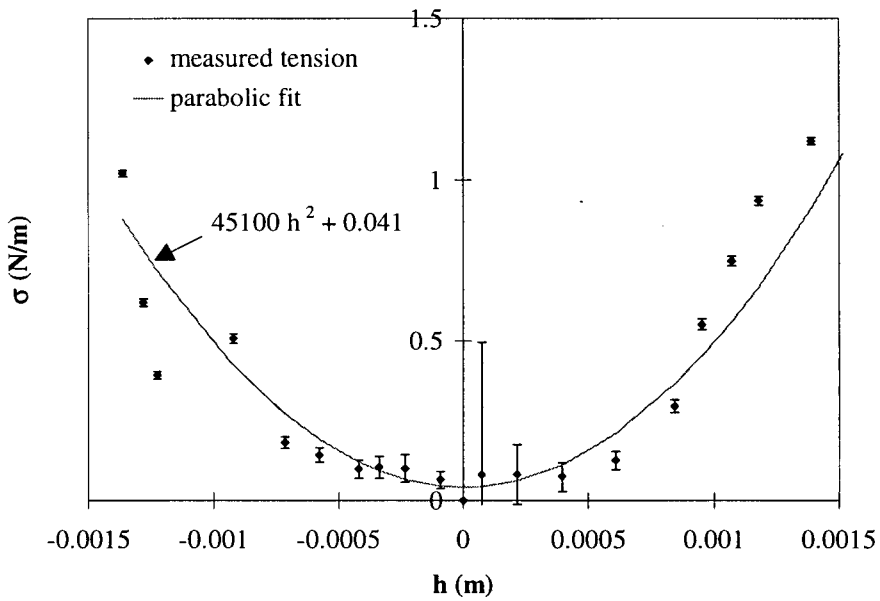

Figure D-2: Tension versus applied displacement of membrane to determine inherent tension